Exploring Thermal Phonon Transport from Atomic to Macroscopic Scales for Energy Conversion and Management

Thesis by

Chengyun Hua

In Partial Fulfillment of the Requirements for the
degree of
Doctor of Philosophy

Caltech

CALIFORNIA INSTITUTE OF TECHNOLOGY
Pasadena, California

2016
Defended May 18, 2016

ACKNOWLEDGEMENTS

First and foremost, I wish to express my genuine gratitude to my advisor, Professor Austin Minnich. His support and guidance throughout my stay at Caltech has had a profound influence on my development, both academic and personal. His passion for science, his creativity, and his critical thinking were a source of inspiration, motivation, and momentum that steered my research towards very interesting directions. I appreciated the freedom and independence he gave me to pursue my own ideas as well as the valuable suggestions and encouragement when needed. I consider myself fortunate to have had a mentor who dedicates so much time and attention to his students and hope to one day be able to emulate his example.

I thank Professors Melany Hunt, Guillaume Blanquart, and Brent Fultz, who, in addition to forming my thesis committee, have contributed many useful comments to this work. I appreciated their insightful suggestions on my research, which played a key role in the successful completion of my PhD work; I thank them for contributions to my career development, which will help me continue to thrive after Caltech. I also want to thank my undergraduate advisor Professor Eric Johnsen at the University of Michigan for introducing me to the fascinating world of science.

I wish to acknowledge the former and contemporary members of Minnich Lab, especially Dr. Xiangwen Chen and Navaneetha Krishnan Ravichandran, for all sorts of invaluable help they offered, insightful discussion over various research topics, and constructive critiques on my practice talks. I also want to thank the wonderful MCE (Cheryl Geer, Sonya Lincoln, and Maria Koeper) and ISP staff (Laura Flower Kim and Daniel Yoder) for always being available for assistance.

Caltech is not just about science and research. It is a place to discover talents, find passion as well as cultivate friendship. Without my friends, life at Caltech would have been far less colorful. I thank the fellows from my class Brandon Runnels, Lucas Meza, Brock Bobbit, and Hyun-Sik Kim for sharing the pains and joys inside and outside the classroom. I am also really grateful to have good friends like Nick Dou, Jackie Villadsen (and her cat Snug), Sunita Darbe, Sam Johnson, Esperanza Linares-Guerrero, Andres Goza, and Tess Saxton-Fox, who have shared with me the happiness and accompanied me through the difficulties. I particularly want to thank my dear friend Andrew Robbins for the enormous amount of time we spent in the office discussing research or simply procrastinating as well as all the outdoor

adventures we did together.

Finally, I want to thank my Mom and Dad, who have unconditionally supported me while I am chasing my dreams on the other side of the globe. Without their support, I would not have been able to make my way to Caltech.

Caltech is a truly amazing place. I was able to learn from the world-class scientists and engineers, work with the brightest minds, and have all sorts of adventures with the most wonderful people. I will forever cherish the memory of my life at Caltech.

ABSTRACT

Heat is one of the most fundamental forms of energy, and the ability to control heat plays a critical role in most current and future energy applications. Recently, interface engineering between heterogeneous solids has provided new approaches to manipulate heat transport at the scales of the energy carriers in solids, *i.e.* phonons which are quantized lattice vibrations. For example, nanocrystalline materials, which are polycrystalline materials with nanoscale grain sizes, are promising thermoelectric (TE) materials that have achieved substantially improved figure of merits compared to their bulk counterparts. This enhancement is typically attributed to a reduction in lattice thermal conductivity by phonon scattering at grain boundaries. On the other hand, inefficient heat dissipation across interfaces has been a long-standing problem that shortens the lifetime of electronics such as light-emitting diodes.

Despite the importance of interfaces, we still lack a comprehensive understanding of interfacial thermal phonon transport. For instance, the Fresnel coefficients enable the straightforward mathematical description of light as it moves between media of differing dielectric constants. Similarly, interfacial phonon transport can also be characterized by transmission coefficients that vary over the broad phonon spectrum in an analogous manner to Fresnel coefficients for light. However, despite decades of work, the spectral profile of these coefficients and how the profile is influenced by the atomic structure of actual interfaces remains unclear. As a result, the basic phenomenon of interfacial heat transport remains among the most poorly understood transport processes.

To elucidate this process, in this thesis we investigate interfacial thermal phonon transport using both modeling and experiment. The first portion of the thesis examines the impact of frequency-dependent grain boundary scattering in nanocrystalline silicon and silicon-germanium alloys using a novel computational method. We find that the grain boundary may not be as effective as commonly considered in scattering certain phonons, with a substantial amount of heat being carried by low frequency phonons with mean free paths longer than the grain size. Our result will help guide the design of more efficient TEs.

The second part of the thesis focuses on studying heat conduction using the Boltzmann transport equation (BTE), which is the governing equation of energy transport at length scales comparable to phonon mean free paths. The BTE is an integro-differential equation of time, real space, and phase space. Due to its high dimensionality, it is extremely challenging to solve. Here, we develop analytical methods to solve the frequency-dependent BTE, which allow us to obtain simple, closed-form solutions to complex multidimensional problems that have previously been possible to solve only with computationally expensive numerical simulations. We demonstrate that the solution leads to a more accurate measurement of phonon MFP spectra in thermal transient grating experiments.

Finally, we report the first measurements of thermal phonon transmission coefficients at a metal-semiconductor interface using ab-initio phonon transport modeling based on the BTE we develop in the second part and a thermal characterization technique, time-domain thermoreflectance. With our approach, we are able to directly link the atomic structure of an interface to the spectral content of the heat crossing it for the first time. Our work realizes the long-standing goal of directly measuring thermal phonon transmission coefficients and demonstrates a general route to study microscopic processes governing interfacial heat conduction.

PUBLISHED CONTENT AND CONTRIBUTIONS

(*1*) Chengyun Hua and Austin J Minnich. "Importance of frequency-dependent grain boundary scattering in nanocrystalline silicon and silicon–germanium thermoelectrics". In: *Semiconductor Science and Technology* 29.12 (2014), p. 124004. URL: `http://stacks.iop.org/0268-1242/29/i=12/a=124004`.
Contributions: Conducted Monte Carlo simulations in nanocrystalline structrues, analyzed the data, and wrote the manuscript.

(*2*) Chengyun Hua and Austin J. Minnich. "Analytical Green's function of the multidimensional frequency-dependent phonon Boltzmann equation". In: *Phys. Rev. B* 90 (21 2014), p. 214306. DOI: `10.1103/PhysRevB.90.214306`. URL: `http://link.aps.org/doi/10.1103/PhysRevB.90.214306`.
Contributions: Generated the idea, solved and analyzed the equation, and wrote the manuscript.

(*3*) Chengyun Hua and Austin J. Minnich. "Transport regimes in quasiballistic heat conduction". In: *Phys. Rev. B* 89 (9 2014), p. 094302. DOI: `10.1103/PhysRevB.89.094302`. URL: `http://link.aps.org/doi/10.1103/PhysRevB.89.094302`.
Contributions: Generated the idea, solved and analyzed the equation, and wrote the manuscript.

(*4*) Chengyun Hua and Austin J. Minnich. "Semi-analytical solution to the frequency-dependent Boltzmann transport equation for cross-plane heat conduction in thin films". In: *Journal of Applied Physics* 117.17, 175306 (2015). DOI: `http://dx.doi.org/10.1063/1.4919432`. URL: `http://scitation.aip.org/content/aip/journal/jap/117/17/10.1063/1.4919432`.
Contributions: Generated the idea, solved and analyzed the equation, and wrote the manuscript.

(*5*) Chengyun Hua et al. "Fresnel transmission coefficients for thermal phonons at solid interfaces". In: *In review process* (2016).
Contributions: Developed the analytical model, analyzed the experimental data, and wrote the manuscript.

TABLE OF CONTENTS

LIST OF ILLUSTRATIONS

LIST OF TABLES

Chapter 1

OVERVIEW

1.1 Nanoscale energy transport

The ability to tailor the fundamental physical properties of materials and devices exactly at the scale where they occur requires atomically precise control of matter. Modern technologies provide new approaches to use structure at the nanoscale as a tunable physical variable, which allows us to greatly expand the range of performance of existing materials and devices. One of the prominent topics in nanoscience is the ability to manipulate heat transport at the scales of energy carriers in solids. Precise control of heat could lead to efficient heat dissipation in high power and nanoscale electronic devices, the proposed use of intensely heated nanoparticles in medical therapies, and waste heat harvesting using thermoelectric devices in automobiles and airplanes.

Over the past decades, extensive research in nanoscale energy transport has led to remarkable advances such as the demonstration of thermoelectric materials with exceptionally high efficiencies. Recently, nanocrystalline materials, which are polycrystalline materials with nanoscale grain sizes, have been demonstrated as efficient thermoelectrics. Many of these materials show great promise for scalable manufacturing. In particular, the nanostructuring approach has been successful for silicon and silicon-germanium alloys created by ball-milling and hot pressing. SiGe has long been used for space power generation(*1*, *2*) and the thermoelectric properties of SiGe nanocomposites with improved properties over those of the bulk were recently reported.(*2*–*5*) Substantial improvements in nanostructured bulk silicon, which does not require expensive and rare germanium, were also reported.(*6*)

Research in engineering interfaces between two solids enables new functionalities that are not possible in homogeneous materials. For instance, electronic transport across metal-semiconductor and pn-junctions forms the basis for modern microelectronics, photovoltaics, and light-emitting diodes (LEDs). Interfaces play a key role in heat conduction by phonons as well: engineered interfaces in solids have led to dramatic increases in the efficiency of thermoelectric materials.

Anisotropic materials, which can possess extreme values of thermal conductivity that are difficult to achieve in isotropic materials, has been used to control heat flow in different crystal orientations.(*7*) For example, the extremely high thermal conductivity in the basal plane and low thermal conductivity in the cross plane makes graphite an attractive candidate for heat spreading applications in high-power transistors.(*8*)These are just a few examples of utilizing and engineering materials to gain the desired thermal properties in solids.

To ultimately achieve precise control of heat in solids, the knowledge of heat carriers is crucial. There are two major heat carriers in solids: electrons and phonons. Electrons carry charges as well as heat. In fact, in heavily-doped semiconductors, electrons can contribute up to half of the total thermal conductivity. Phonons are the quantized lattice vibrations in a crystal, which are the domaint heat carriers in dielectrics and semiconductors. While electronic properties in solids, *i.e.* electrical resistivity, optical absorption, and interfacial transmission processes, have been well understood, our knowledge of phonons lags far behind that of electrons.

For instance, the improved efficiency in nanocryatlline thermoelectric materials is achieved by significantly reducing the phonon thermal conductivity through strong phonon grain boundary scattering.(*3*, *4*, *6*, *9–12*) The physics of thermal conductivity is commonly interpreted using kinetic theory

$$k = \frac{1}{3} \sum_{pol} \int C_{\omega} v_{\omega} \Lambda_{\omega} d\omega, \tag{1.1}$$

where C_ω is the mode specific heat, v_ω is the group velocity, ω is the frequency, Λ_ω is the effective mean free path (MFP), and the sum runs over all phonon polarizations. Λ_ω includes all those scattering mechanisms present in a bulk sample, Λ_{bulk}, as well as additional scattering due to grain boundaries, Λ_{bdy}, which are combined using Matthiessen's rule: $\Lambda_\omega^{-1} = \Lambda_{bulk}^{-1} + \Lambda_{bdy}^{-1}$. The greatest challenges to engineer thermal conductivity are in measuring and calculating both Λ_{bulk} and Λ_{bdy}.

The knowledge of bulk mean free paths of solids is crucial to designing nanostructures that could provide optimal thermal properties.(*13*, *14*) Surprisingly, we do not know the MFPs in most solids. First-principle calculations based on density functional theory have enabled the direct computation of MFPs in materials with simple crystal structures. However, they have never been directly measured in experiments. Traditionally, semi-empirical expressions have been the only means to estimate MFPs.(*15*) Various experimental techniques to measure phonon MFPs exists such as photoacoustic wave propagation,(*16*) inelastic neutron scattering,(*17*) heat pulse techniques(*18*, *19*) but they have some limitation such as a restriction on the sample type, accessible phonon frequency range, or applicable temperatures. Recently, Minnich proposed a method(*20*) to accurately reconstruct the MFP distribution over a wide range of length scales and materials from the observation of quasiballistic thermal transport, which occurs if a temperature gradient exists over a length scales comparable to phonon MFPs.(*21*, *22*) The proposed method is suitable of a series of ultrafast optical techniques(*20*, *23–25*) where quasiballistic phonon transport can be observed. However, interpreting measurements using this reconstruction method requires the knowledge of heat conduction beyond the diffusion transport, which is a challenge itself. Thus, measuring phonon MFPs remains a tough task.

Another challenge in engineering thermal conductivity using nanostructures is to predict Λ_{bdy} for the complex interfaces, *i.e.* grain boundaries. Our knowledge of boundary scattering process is still based on simple models that were developed over 50 years ago and have never been experimentally verified. Numerous works over several decades have investigated the microscopic processes of phonon transport at solid-solid interfaces by observing the temperature dependence of the thermal conductivity or interface conductance(*26–30*) or by correlating changes in bonding strength and interface conductance.(*31*, *32*) However, these experimental approaches provide limited information about the microscopic information about thermal phonons because the observed quantities are averaged over all phonons and thus obscure the microscopic processes of interfacial thermal phonon transport at solid-solid interfaces.

The third challenge is to model heat conduction at length scales comparable to phonon MFPs, which has been of considerable interest recently(*33*) due to its applications in many technologies such as thermoelectrics(*10*, *12*) and electronic devices(*34*) as well as its potential to infer phonon MFP spectra in solids. At these small scales, classic continuum transport theories such as Fourier's law are not valid due to the absence of scattering and therefore a local temperature.(*35*) In this nondiffusive regime, phonon transport is nonlocal and is described by the phonon frequency-dependent Boltzmann transport equation (BTE).(*21*) The BTE is an integrodifferential equation of time, space, and phase space.(*36–39*) It is extremely challenging to solve due to its high dimensionality. Extensive efforts have been done to study phonon transport using BTE.(*40–43*) However, most of the previous approaches depended on simplifications to make the problem tractable, which in practice are not physical. Rigorous methods to model nanoscale heat conduction using the BTE with no or minimal simplifications in various geometries are key components of successfully controlling heat in solids.

1.2 Outline of this thesis

A better understanding of any one of these topics could lead to substantial contribution to our fundamental knowledge of energy carriers. The purpose of this thesis is to give insights into some of these questions. This work focuses on understanding energy transport by phonons at the nanoscale using theory, computational methods and ultrafast experimental techniques.

Chapter 2 studies the impact of frequency-dependent grain boundary scattering in nanocrystalline silicon and silicon-germanium alloys in a realistic 3D geometry using frequency-dependent variance reduced Monte Carlo simulations. We are able to explain the thermal conductivity measurements in nanocrystalline Si by Wang *et. al.* while the commonly used gray model, assuming phonon-grain boundary scattering rate is a constant for all phonon modes, predicts the wrong trend of thermal conductivity at low temperatures. We find that the grain boundary may not be as effective as predicted by the gray model in scattering certain phonons. We also identify the portion of the phonon spectrum that is responsible for carrying heat across the grain boundaries, therefore helping guide the design of more efficient TEs.

While this computational study provides important insights, one issue still remains. Even though the proposed frequency-dependent model reproduces the experimental measurements, the fitting itself is not unique. Since thermal conductivity is a macroscopic property that is integrated over the thermal spectrum, there exists multiple choices of this underlying distribution that result in the same thermal conductivity. Moreover, we do not know the spectral properties of thermal phonons in most of the materials. The second portion of the thesis focuses on determining how to more directly measure properties of the heat carriers like the phonon MFP distribution in bulk materials and phonon transmission coefficients at a solid-solid interface.

In Chapter 3, we present analytical solutions to the phonon Boltzmann transport equation, the governing equation when heat transport occurs at length scales comparable to phonon MFPs. We first derive an analytical Green's function for the frequency-dependent, multidimensional Boltzmann equation under the relaxation-time approximate. Then, we present a semi-analytical series expansion method to solve the transient, frequency-dependent BTE in a thin film geometry. The new solutions are valid from diffusive to ballistic transport regimes and rigorously includes frequency dependence of phonon properties and enables simple closed-form solutions for a number of multidimensional problems for which the only prior solution methods have been computationally expensive numerical methods. Most importantly, the analytical solutions allow us to inspect nanoscale heat conduction just by looking at the expression of the equation, which is not directly accessible from pure numerical approaches.

The rest of the thesis focuses on applying the derived analytical solutions to extract the spectral properties of thermal phonons in bulk materials and at interfaces. Chapter 4 analyzes heat conduction in transient grating (TG) spectroscopy and demonstrates that the new analytical Green's function enables a more accurate measurement of MFP spectra, therefore leading to an improved understanding of heat conduction in solids.

In Chapter 5, we report the first measurements of thermal phonon transmission coefficients at a metal-semiconductor interface using ab-initio phonon transport modeling based on the BTE solutions in Chapter 3 and a thermal characterization technique, time-domain thermoreflectance. With our approach, we are able to directly link the atomic structure of an interface to the spectral content of the heat crossing it for the first time. Our work realizes the long-standing goal of directly measuring thermal phonon transmission coefficients and demonstrates a general route to study microscopic processes governing interfacial heat conduction.

Finally, chapter 6 examines possibilities for future work and concludes the thesis.

Chapter 2

PHONON TRANSPORT IN NANOCRYSTALLINE MATERIALS

Chapter 2 has been adapted from:

(*1*) Chengyun Hua and Austin J Minnich. "Importance of frequency-dependent grain boundary scattering in nanocrystalline silicon and silicon–germanium thermoelectrics". In: *Semiconductor Science and Technology* 29.12 (2014), p. 124004. URL: `http://stacks.iop.org/0268-1242/29/i=12/a=124004`.

2.1 Background

Thermoelectric (TE) materials, which can convert heat directly to electricity, are of considerable interest for applications such as waste heat recovery due to their silent operation, reliability and lack of working fluid.(*44–46*) The performance of TE devices is characterized by the thermoelectric figure of merit $zT = S^2\sigma T/(k_e + k_{ph})$, where S is the Seebeck coefficient, σ is the electrical conductivity, T is the absolute temperature at which the properties are measured and k_e and k_{ph} are the corresponding thermal conductivities for electrons and phonons.(*21*) To achieve comparable efficiency to that of mechanical cycles, zT should be greater than 2, but commonly used bulk TE materials such as Bi_2Te_3 typically have $zT < 1$.

Recently, nanocrystalline materials, which are polycrystalline materials with nanoscale grain sizes, have been demonstrated as efficient thermoelectrics. The improved efficiency is achieved by significantly reducing the phonon thermal conductivity through strong phonon grain boundary scattering.(*3*, *4*, *6*, *9–12*) Many of these materials show great promise for scalable manufacturing. In particular, the nanostructuring approach has been successful for silicon and silicon-germanium alloys created by ball-milling and hot pressing. SiGe has long been used for space power generation(*1*, *2*) and the thermoelectric properties of SiGe nanocomposites with improved properties over those of the bulk were recently reported.(*2*–*5*) Substantial improvements in nanostructured bulk Si, which does not require expensive and rare Ge, were also reported.(*6*) While these gains are significant, further improvements are difficult to achieve due to the lack of understanding of grain boundary scattering, which plays a critical role in scattering phonons in nanocrystalline materials.

Phonon transport in nanostructured Si/SiGe has been recently studied using molecular dynamics(*47*–*51*), atomistic Green's functions(*52*–*54*) and phonon-Boltzmann-equation-based simulations.(*55*–*61*) Many studies assumed that the transmissivity of phonons across the boundary to be constant in a gray model. However, atomistic calculations(*50*, *51*, *53*, *54*) reported that transmissivity depends on phonon frequency. Kimmer *et al.*(*51*) found that transmission through the high-energy grain boundary in silicon is a function of the phonon frequency using molecular-dynamics simulations. Li and Yang(*53*) used atomistic Green's functions to study the effect of lattice mismatch on phonon transmission across interfaces and showed that transmissivity decreases as phonon frequency increases. These predictions are supported by a recent experimental work by Wang *et al*(*62*), who reported temperature (T) dependent measurement of thermal conductivities of nanocrystalline silicon. While a T^3 dependence of thermal conductivity is expected based on the gray model, they instead observed a T^2 dependence, implying that transmissivity increases with decreasing phonon frequency. This result suggests that lower frequency modes are less scattered by interfaces compared to higher frequency modes. A frequency-dependent transmissivity would have an important effect on the distribution of heat among the phonon spectrum and hence on strategies to further reduce the thermal conductivity of nanocrystalline Si and SiGe. However, phonon transport in nanocrystalline thermoelectrics with frequency dependent grain boundary scattering has not yet been systematically explored.

Here we examine the effects of frequency-dependent grain boundary scattering on the thermal conductivity of nanocrystalline Si and SiGe alloys using efficient variance-reduced Monte Carlo (MC) simulations. This novel computational method enables the simulation of phonon transport in the full 3D geometry of the crystal with orders of magnitude reduced computational cost compared to previous numerical methods while rigorously including the frequency-dependence of phonon properties. Moreover, the simulations allow us to examine in detail how the frequency-dependent grain boundary scattering modifies the distribution of heat among the thermal phonon spectrum, providing an important guide to further improving the thermoelectric efficiency of nanocrystalline Si and SiGe.

2.2 Modeling

We seek to simulate thermal phonon transport in a polycrystalline domain with grain sizes of tens to hundreds of nanometers. To study heat transfer in this mesoscopic structure, we solve the frequency-dependent Boltzmann transport equation (BTE) under the relaxation time approximation, which is accurate to approximately 10% in silicon.(*63*) The energy-based BTE is given by:(*35*, *64*)

$$\frac{\partial e^d_\omega}{\partial t} + \mathbf{v}_g \cdot \nabla e^d_\omega = \frac{(e^{loc}_\omega - e^{eq}_\omega) - e^d_\omega}{\tau(\omega, p, T)}, \tag{2.1}$$

where $e^d_\omega = \hbar\omega(f - f^{eq}_{T_{eq}})$ is the desired deviational distribution function, $f^{eq}_T = [exp(\hbar\omega/k_bT) - 1]^{-1}$ is a Bose-Einstein (BE) distribution at the temperature T, $e^{loc}_\omega = \hbar\omega f^{eq}_{T_{loc}}$ is the BE distribtion at the local equilibrium temperature T_{loc}, $e^{eq}_\omega = \hbar\omega f^{eq}_{T_{eq}}$ is the BE distribtion at the global equilibrium temperature T_{eq}, $\mathbf{v}_g(\omega, p)$ is the phonon group velocity and $\tau(\omega, p, T)$ is the phonon relaxation time. Here, $\hbar$ is the reduced Planck constant, k_b is the Bolzmann constant, T is the temperature, ω is the phonon frequency and p is the phonon polarization.

The BTE is an integro-differential of time, real space and phase space, and it describes a wide range of phenomena in many field ranging from astronomy to neutron transport.(*36*–*39*) The equation was first used to describe phonons in solids by Peierls in 1929.(*65*) In 1958, Englman obtained analytical solutions of the BTE with simpler collision terms to describe the transport theory of temperature waves in insulators. Later, Williams extended Englman's theory and obtained simpler forms of the solution.(*66*) In the 1960s and 70s, Simons developed the theory of high-frequency thermal waves in dielectrics in which phonons can undergo both normal and resistive interaction processes based on the BTE.(*67*) A decade later, the equation was re-investigated by Claro and Mahan(*68*) to study the nonlocal heat transfer effects during transient heating. Majumdar derived an equation of phonon radiative transfer from the BTE(*22*), which was applied to study heat transfer across diamond thin films for both steady-state and transient cases.(*69*) Chen demonstrated the failure of Fourier's law in nonplanar nanostructures and provided a general solution for the temperature rise of heat-generating nanometer and micrometer particles embedded in a host medium based on the BTE.(*40*) Later, he derived ballistic-diffusive heat-conduction equations from the BTE which gave a better approximation than the Fourier Law at small scales but was much simpler to solve than the BTE(*42*). This two-channel model was then employed to solve several planar nanoscale heat conduction problems.(*41*) Recently, Miranda *et al.* obtained a constitutive equation for heat conduction derived from the exact solution of the BTE by a series expansion.(*43*)

Despite these extensive efforts to study phonon transport using the BTE, most of the previous approaches depended on simplifications to make the problem tractable. For example, all the works mentioned above assumed a single phonon mean free path even though recent work has demonstrated that the transport properties of phonons in solids vary widely over the broad thermal spectrum.(*70*, *71*) Further, the above solutions assumed simple 1D geometries that do not often occur in practice. Various numerical techniques have been developed to solve the BTE, including discrete ordinates(*35*), a finite volume approach(*72*), Monte Carlo simulations(*55*, *59*), and a mean free path (MFP) sampling algorithm.(*73*) However, these methods are either computationally expensive or make simplifying assumptions that may not be accurate. Another approach to incorporate boundary scattering is to model the interface scattering using a phenomenological volumetric scattering rate $\tau^{-1} = v/L$.(*60*) While this approach has minimal computational requirements and provides useful insights, it lacks predictive power because the value of the geometrical length L depends on frequency in the non-gray model and is not known in advance.

In this work, we overcome these computational challenges using a novel variance-reduced, frequency-dependent Monte Carlo technique recently introduced by Peraud and Hadjiconstantinou. (*64*, *74–77*) Specifically, we solve the adjoint BTE using a linearized, energy-based deviational MC algorithm. This algorithm enables us to solve the frequency-dependent BTE in a large, complex geometry with minimal memory requirements and substantially reduced computational cost compared to traditional MC algorithms.

The algorithm we have chosen incorporates several key improvements over other numerical methods that we describe in turn. First, we use a deviational MC algorithm based on Eq. (2.1) rather than traditional MC method.(*64*) Deviational MC techniques achieve variance-reduction by recognizing that many of the collisions performed in traditional MC simulations serve only to stochastically compute the Bose-Einstein equilibrium distribution that is already known analytically. The variance of the calculation can be dramatically reduced by replacing the stochastic calculation of this known distribution with an analytical expression and only simulating the parts that deviates from the equilibrium distribution.

Second, for problems exhibiting sufficiently small temperature differences, the collision operator in Eq. (2.1) can be linearized. As a result, properties for scattered particles can be drawn from a distribution that is independent of the local temperature, allowing each particle to be simulated independently and thereby eliminating the need for discretization in space and time.(*74*) In addition to further reducing computational cost, this method dramatically reduces the memory requirements of MC simulations because all the phonon properties do not need to be stored simultaneously.

Finally, we solve the adjoint BTE rather than the traditional BTE using a recent approach introduced by Peraud *et al.*(*75–77*) One drawback of solving the traditional BTE is that the frequencies of the phonon are drawn from the heat flux distribution $\hbar\omega D(\omega,p)v(\omega,p)f^{eq}_{T_{eq}}$, which is weighted by the density of states $D(\omega,p)$. As a result, even if modes with small density of states contribute substantially to heat conduction, as occurs in silicon, these phonons are unlikely to be sampled, leading to large noise at certain frequencies. Peraud *et al.* recently showed that this limitation can be overcome using an adjoint approach, in which phonons are emitted uniformly over the frequency spectrum and subsequently weighted by the heat flux distribution to provide a variance-reduced estimate of the heat flux. The underlying idea is that when the estimator, or in this case the heat flux in a specific frequency bin, corresponds to a small region of phase space, one can exploit the time-reversibility of the BTE to emit phonons from the estimator and follow their trajectories backwards in time. In this way, the probability that a given sample contributes to the desired estimator is considerably increased, reducing the overall noise.

The full details of the computation are discussed by Peraud *et al.* and will only be briefly reviewed here. The computational domain is a 3D cube with square grains as illustrated in the inset of Fig. 2.3. The domain bisects the grain in each dimension, placing the corner of the grains in the center of the domain. We impose a periodic heat flux boundary conditions along the direction of temperature gradient to model an infinitely repeating structure.(*78*) The other two directions have a specular boundary condition imposed by symmetry. These boundary conditions allow the thermal properties of an infinite polycrystal to be calculated using only one period.

We impose a linearly varying equilibrium temperature $T_{eq}(x)$ that allows the control temperature to follow the physical temperature more closely.(*74*) This variation in T_{eq} can be implemented as a uniform volumetric source of deviational phonon bundles, each representing a fixed amount of deviational energy. The frequencies of the phonon bundles are drawn from a uniform distribution, rather than the heat flux distribution, according to the adjoint BTE. The algorithm then proceeds by stochastically simulating the advection, scattering, and sampling of phonon bundles sequentially and completely independently exactly as described by Peraud *et al.*(*74*) Finally, the calculated spectral heat flux is weighted by the heat flux distribution to obtain an unbiased calculation of the heat flux.(*75*)

In this work, we consider Si and $\mathrm{Si}_{1-x}\mathrm{Ge}_x$ ($x < 0.5$) with Ge modeled as a mass defect scattering mechanism in silicon. We model silicon using the experimental dispersion along the [100] direction as reported in the previous literature and assume that the crystal is isotropic.(*79*) Optical phonons are neglected due to their small contributions to heat transfer in silicon.(*55*) The relaxation times caused by three-phonon scatterings (τ_L for longitudinal acoustic phonons and τ_T for transverse acoustic phonons) and phonon-mass-defect scatterings τ_{MD} are given by(*79–81*):

$$\begin{aligned} \tau_L^{-1}(\omega) &= 2 \times 10^{-19} \times \omega^2 T^{1.49} \exp(-80/T), && (2.2)\\ \tau_T^{-1}(\omega) &= 1.2 \times 10^{-19} \times \omega^2 T^{1.65} \exp(-80/T), && (2.3)\\ \tau_{MD}^{-1}(\omega) &= A\omega^4, && (2.4) \end{aligned}$$

where A is a constant that equals 3×10^{-45} for bulk silicon(*82*).

For electron-phonon scattering, the relaxation time is given as(*83*)

$$\tau_{ep}^{-1}(\omega) = \frac{E_d^2 m^{*3} v_s}{4\pi\hbar^4\rho}\frac{k_B T}{\frac{1}{2}m^* v_s^2}\left\{\frac{\hbar\omega}{k_B T} - \ln\frac{1+\exp\left[\frac{\frac{1}{2}m^* v_s^2 - E_f}{k_B T} + \frac{\hbar^2\omega^2}{8m^* v_s^2 k_B T} + \frac{\hbar\omega}{2k_B T}\right]}{1+\exp\left[\frac{\frac{1}{2}m^* v_s^2 - E_f}{k_B T} + \frac{\hbar^2\omega^2}{8m^* v_s^2 k_B T} - \frac{\hbar\omega}{2k_B T}\right]}\right\}, \tag{2.5}$$

where E_d, m^*, ρ, v_s, and E_f represent acoustic deformation potential, density of states effective mass, density, averaged phonon group velocity and Fermi level, respectively. The values of m^*, v_s, ρ and E_f are obtained from the literature, which are $m^* = 1.4m_0$ (m_0 is the electron mass), $v_s = 6500$ m/s, $\rho = 2500$ kg/m^2, and $E_f = 0.05$ eV corresponding to a doping concentration of approximately 10^{20} cm^{-3} in n-type Si.

For mass defect scattering in SiGe, we take $A = 3\times10^{-42}$, which corresponds to $x = 0.25$ in Si$_{1-x}$Ge$_x$ according to the formula given by Klemens.(*82*) We then adjust the deformation potential E_d until the thermal conductivity matches experimentally reported values of bulk SiGe,(*84*) yielding $E_d = 2.5$ eV, in reasonable agreement with the value reported by Holland.(*80*) For doped Si, we change A to be 3×10^{-43}, which corresponds to a doping concentration of 10^{20} cm^{-3}.(*55*) In the next section, we show that the results of this work are not sensitive to the exact values of these fitting parameters.

The critical parameter in our model is the phonon transmissivity across the grain boundaries. Many previous works assumed a gray model, but this model is not consistent with the measurements of Wang *et al.* We use a frequency-dependent transmissivity $t(\omega)$ proposed by Wang *et al.* in the form of(*62*)

$$t(\omega) = \frac{1}{\gamma\omega/\omega_{max} + 1}, \tag{2.6}$$

where γ is a fitting parameter and ω_{max} is the maximum phonon frequency with nonzero density of states (~ 12 THz for silicon). This model is qualitatively consistent with atomistic Green's function calculations.(*52*, *53*) Note that this condition implies that the transmissivity approaches one as frequency goes to zero, which is physically consistent with the expectation that long wavelength phonons are unaffected by atomistic disorder at a grain boundary. In this work, we denote gray and non-gray as constant and frequency-dependent transmissivity, respectively. Note that other parameters in the BTE always depend on phonon frequency regardless of the transmissivity model.

We implement the interface condition with the following procedure. If a particle encounters the interface, its transmissivity is calculated using the phonon's frequency. If a random number is less than the calculated transmissivity, then the phonon transmits through the interface; otherwise, the phonon is reflected. Following Wang *et al.*, we use Ziman's specularity parameter to determine whether the scattering is specular or diffuse:

$$P(\omega, p) = \exp\left[-\frac{16\pi^2\eta^2}{\lambda^2(\omega, p)}\right], \tag{2.7}$$

where $\lambda(\omega, p)$ is the phonon wavelength and η is the rms surface roughness. If a randomly drawn number is less than P, the phonon experiences specular scattering, in which case the phonon's velocity vector is known from momentum conservation. Otherwise, the phonon is scattered diffusely. In the latter case, the phonon's new velocity vector is randomized according to the half-sphere defined by the normal vector of the interface.

2.3 Results and discussion

We validated our code by computing the spectral thermal conductivity versus phonon frequency of the bulk silicon at room temperature. The analytical expression for the spectral thermal conductivity is $k(\omega, p) = \frac{1}{3}C(\omega, p)v_g(\omega, p)\Lambda(\omega, p)$, where $C(\omega, p) = \hbar\omega D(\omega, p)\frac{\partial f_{BE}}{\partial T}$ is the mode specific heat, $D(\omega, p)$ is the density of states, and $\Lambda(\omega, p) = \tau(\omega, p)v_g(\omega, p)$ is the phonon MFP. Figs. 2.1 (a) & (b) show the corresponding density of states and group velocity versus phonon frequency for two transverse acoustic branches and one longitudinal acoustic branch in silicon used in this work. $k(\omega, p)$ gives a quantitative measure how each phonon contributes to the total thermal conductivity. As shown in Fig. 2.2, excellent agreement between the computation and the analytical solution is observed. Also note that the stochastic noise is low over the entire phonon spectrum in the adjoint method, while the noise increases as the phonon frequency decreases with the original algorithm due to undersampling of low frequency phonons.

With this validation, we proceed to the nanocrystalline material by determining the fitting parameter γ in Eq. (2.6). The reported material had 550 nm grains and was nominally undoped. By fitting the experimental thermal conductivity with our model, we obtain $\gamma = 0.12$ and the surface roughness $\eta = 0.5$ nm in Eq. (2.7), which explain the thermal conductivity data from Wang *et al.* Since the reported Si is nominally undoped, we take A in Eq. (2.4) to be the value of bulk silicon. As shown in Fig. 2.3, the simulated thermal conductivities of nanocrystalline silicon obtained using the proposed transmissivity model is in good agreement with the experiment over the temperature range. Note that based on the fitted γ as shown in Fig. 2.4, the transmissivity varies from 1 to 0.85 as frequency increases, which is much higher than the typical nominal value of the transmissivity used in the literature.

With the fitting parameters determined, we first examine the difference between the gray and non-gray model for the same undoped nano-Si material. We focus on examining the distribution of heat in the thermal phonon spectrum by plotting the spectral thermal conductivity as a function of phonon frequency. We choose the frequency-independent transmissivity in the gray model to be 0.92 such that the total thermal conductivities given by the gray and non-gray models are approximately the same. As shown in Fig. 2.5, the gray model predicts a substantial decrease in heat at the low frequency regime while the non-gray model predicts a much higher

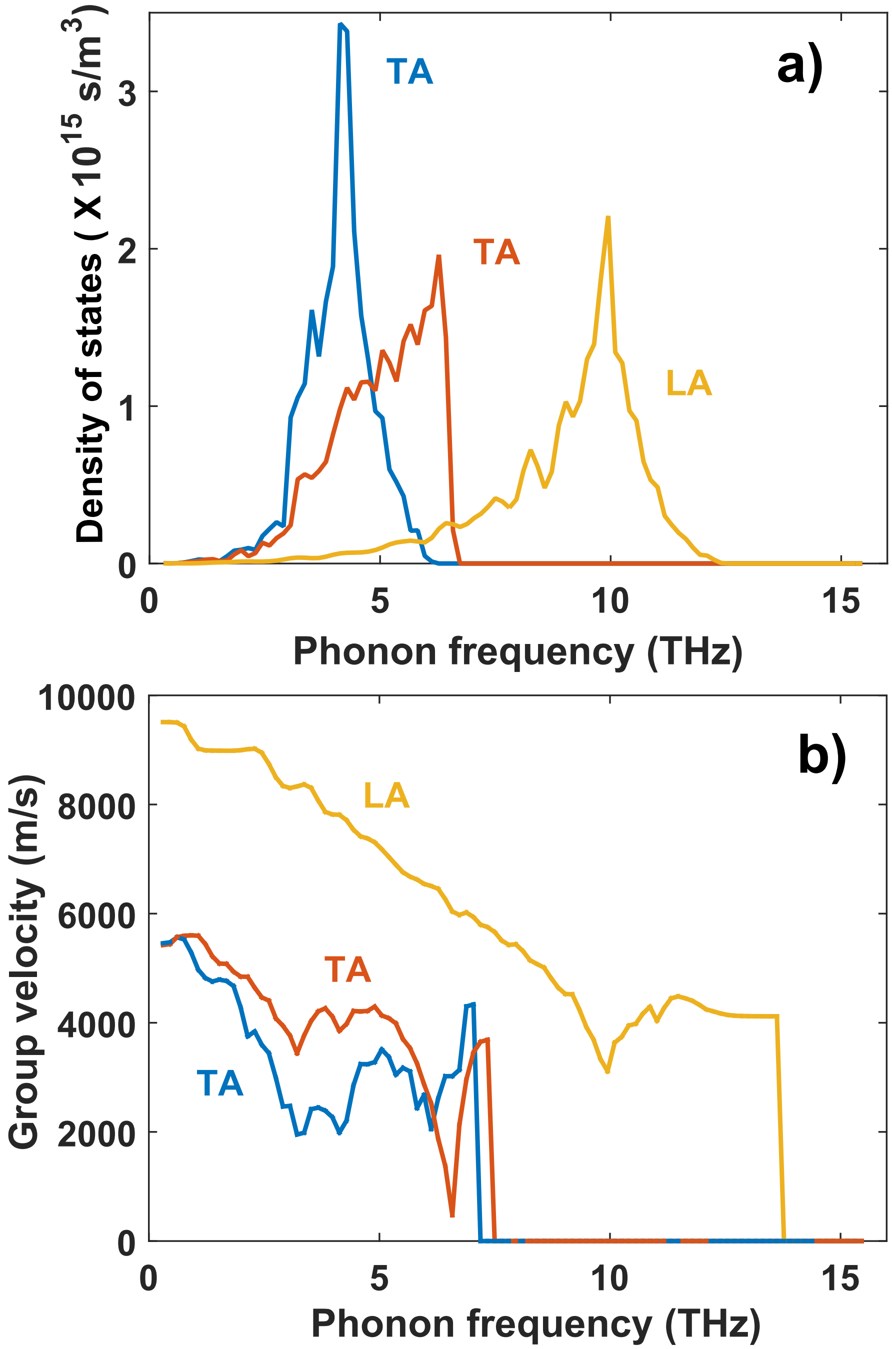

Figure 2.1: (a) Density of states and (b) magitude of group velocity versus phonon frequency for bulk silicon: blue and orange lines represent transverse acoustic modes, and yellow lines represent longitudinal acoustic modes.

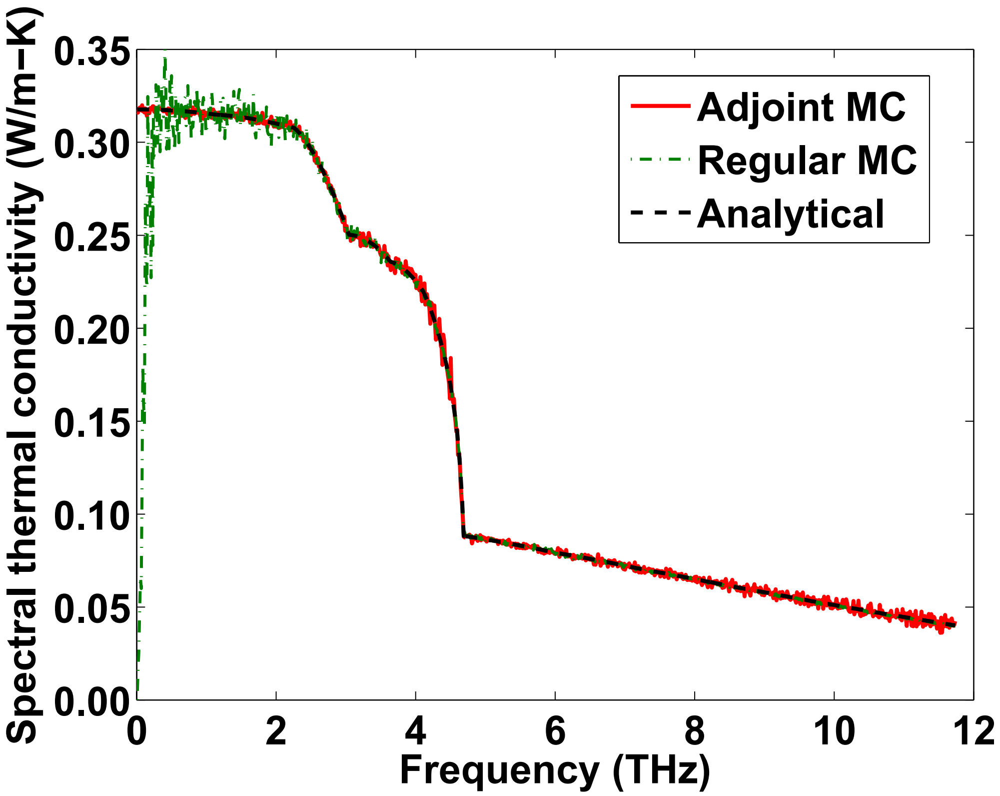

Figure 2.2: Spectral thermal conductivity versus phonon frequency for bulk silicon at 300 K: adjoint MC method (solid line); original MC algorithm (dash-dotted line); analytical solution (dashed line). The noise in the adjoint MC is substantially less than that of the original algorithm at low frequencies. The abrupt change in the slope of the spectral thermal conductivity at 5 THz is due to the cutoff of density of states in Si's transverse acoustic modes.

contribution to the total heat from those low frequency phonons. This increase is expected because the transmissivity approaches one in the low frequency limit, indicating that low frequency phonons are scattered less by grain boundaries compared to the prediction of the gray model.

We next seek to understand doped nanocrystalline Si/SiGe thermoelectric materials by using the fitted constants described in the previous section to account for the mass defect and electron-phonon scattering mechanisms. We take grain size to

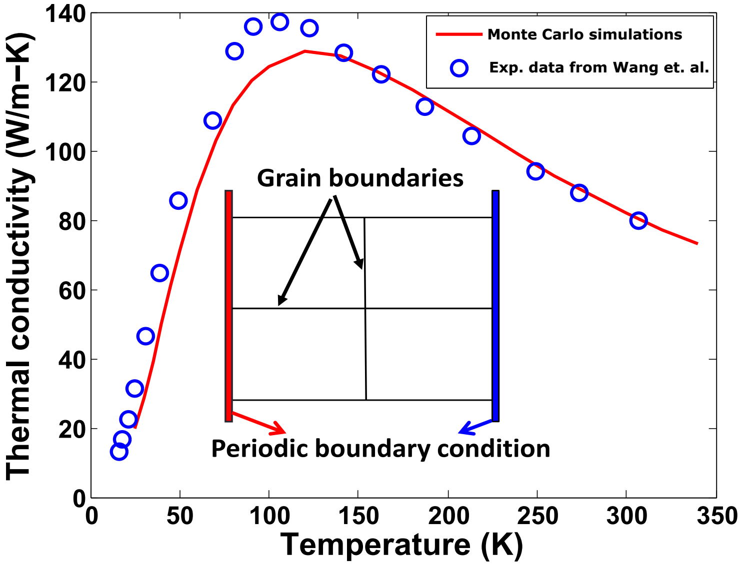

Figure 2.3: Simulated (line) and measured (circles) thermal conductivities for pure nanocrystalline silicon with grain sizes at 550 nm, demonstrating good agreement. Inset: 2D schematic of a unit cell used in the simulation. The grain boundary bisects the domain at the indicated location.

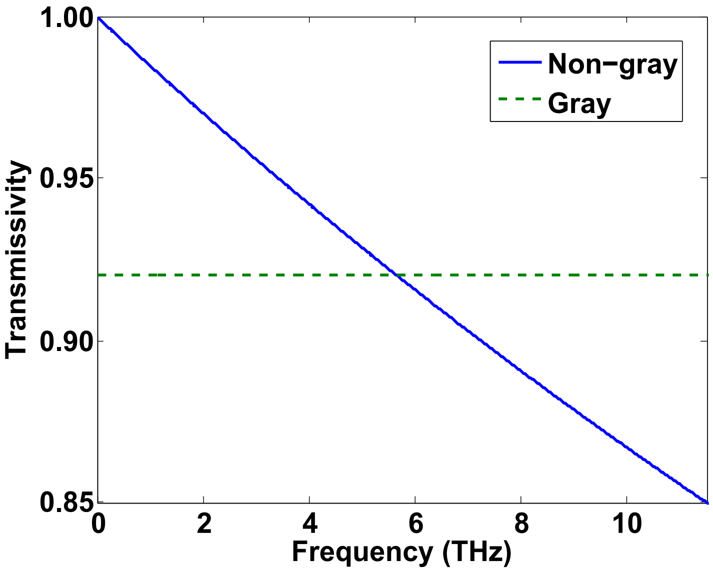

Figure 2.4: Non-gray (line) and gray (dashed line) phonon transmissivities at grain boundaries plotted versus phonon frequency.

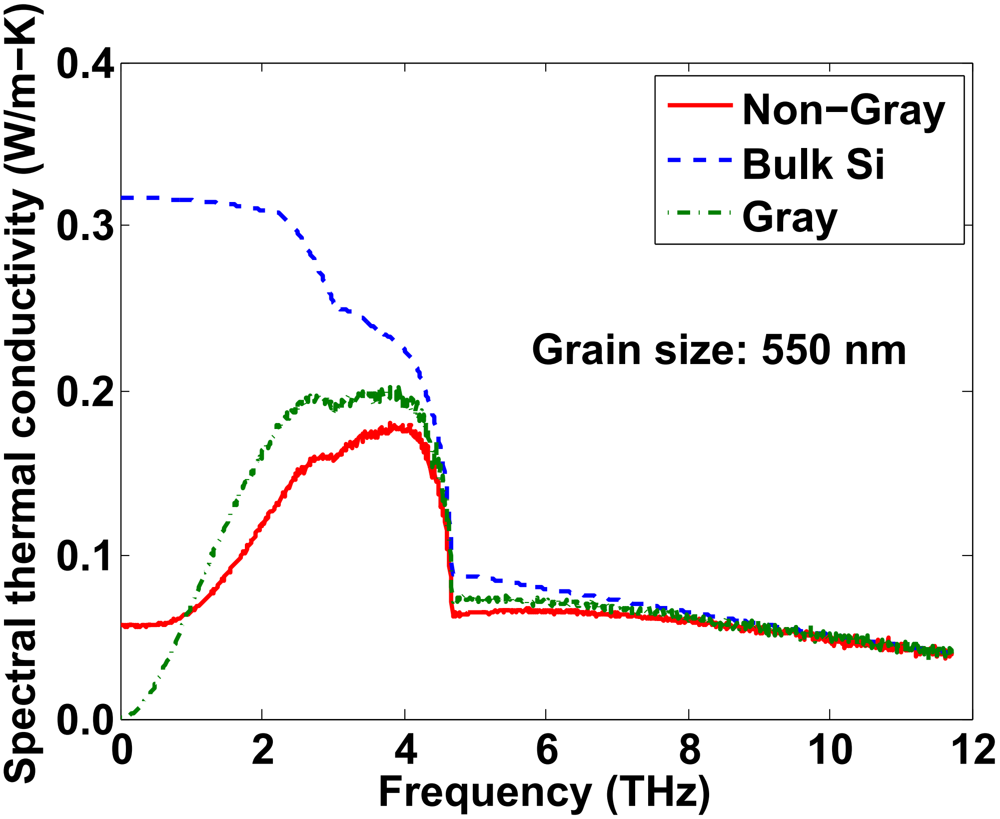

Figure 2.5: Room-temperature spectral thermal conductivity versus phonon frequency with 550 nm grain: bulk silicon (dashed line), nanocrystalline silicon with gray model (dash-dotted line), and nanocrystalline silicon with non-gray model (solid line). Low frequency phonons carry more heat in the non-gray model.

be 20 nm following the experimental reports.(*3*–*6*) The result of these effects on the heat transport in nanocrystalline silicon and SiGe is shown in Fig. 2.6. We find that high frequency phonons are strongly scattered by the impurities while low frequency phonons are scattered by the electrons, as expected. However, due to the non-gray transmissivity, a large fraction of heat is carried by phonons with frequency less than 4 THz. This observation is unexpected because under the gray model, thermal conductivity reduction is largely due to the scattering of these low frequency phonons, but contribution of these modes remains significant in the non-gray model.

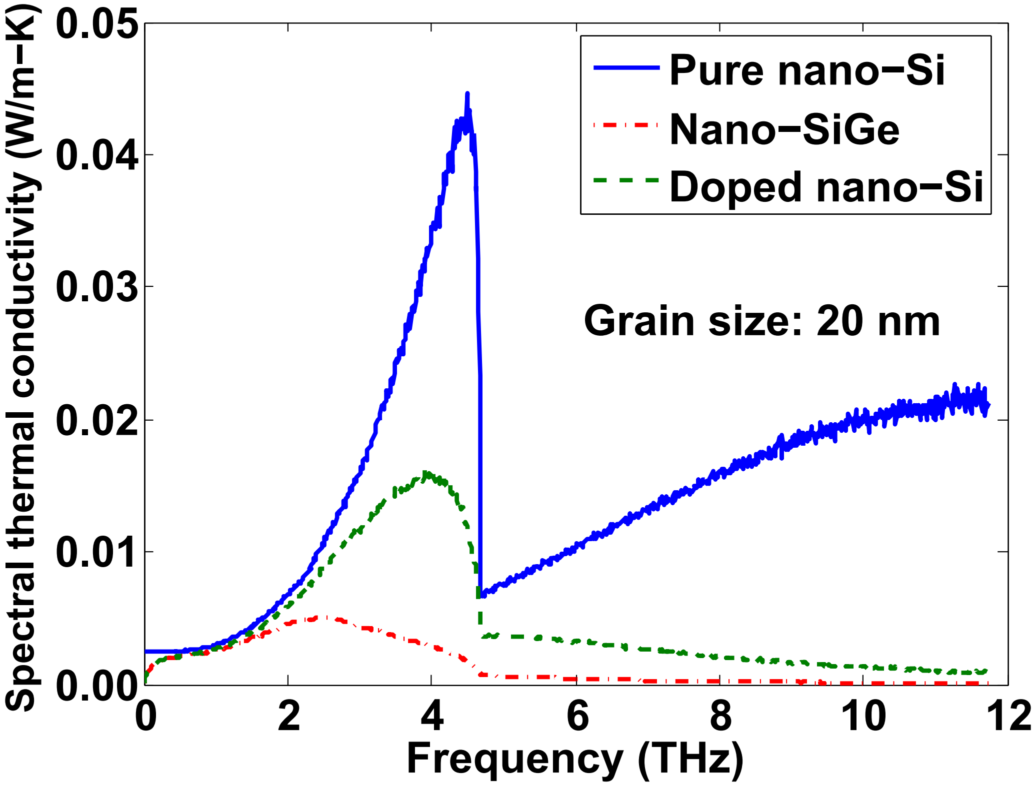

Figure 2.6: Room-temperature spectral thermal conductivity versus phonon frequency with 20 nm grain: pure nanocrystalline silicon (solid line), doped nanocrystalline silicon (dashed line) and nanocrystalline silicon germanium (dash-dotted line). High frequency phonons are scattered by mass defects while low frequency phonons are scattered by electrons.

To determine the key length scales for heat conduction, we calculate the phonon MFPs. We plot this quantity as the thermal conductivity accumulation function, which has been shown to be a useful quantity for understanding thermal transport.(*85*, *86*) We calculate the accumulation function by determining an effective MFP for each mode that incorporates all the scattering mechanisms, including grain boundary scattering, using the spectral thermal conductivity for each phonon frequency and polarization and the kinetic equation: $\Lambda_{eff} = 3k(\omega, p)/C(\omega, p)v(\omega, p)$. The spectral thermal conductivity can then be sorted by MFP, from which the ther-

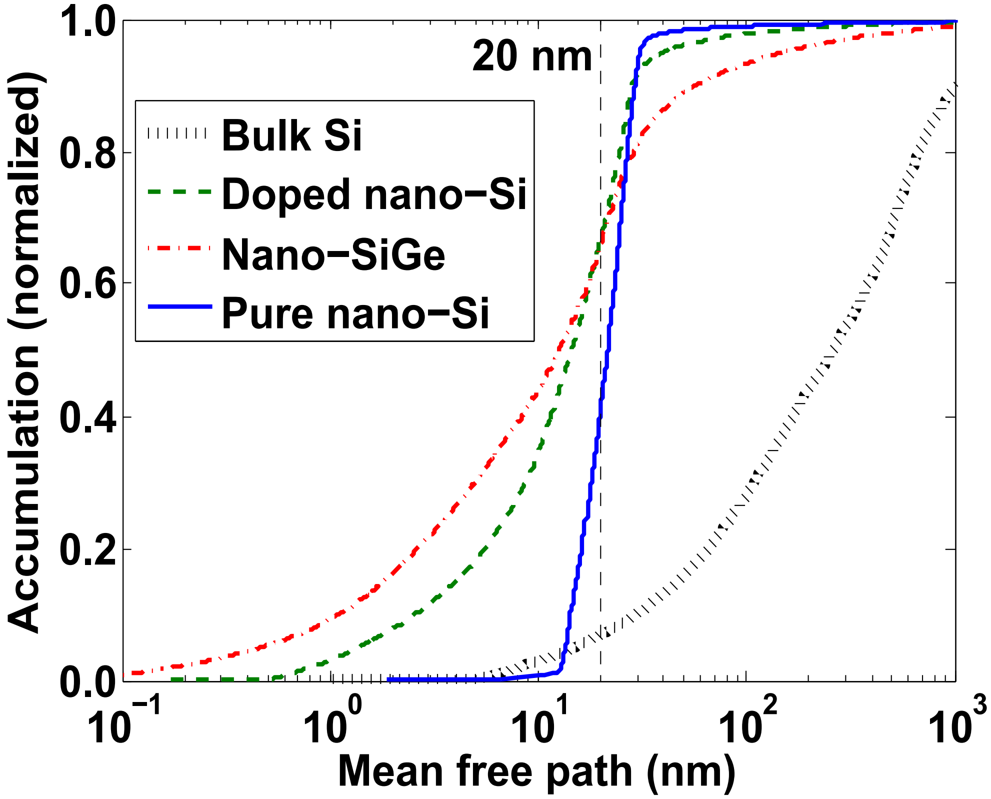

Figure 2.7: Thermal conductivity accumulation versus phonon MFP: pure nanocrystalline silicon (solid line), doped nanocrystalline silicon (dashed line), doped nanocrystalline silicon germanium (dash-dotted line), and bulk silicon (dotted line). Heat is still carried by long MFP phonons in nanocrystalline Si/SiGe even though many low frequency phonons are scattered by electrons.

mal conductivity accumulation is obtained from the cumulative sum of the spectral thermal conductivity.

Our simulations show a surprising result. As shown in Fig. 2.7, at room temperature, about 60 % of the total heat in undoped nanocrystalline silicon with a grain size around 20 nm is carried by the phonons with MFPs longer than the grain size, which are denoted long MFP phonons here. Even in doped nanocrystalline Si and SiGe, for which low frequency phonons are scattered by electrons, as much as 35 % of the total heat is carried by these long MFP phonons.

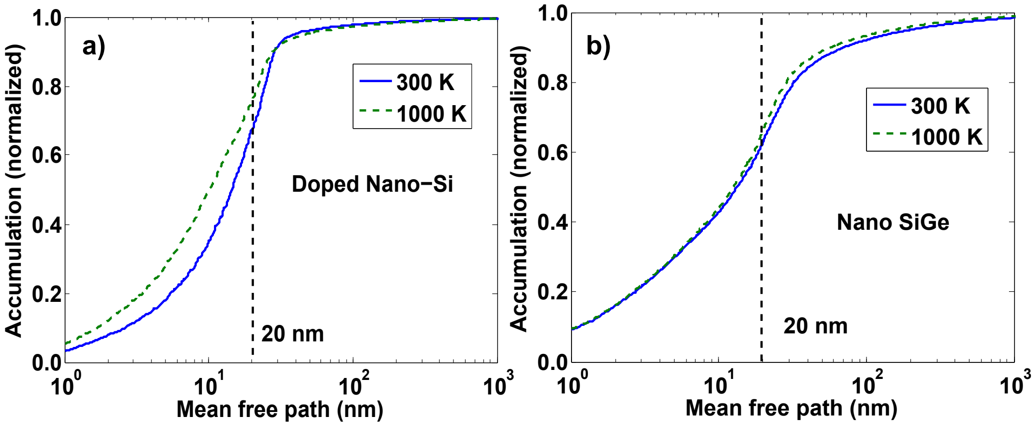

Figure 2.8: Thermal conductivity accumulation for (a) doped nanocrystalline Si and (b) doped nanocrystalline SiGe with 20 nm grains versus phonon MFP at 300 K (solid line) and 1000 K (dashed line). At high temperatures, there is still a large fraction of heat carried by long MFP phonons even when phonon-phonon scattering is dominant.

To verify that our conclusion does not depend on the fitting parameters for mass-defect and electron-phonon scattering, we examine the change in the MFP distribution as τ_{MD}^{-1} and τ_{ep}^{-1} varied by 50% to 200% of their nominal values for nanocrystalline SiGe at room temperature. We find that there is only 3% variation in heat contribution from long MFP phonons due to the change in mass defect scattering magnitude. Similarly, 7% variation is observation when varying τ_{ep}^{-1} using the same method. Thus, our observation of the importance of long MFP phonons is not sensitive to the assumptions made for these scattering mechanisms.

The effects of temperature on the thermal conductivity accumulations for doped nanocrystalline Si/SiGe are shown in Fig. 2.8(a). As the temperature increases, the contribution from long MFP phonons decreases due to the dominance of phonon-phonon scattering. For doped nano-Si (Fig. 2.8(a) & dashed line in Fig. 2.9), at room temperature, about 35% of the total heat is due to phonons with MFPs longer than the grain size while at 1000 K, corresponding to the typical operating temper-

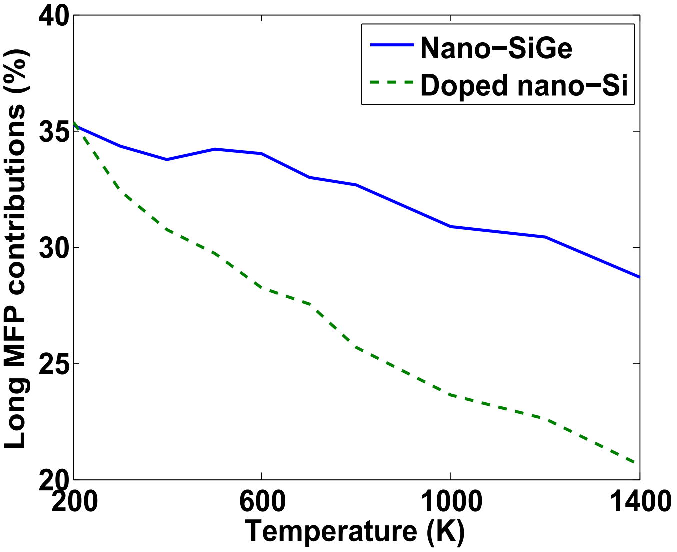

Figure 2.9: Percentage contribution from phonons with MFPs longer than the grain size versus temperature in doped nanocrystalline SiGe (solid line) and doped nanocrystalline Si (dashed line). The percentage contribution decreases as temperature increases but is still considerable at high temperatures.

ature of devices that use Si/SiGe, the percentage contribution decreases to 20%. On the other hand, this dominance shift is less obvious in nanocrystalline SiGe since most of the high frequency phonons, which are more likely to undergo phonon-phonon scattering, are already strongly scattered by the alloy atoms, as shown in Fig. 2.8(b). At 1000 K, the contribution from these long MFP phonons in nano SiGe is still as high as 30% as shown by solid line in Fig. 2.9.

We now examine the effects of grain size on the heat transport in doped nanocrystalline Si/SiGe. Figures 2.10 and 2.11 show the thermal conductivity accumulation versus phonon MFP for doped nanocrystalline Si/SiGe with different grain sizes at 300 K. Since the mass defect scattering strength is different in the two materials, short MFP phonons are less scattered by the mass defects and in general carry more heat in doped nanocrystalline Si than in doped nanocrystalline SiGe. Regardless of the strength of the mass defect scattering, we find an increase in contribution

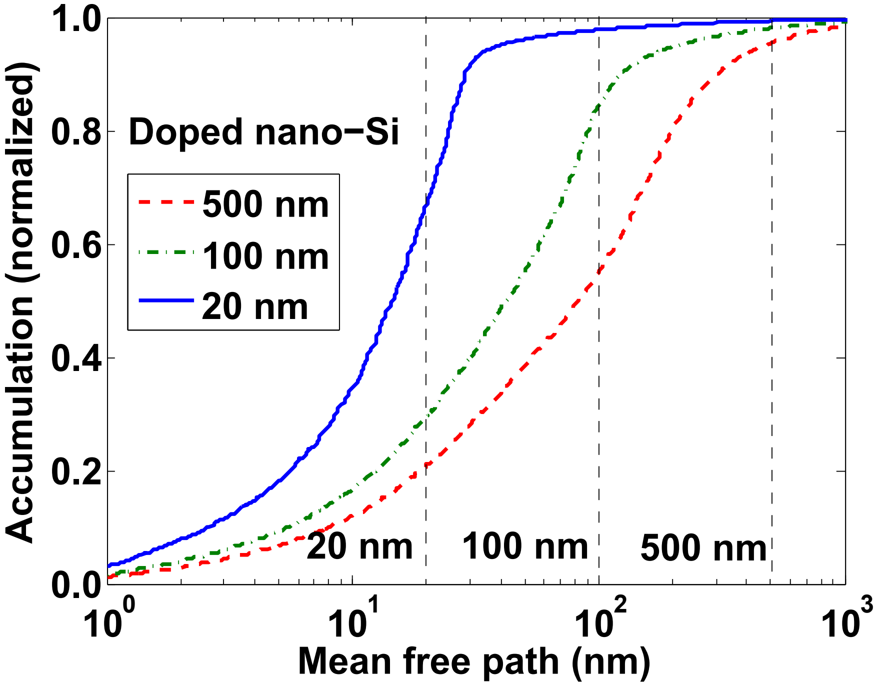

Figure 2.10: Thermal conductivity accumulation for doped nanocrystalline Si at 300 K versus phonon MFP with grain sizes at 20 nm (solid line), 100 nm (dash-dotted line) and 500 nm (dashed line). As the grain size decreases, the distribution shifts to shorter MFPs but the heat contribution from long MFP phonons increases.

from long MFP phonons as the grain size decreases in both materials even though smaller grain sizes result in shorter MFP phonons.

To clearly demonstrate this trend, we plot both thermal conductivity and long MFP contribution versus grain size in Figs. 2.12 & 2.13. Previous studies have shown that decreasing the grain size can effectively reduce the thermal conductivity.(*47*, *48*) The decreasing trend of thermal conductivity as grain size decreases in Fig. 2.12 confirm this observation. As the grain size varies from 550 nm to 20 nm, there is a 30% reduction of thermal conductivity for nanocrystalline SiGe and 45% in doped nanocrystalline Si. Due to the stronger mass defect scattering, the thermal conductivity of nanocrystalline SiGe is more than 50% lower than that of doped nanocrystalline Si at a given grain size. When we look into the contribution to the

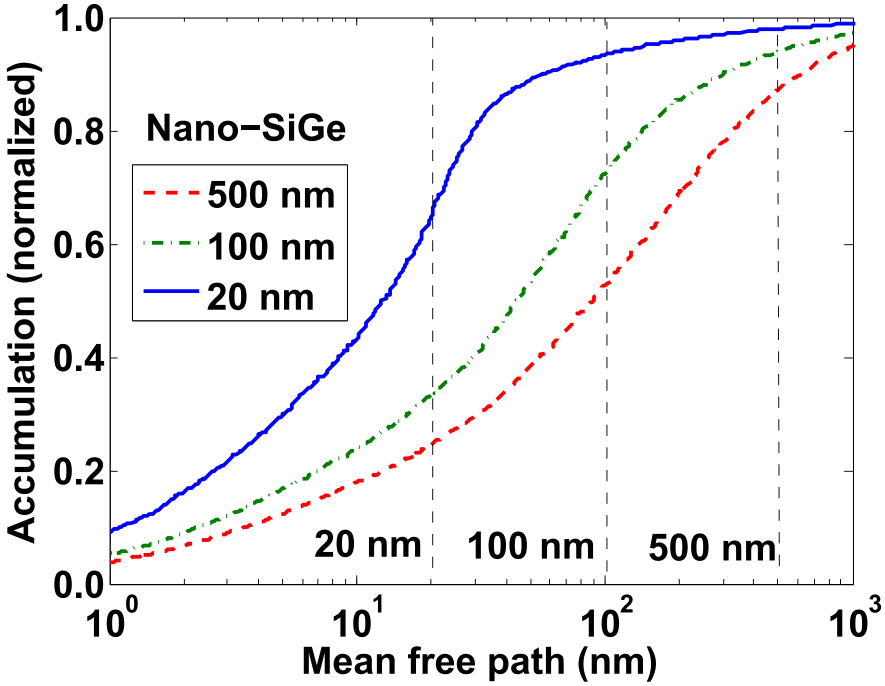

Figure 2.11: Thermal conductivity accumulation for doped nanocrystalline SiGe at 300 K versus phonon MFP with grain sizes at 20 nm (solid line), 100 nm (dash-dotted line), and 500 nm (dashed line). As the grain size decreases, the distribution shifts to shorter MFPs but the heat contribution from long MFP phonons increases.

total thermal conductivity from each phonon mode, we find that, counterintuitively, the contribution from those phonons with MFPs longer than the grain size increases as the grain size decreases as shown in Fig. 2.13. For a 20 nm grain, the contribution from long MFP phonons is as high as 35% in both nanocrystalline Si and SiGe. This result can be explained by the increasing fraction of phonons with MFP that is longer than grain size as the grain size decreases. According to the frequency-dependent transmissivity, those phonons are less affected by the grain boundaries compared to the prediction of the gray model. Therefore, their contribution to the total thermal conductivity increases even though the total thermal conductivity decreases.

These observations indicate that nanocrystalline grain boundaries may not be as ef-

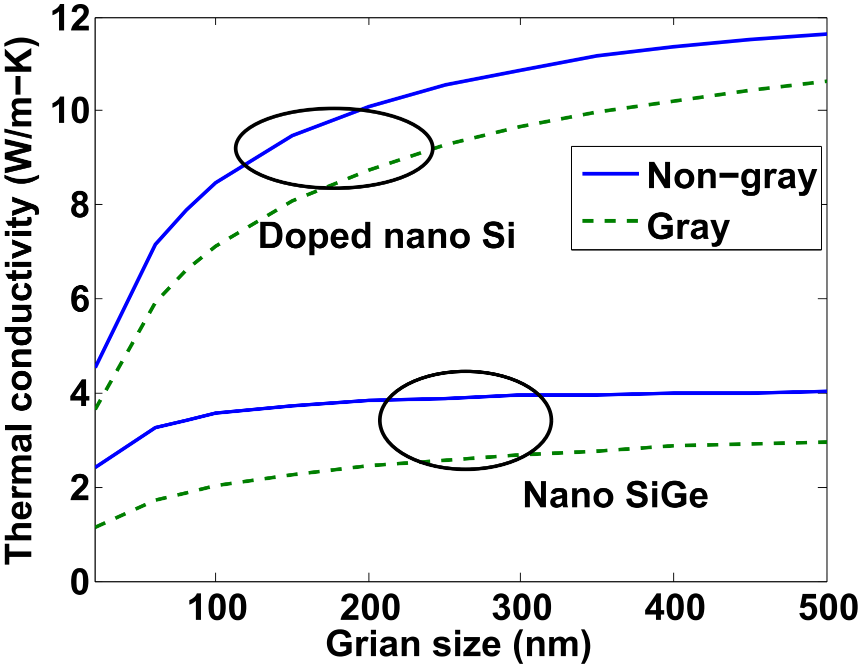

Figure 2.12: Thermal conductivity versus grain size in doped nanocrystalline Si/SiGe using non-gray (solid lines) and gray (dashed lines) models. Thermal conductivity decreases as the grain size decreases, particularly for grains smaller than 100 nm.

fective as previously believed at scattering long MFP phonons. If a grain boundary can be designed such that it diffusely scatters all phonons independent of frequency as in the gray model, an additional reduction in the phonon thermal conductivity can be achieved. In Figs. 2.12 & 2.13, we plot the thermal conductivity and long MFP phonon contribution versus grain size for the gray model with a constant transmissivity of 0.85, corresponding to the smallest value of the transmissivity in the non-gray model. Figure 2.12 shows that thermal conductivity is approximately 12% lower than non-gray model in doped nanocrystalline silicon and 30% lower in doped nanocrystalline SiGe. The higher reduction in SiGe is because long MFP phonons in doped nanocrystalline SiGe, which are strongly scattered by the grain boundary, contribute more to thermal conductivity than in doped nanocrystalline Si.

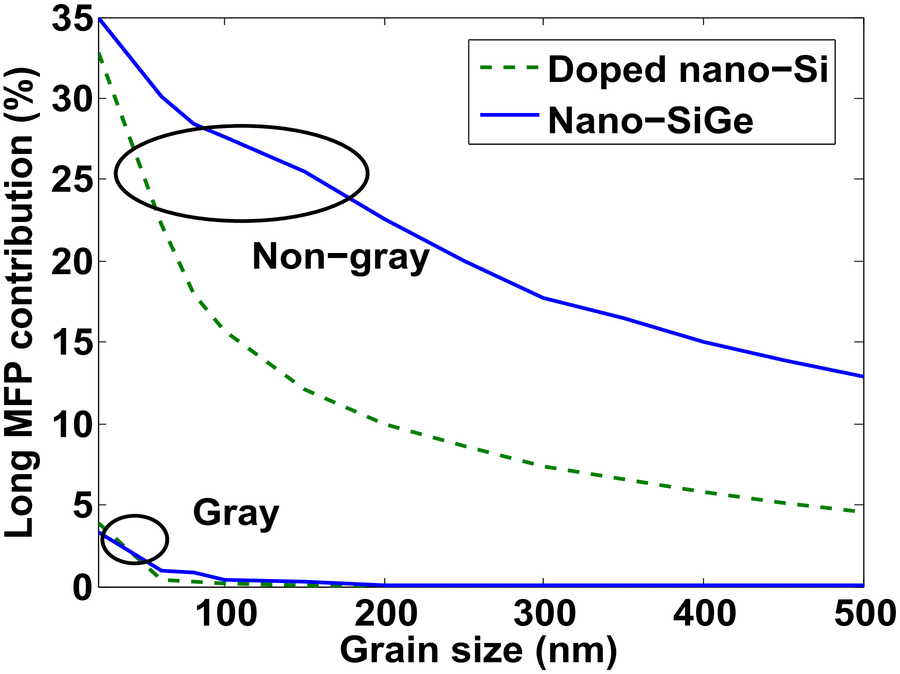

Figure 2.13: Percentage contribution from phonons with MFPs longer than the grain size versus grain size in doped nanocrystalline Si (dashed lines) and doped nanocrystalline SiGe (solid lines) using non-gray and gray models. The contribution from the long MFP phonons increases as grain size decreases.

Figure 2.13 quantifies this reduction in contribution from long MFP phonons. The gray grain boundary scatters most of the long MFP phonons such that their contribution to the total thermal conductivity is negligible. In both doped nanocrystalline Si and SiGe with 20 nm grains, the long MFP contribution is reduced to less than 5%. Further thermal conductivity reduction can be achieved if the transmissivity is further decreased. Therefore, great potential to further increase the thermoelectric performance of nanocrystalline Si/SiGe exists if such grain boundaries can be designed.

2.4 Summary

Nanocrystalline Si and SiGe have great potential as thermoelectrics, but a better understanding of grain boundary scattering is necessary to improve their efficiency. In this chapter, we have studied thermal phonon transport in the full 3D geometry of nanocrystalline Si and SiGe using a novel adjoint variance-reduced energy-based Monte Carlo method. We find that low frequency, long MFP phonons, which are previously predicted to carry negligible heat in the gray model, may still carry a substantial amount of heat due to the frequency-dependent grain boundary scattering. Significant potential to improve the efficiency of nanocrystalline Si and SiGe exists if these phonons can be scattered. Our work provides important insight into how to further increase the thermoelectric performance of nanostructured silicon and silicon-germanium alloys.

While this computational study provides important insights, one issue still remains. Even though the proposed frequency-dependent model reproduces the experimental measurements, the fitting itself is not unique. Since thermal conductivity is a macroscopic property that is integrated over the thermal spectrum, there exists multiple choices of this underlying distribution that result in the same thermal conductivity. Moreover, we do not know the spectral properties of thermal phonons in most of the materials. In the rest part of thesis, we present analytical methods to analyze the heat transport at the nanoscale, which allow us to more directly measure microscopic properties of phonons such as phonon MFP spectra in solids and phonon transmission coefficients at a solid-solid interface. In the next chapter, we will start with analyzing heat conduction at length scale comparable to phonon MFPs using Boltzmann transport equation.

Chapter 3

BOLTZMANN TRANSPORT EQUATION

Chapter 3 has been adapted from:

(*1*) Chengyun Hua and Austin J. Minnich. “Analytical Green’s function of the multidimensional frequency-dependent phonon Boltzmann equation”. In: *Phys. Rev. B* 90 (21 2014), p. 214306. DOI: `10.1103/PhysRevB.90.214306`. URL: `http://link.aps.org/doi/10.1103/PhysRevB.90.214306`.

(*2*) Chengyun Hua and Austin J. Minnich. “Semi-analytical solution to the frequency-dependent Boltzmann transport equation for cross-plane heat conduction in thin films”. In: *Journal of Applied Physics* 117.17, 175306 (2015). DOI: `http://dx.doi.org/10.1063/1.4919432`. URL: `http://scitation.aip.org/content/aip/journal/jap/117/17/10.1063/1.4919432`.

3.1 Introduction

Heat conduction at length scale comparable to phonon wavelengths and mean free paths (MFPs) is of considerable interest recently(*33*) due to its applications in many technologies such as thermoelectrics(*10*, *12*) and electronic devices.(*34*) At these small scales, classic continuum transport theories such as Fourier’s law are not valid due to the absence of scattering and therefore a local temperature.(*35*) In this non-diffusive regime, phonon transport is nonlocal and is described by the Boltzmann transport equation (BTE).(*21*)

Although numerical approaches such as the variance-reduced Monte Carlo methods introduced in Chapter 2 could efficiently solve the frequency-dependent BTE in a large, complex geometry with minimal memory requirements, analytical solutions to the BTE could enable physical insights to be obtained just from examining the form of the equation, which is not immediately accessible from the numerical solutions. So far no analytical solutions to the BTE that could rigorously include the frequency dependence of thermal phonons have been reported.

Here, we report two analytical methods to solve the multidimensional, frequency-dependent transient BTE subject to different boundary conditions. Both methods allow us to obtain simple, closed-form solutions to complex multidimensional problems that have previously been possible to solve only with computationally expensive numerical simulations and will enable a better understanding of nondiffusive heat conduction.

3.2 Analytical Green's function of BTE

In this section, we demonstrate that exact analytical solutions to the multidimensional, frequency-dependent transient BTE for arbitrary heat inputs can be obtained using Fourier transforms in infinite or semi-infinite domains.

Derivation

The frequency-dependent BTE under relaxation time approximation is given by:

$$\frac{\partial g_\omega}{\partial t} + \mathbf{v}_g \cdot \nabla g_\omega - \frac{Q_\omega}{4\pi} = -\frac{g_\omega - g_0(T)}{\tau(\omega, T)}, \tag{3.1}$$

where $g_\omega = \hbar\omega D(\omega)(f_\omega(x,t,\theta) - f_0(T_0))$ is the desired deviational distribution function, $g_0(T)$ is the equilibrium deviational distribution function defined below, $Q_\omega(\mathbf{r}, t)$ is the spectral volumetric heat generation, $\mathbf{v}_g(\omega, T)$ is the phonon group velocity, and $\tau(\omega, T)$ is the phonon relaxation time. Here, $\mathbf{r}$ is the spatial vector, t is the time, ω is the phonon frequency, and T is the temperature. In the Cartesian coordinate system and assuming an isotropical crystal, the advection term in Eq. (3.1) is expanded as

$$\mathbf{v}_g \cdot \nabla g_\omega = v_g \mu \frac{\partial g_\omega}{\partial z} + v_g \sqrt{1-\mu^2}\cos\phi \frac{\partial g_\omega}{\partial x} + v_g \sqrt{1-\mu^2}\sin\phi \frac{\partial g_\omega}{\partial y}, \tag{3.2}$$

where $\mu = cos(\theta)$ is the directional cosine of the polar angle θ and ϕ is the azimuthal angle. Here, we emphasize that while many crystals contain minor anisotropies in the Brillouin zone, the vast majority of crystals are thermally isotropic, with notable exceptions being materials with very anisotropic bonding such as graphite. We present a validation of this assertion for the ab-initio calculations for silicon used here in Appendix C.

Assuming a small temperature rise, $\Delta T = T - T_0$, relative to a reference temperature, T_0, the equilibrium deviational distribution is proportional to ΔT,

$$g_0(T) = \frac{1}{4\pi}\hbar\omega D(\omega)(f_{BE}(T) - f_{BE}(T_0)) \approx \frac{1}{4\pi}C_\omega \Delta T. \tag{3.3}$$

Here, $\hbar$ is the reduced Planck constant, $D(\omega)$ is the phonon density of states, f_{BE} is the Bose-Einstein distribution, and $C_\omega = \hbar\omega D(\omega)\frac{\partial f_{BE}}{\partial T}$ is the mode specific heat. The volumetric heat capacity is then given by $C = \int_0^{\omega_m} C_\omega d\omega$ and the thermal conductivity $k = \int_0^{\omega_m} k_\omega d\omega$, where $k_\omega = \frac{1}{3}C_\omega v_\omega \Lambda_\omega$ and $\Lambda_\omega = \tau_\omega v_\omega$ is the phonon MFP.

Both g_ω and ΔT are unknown. Therefore to close the problem, we need to relate g_ω to ΔT. Notice that when intergrating over solid angle and phonon frequency, the left hand side of Eq. (3.1) becomes

$$\frac{\partial E}{\partial t} + \nabla \cdot \mathbf{q} - Q,$$

where $E = \int \int_0^{\omega_m} g_\omega d\omega d\Omega$ is the energy, $\mathbf{q} = \int \int_0^{\omega_m} \mathbf{v} g_\omega d\omega d\Omega$ is the heat flux, and $Q = \int \int_0^{\omega_m} Q_\omega d\omega d\Omega$ is the volumetric heat generation. This expression represents the general law of energy conversation and always equals to zero. Thefore, the energy conversation requires that the right hand side of Eq. (3.1) becomes

$$\int \int_0^{\omega_m} \left[\frac{g_\omega(\mathbf{r},t)}{\tau_\omega} - \frac{1}{4\pi}\frac{C_\omega}{\tau_\omega}\Delta T(\mathbf{r},t)\right] d\omega d\Omega = 0, \tag{3.4}$$

where Ω is the solid angle in spherical coordinates and ω_m is the cut-off frequency. Note that summation over phonon branches is implied without an explicit summation sign whenever an integration over phonon frequency is performed.

Let us now consider solving this equation in an infinite domain or a semi-infinite domain with specular boundary conditions such that the domain can be extended to infinity by symmetry. This assumption eliminates the consideration of diffuse boundaries but still leaves a wide range of problems that can be solved. In such a domain, a Fourier transform can be applied to all spatial coordinates as well as the time variable, giving:

$$(i\eta + v_g\mu i\xi_z + v_g\sqrt{1-\mu^2}\cos\phi i\xi_x + v_g\sqrt{1-\mu^2}\sin\phi i\xi_y)\widetilde{g_\omega} = -\frac{\widetilde{g_\omega}}{\tau_\omega} + \frac{C_\omega}{4\pi\tau_\omega}\Delta\widetilde{T} + \frac{\widetilde{Q_\omega}}{4\pi}, \tag{3.5}$$

where $\widetilde{\ }$ indicates the function is in its Fourier transform form. Here, we define the temporal frequency as η and the spatial wavevector in x, y and z as ξ_x, ξ_y, and ξ_z, respectively.

After rearranging Eq. (3.5), the unknown distribution function is written as

$$\widetilde{g_\omega} = \frac{C_\omega}{4\pi}\frac{\Delta\widetilde{T} + \widetilde{Q_\omega}\tau_\omega/C_\omega}{1 + i\eta\tau_\omega + i\mu\xi_z\Lambda_\omega + i\sqrt{1-\mu^2}(\cos\phi\xi_x\Lambda_\omega + \sin\phi\xi_y\Lambda_\omega)}. \tag{3.6}$$

Plugging Eq. (3.6) into Eq. (3.4), an equation for temperature can be obtained

$$4\pi\Delta\widetilde{T}\int_0^{\omega_m}\frac{C_\omega}{\tau_\omega}d\omega \tag{3.7}$$

$$= \int_0^{\omega_m}\int_0^{2\pi}\int_{-1}^{1}\frac{C_\omega}{\tau_\omega}\frac{\Delta\widetilde{T} + \widetilde{Q_\omega}\tau_\omega/C_\omega}{1 + i\eta\tau_\omega + i\mu\Lambda_\omega\xi_z + i\sqrt{1-\mu^2}(\cos\phi\xi_x\Lambda_\omega + \sin\phi\xi_y\Lambda_\omega)}d\mu d\phi d\omega.$$

The angle integrals on the right hand side of Eq. (3.7) can in fact be analytically evaluated using the identities 2.558-4 and 2.261 in Ref. (*87*). Therefore, a simple closed form of temperature in Fourier space can be obtained

$$\Delta\widetilde{T}(\eta,\xi_x,\xi_y,\xi_z) = \frac{\int_0^{\omega_m}\frac{\widetilde{Q_\omega}}{\Lambda_\omega\xi}\tan^{-1}\left(\frac{\Lambda_\omega\xi}{1+i\eta\tau_\omega}\right)d\omega}{\int_0^{\omega_m}\frac{C_\omega}{\tau_\omega}\left[1 - \frac{1}{\Lambda_\omega\xi}\tan^{-1}\left(\frac{\Lambda_\omega\xi}{1+i\eta\tau_\omega}\right)\right]d\omega}, \tag{3.8}$$

where $\xi = \sqrt{\xi_x^2 + \xi_y^2 + \xi_z^2}$. Note that if the spectral volumetric heat generation Q_ω is a Dirac-delta function in time and space, Eq. (3.8) becomes the impulse temperature response or the Green's function of the frequency dependent BTE. Once $\Delta\widetilde{T}$

is determined, $\widetilde{g}_\omega$ can be obtained by Eq. (3.6). The spectral heat flux is calculated as $\widetilde{\mathbf{q}}_\omega = \int \widetilde{g}_\omega v_g d^{\cdot}$, thus closing the problem. Solutions to each of these quantities in the real-space solution can be easily obtained by inverse Fourier transform.

We next confirm that our solution reduces to the Green's function of the diffusive and ballistic regimes. These regimes can be specified by the two non-dimensional parameters, the Knudsen number $\mathrm{Kn}_\omega = \xi \Lambda_\omega$ and transient number $\Gamma_\omega = \eta \tau_\omega$ in Eq. (3.8). In the diffusive limit, length and time scales are much larger than the phonon MFPs and relaxation times, respectively, corresponding to $\mathrm{Kn}_\omega \ll 1$ and $\Gamma_\omega \ll 1$. Examining Eq. (3.8) under this limit, we find that in Eq. (3.8)

$$\frac{1}{\Lambda_\omega \xi} \tan^{-1}\left(\frac{\Lambda_\omega \xi}{1 + i\eta\tau_\omega}\right) \sim 1 - i\eta\tau_\omega + \frac{1}{3}\Lambda_\omega^2 \xi^2, \tag{3.9}$$

and the solution reduces to the Fourier solution, given by

$$\Delta \widetilde{T}_f \approx \frac{\widetilde{Q}_0}{i\eta C + \xi^2 k}, \tag{3.10}$$

where $\widetilde{Q}_0 = \int_0^{\omega_m} \widetilde{Q}_\omega d\omega$. In the ballistic regime, lengths and times are much smaller than MFPs and relaxation times, or $\mathrm{Kn}_\omega \gg 1$ and $\Gamma_\omega \gg 1$. The BTE thus becomes

$$\frac{\partial g_\omega}{\partial t} + \mathbf{v}_g \cdot \nabla g_\omega = 0, \tag{3.11}$$

the solution of which is the same as Eq. (3.8) under the limit of $\tau_\omega \to \infty$, given by

$$\Delta \widetilde{T}_b \approx \frac{1}{\int_0^{\omega_m} \frac{C_\omega}{\tau_\omega} d\omega} \int_0^{\omega_m} \frac{\widetilde{Q}_\omega}{\Lambda_\omega \xi} \tan^{-1}\left(\frac{v_\omega \xi}{i\eta}\right) d\omega. \tag{3.12}$$

Between these two limits is the quasiballistic regime for we must use the full expression given by Eq. (3.8).

Advantages of the method

The BTE has long been a formidable equation due to its high dimensionality and the efficient solution of this equation has been a long-standing challenge in the thermal sciences. Prior solution approaches in the thermal science literature are either extremely simplified or solely numerical and usually computationally expensive. Independent of any numerical considerations, this identification of an analytical solution to BTE that enables physical insight to be obtained just from examining the form of the equation is a useful advance.

Further, the computational effort to obtain a solution for a specific problem is dramatically reduced as compared to that of discrete ordinates which have been typically used in the past. For example, the typical computational time for a problem with a heat impulse in a semi-infinite substrate using discrete ordinates(*79*) is on the order of five hours while our approach takes less than five seconds, a speedup exceeding three orders of magnitude. Furthermore, our result is valid for transient heat conduction in all three dimensions, a situation that has rarely been considered even numerically as the memory requirements for discrete ordinates in multiple dimensions are prohibitively large.

Applications

We now demonstrate the utility of our solution by solving three multidimensional problems for which the only previous solution methods were computationally expensive numerical approaches. We perform our calculations for crystalline silicon, using the density functional theory (DFT) dispersion and lifetimes calculated by J. Carrete and N. Mingo using ShengBTE (*88*, *89*) and Phonopy(*90*) from interatomic force constants obtained with VASP.(*91–94*) The details about converting the *ab initio* calculations to isotropic dispersion can be found in Appendix C.

The first case we consider here is the transient temperature decay of an infinite silicon crystal subject to a heat impulse with a Gaussian spatial profile. The spectral volume heat generation is given by:

$$Q_\omega(x,y,z,t) = \Delta T(0) C_\omega e^{-\pi \frac{x^2+y^2+z^2}{R^2}} \delta(t), \tag{3.13}$$

where R is the radius of the Gaussian profile as illustrated in the inset of Fig. 3.1. To

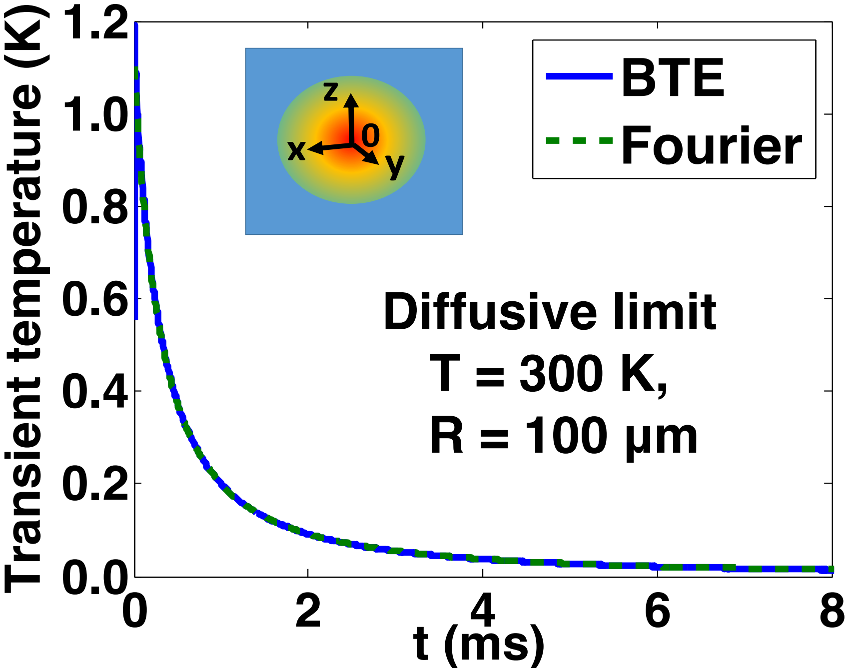

Figure 3.1: Temperature decay curves $\Delta T(t)$ at the origin for an infinite silicon sample subject to an impulsive volumetric heat generation with Gaussian spatial profile at the origin in the diffusive limit. The BTE and Fourier solutions are given by the solid lines and dashed lines respectively. Inset: 2D schematic of the domain. R is the Gaussian radius.

simplify the analytical expressions, we choose the amplitude of spectral distribution of heat generation to be $\Delta T(0)C_\omega$ corresponding to a thermal distribution. Note that this spectral distribution of heat generation can be varied according to the different circumstances.

After transforming Eq. (3.13) into Fourier space and inserting into Eq. (3.8), we obtain the temperature profile in Fourier space, given by

$$\Delta\widetilde{T}(\eta,\xi_x,\xi_y,\xi_z) = \Delta T(0)R^3 e^{-\frac{R^2\xi^2}{4\pi}} \frac{\int_0^{\omega_m} C_\omega \frac{1}{\Lambda_\omega \xi}\tan^{-1}\left(\frac{\Lambda_\omega \xi}{1+i\eta\tau_\omega}\right) d\omega}{\int_0^{\omega_m} \frac{C_\omega}{\tau_\omega}\left[1-\frac{1}{\Lambda_\omega \xi}\tan^{-1}\left(\frac{\Lambda_\omega \xi}{1+i\eta\tau_\omega}\right)\right] d\omega}. \tag{3.14}$$

Now, we examine how temperature decays with time at the origin. We note that to obtain this quantity it is not necessary to inverse Fourier transform the three spatial wavevectors. Instead, we evaluate the Fourier transform only at $x = y = z = 0$ by integrating Eq. (3.8) over all wavevectors as

$$\Delta\widetilde{T}(\eta, \mathbf{r} = 0) = \frac{1}{(2\pi)^3} \int_{-\infty}^{\infty} \int_{-\infty}^{\infty} \int_{-\infty}^{\infty} \Delta\widetilde{T}(\eta, \xi_x, \xi_y, \xi_z) d\xi_x d\xi_y d\xi_z. \tag{3.15}$$

In this way, only one inverse Fourier transform over the frequency variable is required to obtain the temperature decay.

The resulting transient temperature decay curves are plotted in Figs. 3.1 & 3.2. In the diffusive limit where the heat generation region is big enough such that $\mathrm{Kn}_\omega \ll 1$ and $\Gamma_\omega \ll 1$, the BTE solution recovers the Fourier's law solution as in Fig. 3.1. As the Gaussian radius R decreases and MFPs become comparable or greater than R, we observe a deviation of the BTE solution from the Fourier's law due to quasiballistic transport, as shown in Fig. 3.2(a). We note that the actual temperature rise is larger than the Fourier's law prediction, consistent with a prior result by Chen.(*40*) The ballistic limit is plotted in Fig. 3.2(b), demonstrating that the calculated temperature decay agrees with the ballistic solution of the BTE given by Eq. (3.12).

The second case we consider is a line heater on a semi-infinite silicon substrate as illustrated in the inset of Fig. 3.3(a), where x is the in-plane direction and z is the cross-plane direction. The surface of the sample is subject to a periodic line heating with width L in the x direction, exponential decay with penetration depth δ in the z direction, and temporal frequency η. We assume that phonons at $z = 0$ are specularly reflected, leading to the adiabatic boundary condition $g_\omega(z = 0, x, t, \mu) = g_\omega(z = 0, x, t, -\mu)$. Therefore, by symmetry we can extend the domain to the negative z plane and apply our solution.

The spectral volumetric heat generation in this case is expressed as

$$Q_\omega(x, z, t) = \Delta T(0) C_\omega e^{i\eta t} e^{-|z|/\delta} \left[H\left(x + \frac{L}{2}\right) - H\left(x - \frac{L}{2}\right) \right], \tag{3.16}$$

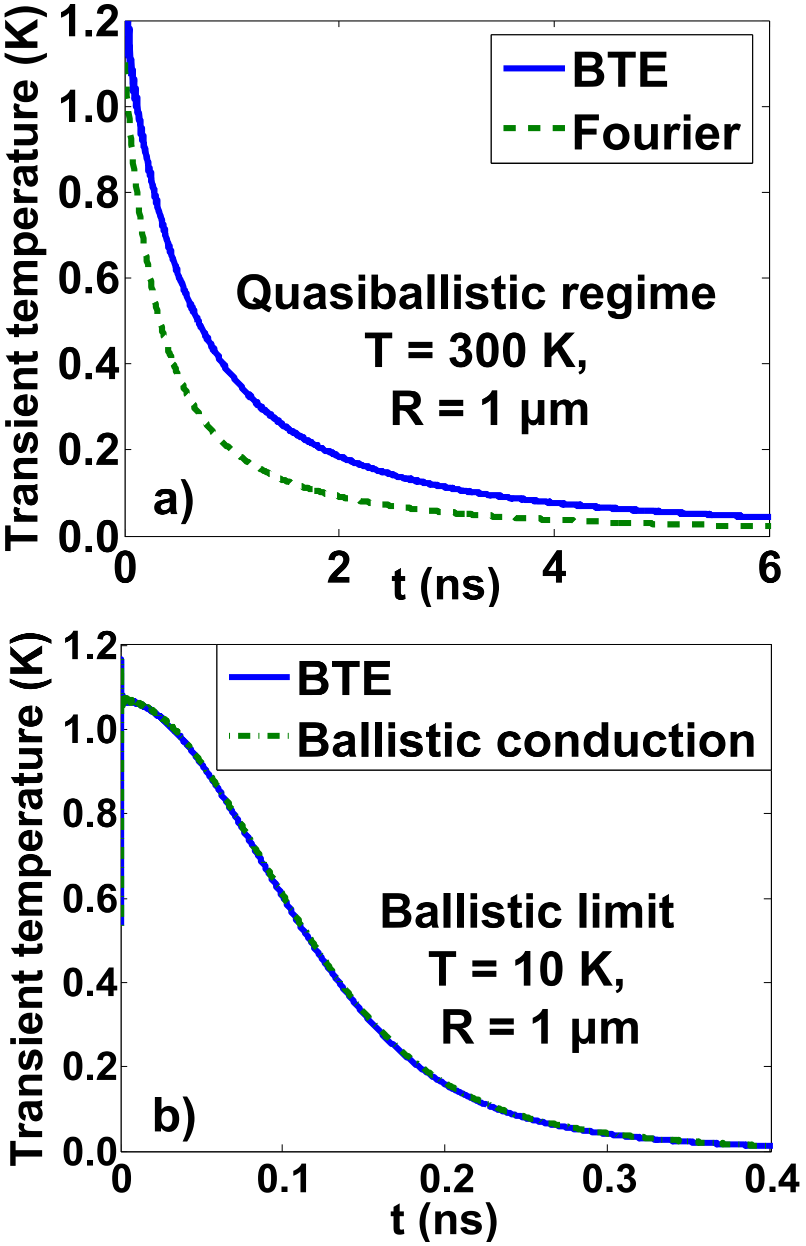

Figure 3.2: Temperature decay curves $\Delta T(t)$ at the origin for an infinite silicon sample subject to an impulsive volumetric heat generation with Gaussian spatial profile at the origin in (a) the quasiballistic regime and (b) the ballistic limit. The BTE, Fourier, and ballistic conduction solutions are given by the solid lines, dashed lines, and dash-dotted lines respectively.

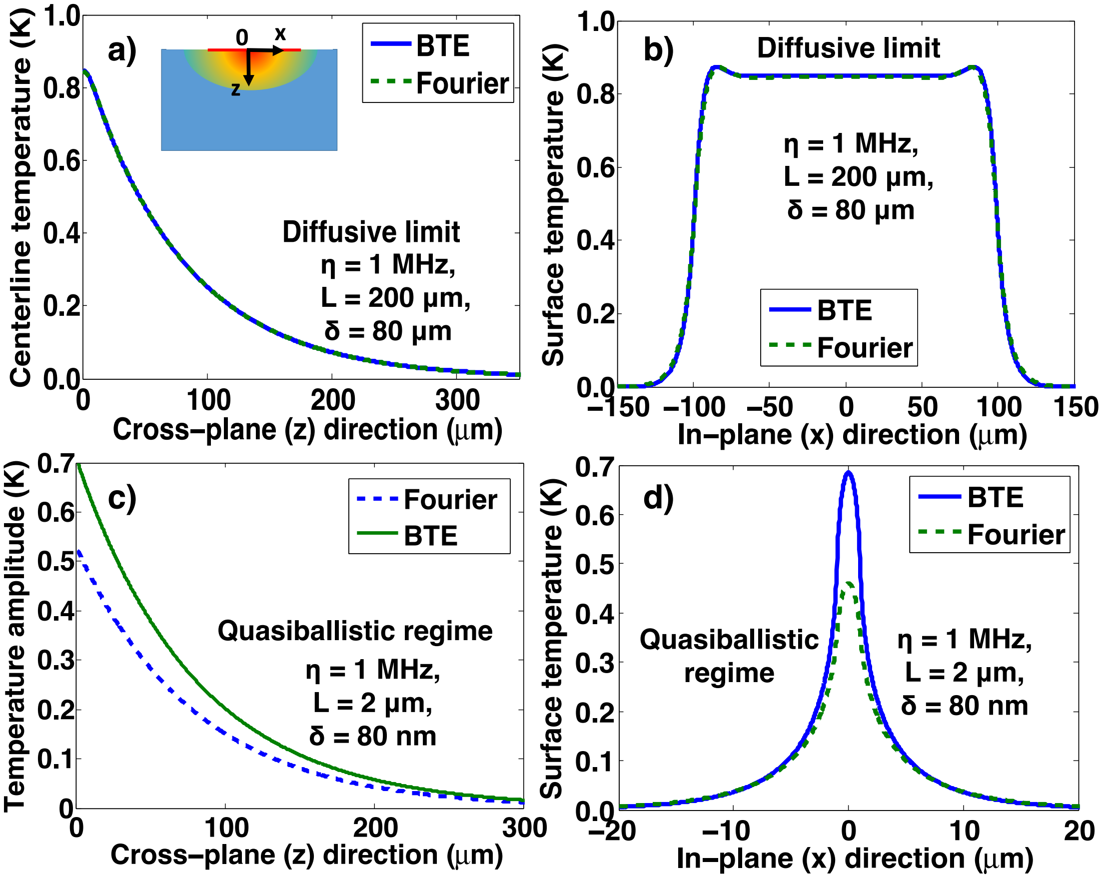

Figure 3.3: Amplitudes of the temperature decay curves $|\Delta T|$ for a planar semi-infinite silicon sample subject to a periodic line heater at the surface. ((a) & (b)) are in diffusive while ((c) & (d)) are in quasiballistic regime. The BTE and Fourier solutions are given by the solid and dashed lines, respectively. Inset in (a): 2D schematic of the geometry. Phonons incident on the plane at $z = 0$ are specularly reflected. The width of line heater is L with an exponential decay with penetration depth δ in the cross-plane direction, and η is the temporal frequency.

where H is the Heaviside step function. The same procedure as in the first case is carried out to obtain the temperature in Fourier space, which is given by

$$\Delta\widetilde{T}(\eta,\xi_x,\xi_y,\xi_z) = \Delta T(0)\frac{2\delta}{1+\delta^2\xi^2} L\mathrm{sinc}\left(\frac{\xi_x L}{2}\right) \frac{\int_0^{\omega_m} C_\omega \frac{1}{\Lambda_\omega\xi}\tan^{-1}\left(\frac{\Lambda_\omega \xi}{1+i\eta\tau_\omega}\right)d\omega}{\int_0^{\omega_m}\frac{C_\omega}{\tau_\omega}\left[1-\frac{1}{\Lambda_\omega\xi}\tan^{-1}\left(\frac{\Lambda_\omega\xi}{1+i\eta\tau_\omega}\right)\right]d\omega}. \tag{3.17}$$

Since the heating is periodic in time, the temperature profile is quasi-stationary. We obtain the centerline temperature ($T(x=0,z)$) by integrating Eq. (3.17) over all ξ_x and the surface temperature ($T(x,z=0)$) by integrating Eq. (3.17) over all ξ_z.

The centerline temperature amplitudes are shown in Figs. 3.3 (a) & (b), and the surface temperature amplitudes are shown in Figs. 3.3 (b) & (d). Again, in the diffusive limit, the BTE solutions agree with the Fourier solutions when the heating length is much larger than the phonon MFPs such that $\mathrm{Kn}_\omega \ll 1$ and $\Gamma_\omega \ll 1$. The phonon transport becomes quasiballistic when the MFPs are comparable to or greater than the characteristic length scales in which case the BTE solutions no longer agree with the Fourier's law solutions. We again observe that the BTE solution predicts a higher temperature rise than the Fourier's law in the quasiballistic case due to a lack of scattering local to the heater.

The last case we consider here is a steady displaced planar Gaussian heating source next to an adiabatic specularly reflecting corner as illustrated in Fig. 3.4. While this geometry is complex, the problem can be effectively solved using the method of images as in elementary electrostatics.(*95*) To implement the method of images, we replace the specular boundaries with three identical heating sources located at the mirror locations across each symmetry plane. By symmetry and uniqueness of the solution for the linear BTE, this solution is equal to that of the original problem. The method of images is a general technique that can be easily applied to even more complex geometries than that considered here.

The spectral volumetric heat generation for the original and mirror heaters can be expressed as

$$Q_\omega(x,z,t) = \Delta T(0) C_\omega \left(f(x,z) + f(-x,-z) + f(x,-z) + f(-x,z) \right), \qquad (3.18)$$

where $f(x,z) = e^{-\pi \frac{(x-L)^2+(z-L)^2}{R^2}}$, L is the displaced distance from the center of the heat to z/x axis, and R is the radius of the Gaussian profile.

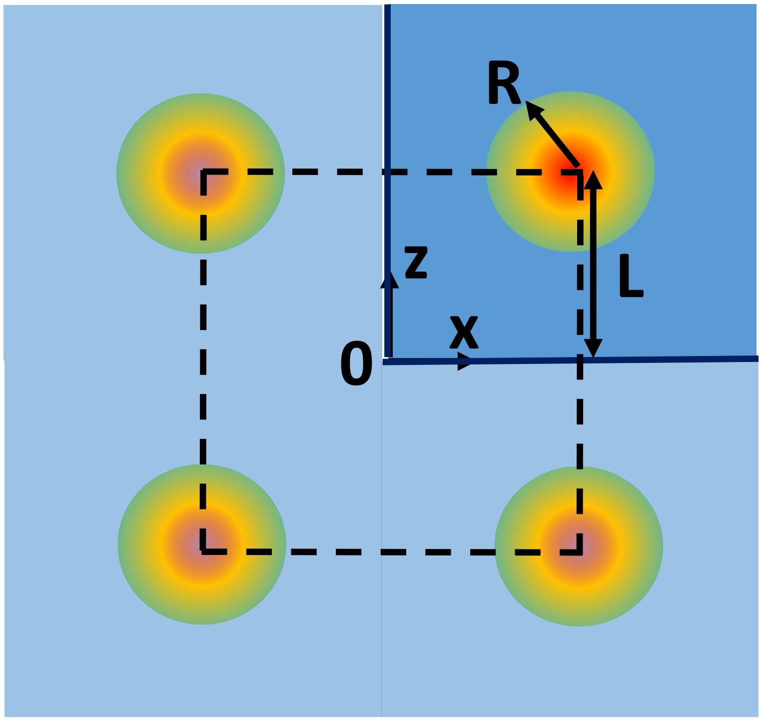

Figure 3.4: A planar domain located in the first quadrant subject to an Gaussian volumetric heat generation displaced away from the origin. The heating profile is uniform in the cross-plane direction. The radius of the Gaussian profile is R and the distance from the center of the heat to x/z axis is L. The problem is treated using the method of images in which the specular boundaries at $z = 0$ and $x = 0$ are replaced with three identical heating sources located at the mirror locations across each symmetry plane.

Figs. 3.5(a) & (b) give the amplitude of the temperature field when the heater is placed 10 μm away from both x and z axes based on the BTE and Fourier's law respectively. At the given the Gaussian radius ($R = 1$ μm), the phonon transport is quasiballistic. The peak amplitude of temperature predicted by the BTE is higher than that of Fourier's law. Also, due to a lack of scattering events local to the heater, heat is trapped around the heating source while it diffuses away from the heater by

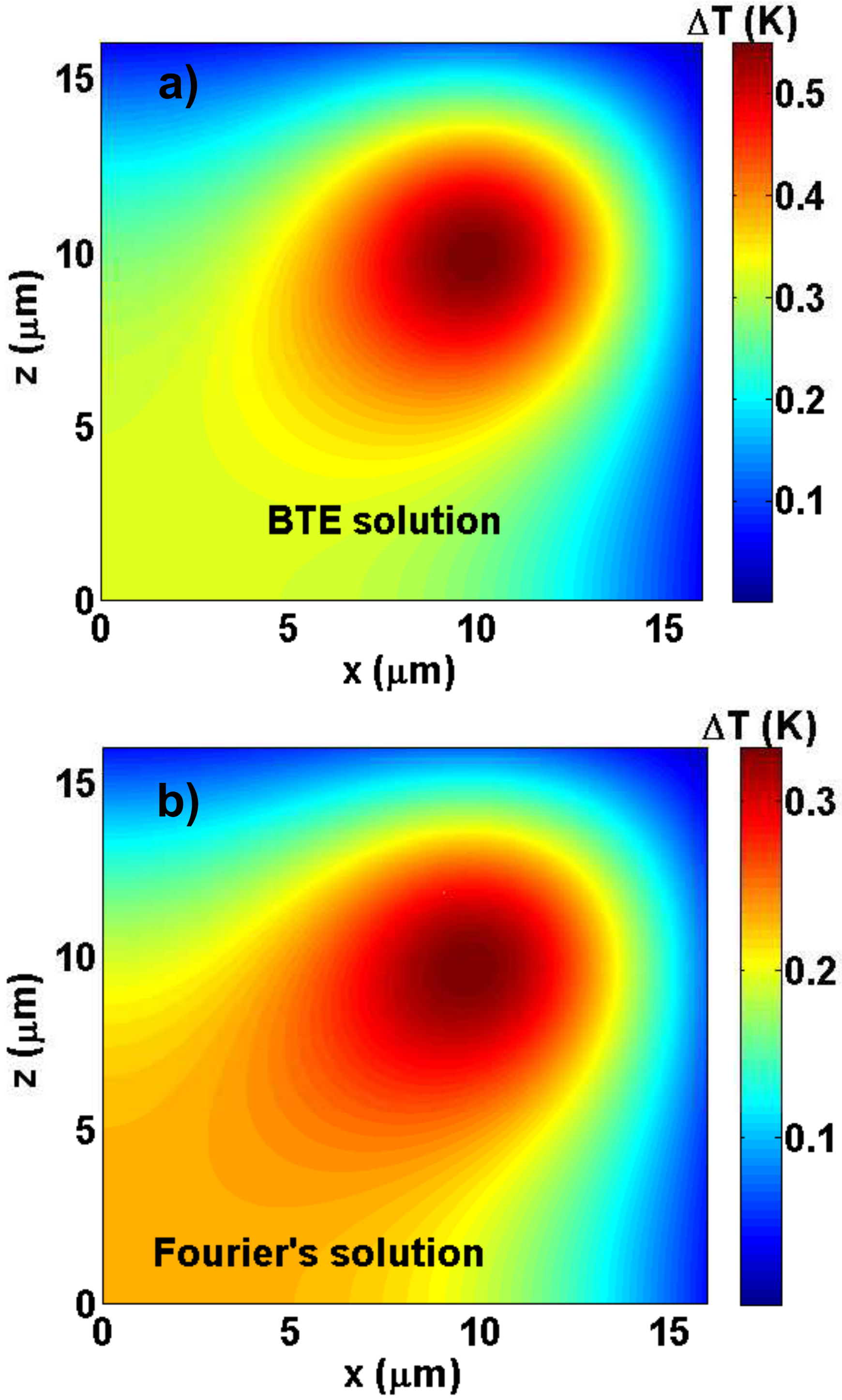

Figure 3.5: Amplitude of 2D temperature field $|\Delta T(x, z)|$ given by (a) the BTE and (b) Fourier's law in the quasiballistic regime with $L = 10\ \mu m$ and $R = 1\ \mu m$.

Fourier's prediction. In the past, the only method to solve this problem was purely numerical. Using our solution, we can write the exact solution in Fourier space, and we can obtain the real-space solution including frequency-dependent phonon properties in under one minute on a typical desktop computer.

3.3 BTE solutions in thin films

In this section, we consider crystals with finite thickness. In the past two decades, thermal transport in thin solid films with thicknesses from tens of nanometers to micrometers has become a topic of considerable importance.(*33*, *96–98*) Such films are used in applications ranging from quantum well lasers to electronic devices.(*99–101*) For example, boundary scattering in these films leads to reduced thermal conductivity that results in the inefficient removal of heat in GaN transistors and LEDs.(*8*, *102*, *103*) To address these and other problems, it is first necessary to understand the fundamental physics of heat conduction in micro-scale solid thin films.

Heat transport in thin films with thicknesses comparable to the phonon mean free paths (MFPs) is governed by the Boltzmann transport equation (BTE), which is an integro-differential equation of time, real space, and phase space. Due to its high dimensionality, it is in general very challenging to solve. For transport along the thin film, an analytical solution can be easily derived by assuming that the characteristic length scale of the thermal gradient is much longer than the phonon MFPs. Analytical solutions were derived for electron transport by Fuchs and Sondheimer with partially specular and partially diffuse boundary scattering.(*104*, *105*) Later, the Fuchs-Sondheimer solutions were extended to phonon thermal transport assuming an average phonon MFP, enabling the calculation of thermal conductivity as a function of the film thickness.(*106*, *107*) Mazumder and Majumdar used a Monte-Carlo method to study the phonon transport along a silicon thin film including phonon dispersion and polarizations.(*108*)

Heat conduction perpendicular to the thin film (cross-plane direction) is much more challenging. In other fields such as neutron transport and thermal radiation, solutions to the BTE for a slab geometry have been obtained using an invariant embedding method,(*109*, *110*) an iterative method(*111*), and an eigenfunction expansion approach.(*112*) For heat conduction, Majumdar numerically solved the gray phonon Boltzmann transport using a discrete-ordinate method by assuming that the two surfaces of the film were black phonon emitters.(*35*) Later, Joshi and Majumdar developed an equation of phonon radiative transfer for both steady-state and transient cases, which showed the correct limiting behavior for both purely ballistic and diffusive transport.(*69*) Chen and Tien applied solutions from radiative heat transfer to calculate the thermal conductivity of a thin film attached to two thermal reservoirs.(*106*) Chen obtained approximate analytical solutions of the BTE to study ballistic phonon transport in the cross-plane direction of superlattices and addressed the inconsistent use of temperature definition at the interfaces.(*113*) Cross-plane heat conduction using a consistent temperature definition was then re-investigated by Chen and Zeng.(*114*, *115*)

Despite these extensive efforts to study transport in thin films based on the BTE, solutions for the cross-plane geometry are still only available with expensive numerical calculations. For example, no analogous Fuchs-Sondheimer formula for the in-plane thermal conductivity exists for the cross-plane direction. Furthermore, most of the previous approaches assumed a single phonon MFP even though recent work has demonstrated that the transport properties of phonons in solids vary widely over the broad thermal spectrum.(*63*, *70*) Incorporating frequency-dependent phonon properties with these prior numerical methods is extremely computationally expensive.

Here, we present a semi-analytical solution of the frequency-dependent transient BTE using the method of degenerate kernels, also known as a series expansion method.(*116*) Our approach is valid from the diffusive to ballistic transport regimes, is capable of incorporating a variety of boundary conditions, and is more than three orders of magnitude faster than prior numerical approaches. Further, we obtain a simple closed-form expression for cross-plane thermal conductivity, analogous to the Fuch-Sondheimer formula for the in-plane thermal conductivity, which enables the cross-plane thermal conductivity of a thin film to be easily calculated. Our results can be applied to efficiently solve heat conduction problems in numerous practical geometries such as superlattices and the thin films used in thermoreflectance experiments while rigorously incorporating the full phonon dispersion.

Method

We start with Eq. 3.1 and assume a small temperature rise, $\Delta T = T - T_0$, relative to a reference temperature, T_0. The one-dimensional (1D) frequency-dependent BTE for an isotropic crystal under the relaxation time approximation becomes:

$$\frac{\partial g_\omega}{\partial t} + v_g \mu \frac{\partial g_\omega}{\partial x} = -\frac{g_\omega}{\tau_\omega} + \frac{1}{4\pi}\frac{C_\omega}{\tau_\omega}\Delta T + \frac{Q_\omega}{4\pi}. \tag{3.19}$$

Again, to close the problem, energy conservation is used to relate g_ω to ΔT, given by

$$\int\int_0^{\omega_m}\left[\frac{g_\omega(x,t)}{\tau_\omega} - \frac{1}{4\pi}\frac{C_\omega}{\tau_\omega}\Delta T(x,t)\right] d\omega d\Omega = 0. \tag{3.20}$$

To solve this equation, we first transform it into an inhomogeneous first-order differential equation by applying a Fourier transform to the time variable, giving:

$$i\eta\widetilde{g}_\omega + v_g \mu \frac{d\widetilde{g}_\omega}{dx} = -\frac{\widetilde{g}_\omega}{\tau_\omega} + \frac{C_\omega}{\tau_\omega}\frac{\Delta\widetilde{T}}{4\pi} + \frac{\widetilde{Q}_\omega}{4\pi}, \tag{3.21}$$

where η is the temporal frequency. This equation has the general solution:

$$\begin{aligned}\widetilde{g}^+_\omega(x) &= P_\omega e^{-\frac{\gamma_\omega}{\mu}x} + \int_0^x \frac{\Gamma(x')}{\mu} e^{\frac{\gamma_\omega}{\mu}(x'-x)} dx' \; (\mu \in (0,1]) && (3.22)\\ \widetilde{g}^-_\omega(x) &= B_\omega e^{\frac{\gamma_\omega}{\mu}(L-x)} - \int_x^L \frac{\Gamma(x')}{\mu} e^{\frac{\gamma_\omega}{\mu}(x'-x)} dx' \; (\mu \in [-1,0]), && (3.23)\end{aligned}$$

where $\Gamma(x') = \frac{C_\omega \Delta\widetilde{T}(x') + \widetilde{Q}_\omega(x')\tau_\omega}{4\pi\Lambda_\omega}$, $\gamma_\omega = (1 + i\eta\tau_\omega)/\Lambda_\omega$, L is the distance between the two walls, and P_ω and B_ω are the unknown coefficients determined by the boundary conditions. Here, $\widetilde{g}^+(x)$ indicates the forward-going phonons and $\widetilde{g}^-(x)$ the backward-going phonons. In this work, $\widetilde{g}^+(x)$ is specified at one of the two walls and $\widetilde{g}^-(x)$ is specified at the other.

Let us assume that the two boundaries are nonblack but diffuse with wall temperature ΔT_1 and ΔT_2, respectively. The boundary conditions can be written as:

$$\begin{aligned}\widetilde{g}^+_\omega(x=0) &= P_\omega = \epsilon_1 \frac{C_\omega}{4\pi}\Delta T_1 + (1-\epsilon_1)\int_{-1}^0 \widetilde{g}^-_\omega(x=0,\mu) d\mu && (3.24)\\ \widetilde{g}^-_\omega(x=L) &= B_\omega = \epsilon_2 \frac{C_\omega}{4\pi}\Delta T_2 + (1-\epsilon_2)\int_0^1 \widetilde{g}^+_\omega(x=L,\mu) d\mu, && (3.25)\end{aligned}$$

where ϵ_1 and ϵ_2 are the emissivities of the hot and cold walls, respectively. When $\epsilon_1 = \epsilon_2 = 1$, the walls are black and we recover Dirichlet boundary conditions. Note that while we assume a thermal spectral distribution for the boundary condition, an arbitrary spectral profile can be specified by replacing the thermal distribution with the desired distribution. Equations (3.24) & (3.25) are specific for diffuse boundary scattering; the specular case is presented in Appendix A.

Applying the boundary conditions to Eqs. (5.6) & (5.7), we have

$$\begin{aligned}\widetilde{g}^+_\omega(x) &= A_{1\omega}\frac{C_\omega}{4\pi} e^{-\frac{\gamma_\omega}{\mu}x} + e^{-\frac{\gamma_\omega}{\mu}x}\int_0^L \Gamma(x')\left[D_\omega E_1(\gamma_\omega(L-x')) + B_{1\omega}E_1(\gamma_\omega x')\right] dx'\\ &+ \int_0^x \frac{\Gamma(x')}{\mu} e^{\frac{\gamma_\omega}{\mu}(x'-x)} dx' \; (\mu \in [0,1]) && (3.26)\\ \widetilde{g}^-_\omega(x) &= A_{2\omega}\frac{C_\omega}{4\pi} e^{-\frac{\gamma_\omega}{\mu}(L-x)} + e^{-\frac{\gamma_\omega}{\mu}(L-x)}\int_0^L \Gamma(x')\left[D_\omega E_1(\gamma_\omega x') + B_{2\omega}E_1(\gamma_\omega(L-x'))\right] dx'\\ &+ \int_x^L \frac{\Gamma(x')}{\mu} e^{-\frac{\gamma_\omega}{\mu}(x'-x)} dx' \; (\mu \in [0,1]), && (3.27)\end{aligned}$$

where

$$\begin{aligned}
A_{1\omega} &= \frac{\epsilon_1 \Delta T_1 + (1-\epsilon_1)\epsilon_2 \Delta T_2 E_2(\gamma_\omega L)}{1-(1-\epsilon_1)(1-\epsilon_2)(E_2(\gamma_\omega L))^2},\ A_{2\omega} = \frac{\epsilon_2 \Delta T_2 + (1-\epsilon_2)\epsilon_1 \Delta T_1 E_2(\gamma_\omega L)}{1-(1-\epsilon_1)(1-\epsilon_2)(E_2(\gamma_\omega L))^2},\\
B_{1\omega} &= \frac{1-\epsilon_1}{1-(1-\epsilon_1)(1-\epsilon_2)(E_2(\gamma_\omega L))^2},\ B_{2\omega} = \frac{1-\epsilon_2}{1-(1-\epsilon_1)(1-\epsilon_2)(E_2(\gamma_\omega L))^2},\\
D_\omega &= \frac{(1-\epsilon_1)(1-\epsilon_2)E_2(\gamma_\omega L)}{1-(1-\epsilon_1)(1-\epsilon_2)(E_2(\gamma_\omega L))^2},
\end{aligned}$$

and $E_n(x)$ is the exponential integral given by:(*21*)

$$E_n(x) = \int_0^1 \mu^{n-2} e^{-\frac{x}{\mu}} d\mu. \tag{3.28}$$

To close the problem, we plug Eqs. (3.26) & (3.27) into Eq. (5.4) and obtain an integral equation for temperature as:

$$\begin{aligned}
2\int_0^{\omega_m} \frac{C_\omega}{\tau_\omega} d\omega \Delta\widetilde{T}(\widehat{x}) &= \int_0^{\omega_m} \frac{C_\omega}{\tau_\omega} \left[A_{1\omega} E_2\left(\widehat{\gamma_\omega}\widehat{x}\right) + A_{2\omega} E_2(\widehat{\gamma_\omega}(1-\widehat{x}))\right] d\omega\\
&+ \int_0^1 \int_0^{\omega_m} \widetilde{Q}_\omega(x') \frac{G_\omega(\widehat{x},\widehat{x}')}{\mathrm{Kn}_\omega} d\omega d\widehat{x}'\\
&+ \int_0^1 \Delta\widetilde{T}(\widehat{x}') \int_0^{\omega_m} \frac{C_\omega G_\omega(\widehat{x},\widehat{x}')}{\mathrm{Kn}_\omega \tau_\omega} d\omega d\widehat{x}',
\end{aligned} \tag{3.29}$$

where $\widehat{x} = x/L$, $\mathrm{Kn}_\omega = \Lambda_\omega / L$ is the Knudsen number, $\widehat{\gamma_\omega} = \frac{1+i\eta\tau_\omega}{\mathrm{Kn}_\omega}$ and

$$\begin{aligned}
G_\omega(\widehat{x},\widehat{x}') &= E_2(\widehat{\gamma_\omega}\widehat{x}) \left[D_\omega E_1(\widehat{\gamma_\omega}(1-\widehat{x}')) + B_{1\omega} E_1(\widehat{\gamma_\omega}\widehat{x}')\right]\\
&+ E_2(\widehat{\gamma_\omega}(1-\widehat{x})) \left[D_\omega E_1(\widehat{\gamma_\omega}\widehat{x}') + B_{1\omega} E_1(\widehat{\gamma_\omega}(1-\widehat{x}'))\right]\\
&+ E_1(\widehat{\gamma_\omega}|\widehat{x}'-\widehat{x}|).
\end{aligned} \tag{3.30}$$

Equation (3.29) can be written in the form:

$$\Delta T(\widehat{x}) = f(\widehat{x}) + \int_0^1 K(\widehat{x},\widehat{x}') \Delta T(\widehat{x}') d\widehat{x}', \tag{3.31}$$

where the kernel function $K(\widehat{x},\widehat{x}')$ is given by

$$K(\widehat{x},\widehat{x}') = \frac{1}{2\int_0^{\omega_m} \frac{C_\omega}{\tau_\omega} d\omega} \int_0^{\omega_m} \frac{C_\omega G_\omega(\widehat{x},\widehat{x}')}{\mathrm{Kn}_\omega \tau_\omega} d\omega \tag{3.32}$$

and the inhomogeneous function $f(\widehat{x})$ is given by

$$\begin{aligned} f(\widehat{x}) &= \frac{1}{2\int_0^{\omega_m}\frac{C_\omega}{\tau_\omega}d\omega}\int_0^{\omega_m}\frac{C_\omega}{\tau_\omega}\left[A_{1\omega}E_2(\widehat{\gamma_\omega}\widehat{x}) + A_{2\omega}E_2(\widehat{\gamma_\omega}(1-\widehat{x}))\right]d\omega \\ &+ \frac{1}{2\int_0^{\omega_m}\frac{C_\omega}{\tau_\omega}d\omega}\int_0^1\int_0^{\omega_m}\widetilde{Q}_\omega(x')\frac{G_\omega(\widehat{x},\widehat{x}')}{\mathrm{Kn}_\omega}d\omega d\widehat{x}'. \end{aligned} \tag{3.33}$$

From Eq. (3.31), we see that the governing equation is a Fredholm integral equation of the second kind. Previously, the gray version of Eq. (3.29) that assumes average phonon properties has been solved numerically using integral discretization method.(*21*) While this approach does yield the solution, it requires the filling and inversion of a large, dense matrix, an expensive calculation even for the gray case. Considering the full phonon dispersion adds additional integrations to calculate each element of the matrix, dramatically increasing the computational cost. Additionally, care must be taken to account for a singularity point at $\widehat{x}' = \widehat{x}$ since $E_1(0) \to \infty$.

Here, we solve this equation using the method of degenerate kernels,(*116*) which is much more efficient than the integral discretization method and automatically accounts for the singularity point at $\widehat{x}' = \widehat{x}$. This method is based on expanding all the functions in Eq. (3.31) in a Fourier series, then solving for the coefficients of the temperature profile. From the temperature $\Delta\widetilde{T}(\widehat{x})$, all other quantities such as the distribution and heat flux can be obtained.

To apply this method, we first need to expand the inhomogeneous function $f(\widehat{x})$ and kernel $K(\widehat{x},\widehat{x}')$ with a Fourier series. This expansion is possible because both $f(\widehat{x})$ and $K(\widehat{x},\widehat{x}')$ are continuous and continuously differentiable on the relevant spatial domains of normalized length between [0, 1] and [0, 1] × [0, 1], respectively.(*116*) All the necessary functions can be expanded using a linear combination of sines and cosines; however, a substantial simplification can be obtained by solving a symmetric problem in which the spatial domain is extended to include its mirror image by extending both $f(\widehat{x})$ and $K(\widehat{x},\widehat{x}')$ to [-1,1] and [-1,1] × [-1,1]. Because of the symmetry of this domain, all the coefficients for sine functions equal zero and the Fourier series for both functions reduces to a cosine expansion. $f(\widehat{x})$ is then approximated as

$$f_{(N)}(\widehat{x}) = \frac{1}{2}f_0 + \sum_{m=1}^{N} f_m \cos(m\pi\widehat{x}), \tag{3.34}$$

where $f_m = 2\int_0^1 f(\widehat{x})\cos(m\pi\widehat{x})d\widehat{x}$. The kernel $K(\widehat{x},\widehat{x}')$ can be represented by a degenerate double Fourier series, given by

$$\begin{aligned} K_{(N)}(\widehat{x},\widehat{x}') = \frac{1}{4}k_{00} &+ \frac{1}{2}\sum_{m=1}^{N} k_{m0}\cos(m\pi\widehat{x}) + \frac{1}{2}\sum_{n=1}^{N} k_{0n}\cos(n\pi\widehat{x}') \\ &+ \sum_{m=1}^{N}\sum_{n=1}^{N} k_{mn}\cos(m\pi\widehat{x})\cos(n\pi\widehat{x}'), \end{aligned} \tag{3.35}$$

where

$$k_{mn} = 4\int_0^1\int_0^1 K(\widehat{x},\widehat{x}')\cos(m\pi\widehat{x})\cos(n\pi\widehat{x}')d\widehat{x}d\widehat{x}'. \tag{3.36}$$

Moreover, the convergence and completeness theorem of cosine functions guarantees that $K_{(N)}(\widehat{x},\widehat{x}')$ and $f_{(N)}(\widehat{x})$ converge to $K(\widehat{x},\widehat{x}')$ and $f(\widehat{x})$ as $N \to \infty$.(*117*)

Inserting Eqs. (3.34) & (3.35) into Eq. (3.31), we then obtain the following integral equation

$$\begin{aligned} \sum_{m=0}^{N} x_m\cos(m\pi\widehat{x}) \;=\; & \frac{1}{2}f_0 + \sum_{m=0}^{N} f_m\cos(m\pi\widehat{x}) + \int_0^1 \sum_{n=0}^{N} x_m\cos(n\pi\widehat{x}')\left[\frac{1}{4}k_{00}\right. \\ & +\frac{1}{2}\sum_{m=1}^{N} k_{m0}\cos(m\pi\widehat{x}) + \frac{1}{2}\sum_{n=1}^{N} k_{0n}\cos(n\pi\widehat{x}') \\ & \left.+\sum_{m=1}^{N}\sum_{n=1}^{N} k_{mn}\cos(m\pi\widehat{x})\cos(n\pi\widehat{x}')\right] d\widehat{x}', \end{aligned} \tag{3.37}$$

where x_m are the desired but unknown Fourier coefficients of $\Delta\widetilde{T}(\widehat{x})$.

Using the orthogonality of $\cos(n\pi\widehat{x})$ on [0, 1] gives a simpler form of Eq. (3.37):

$$\sum_{m=0}^{N} x_m\cos(m\pi\widehat{x}) = \frac{1}{2}f_0+\sum_{m=0}^{N} f_m\cos(m\pi\widehat{x})+\frac{1}{4}\sum_{m=0}^{N} k_{m0}x_m+\frac{1}{2}\sum_{m=1}^{N}\sum_{n=1}^{N} k_{mn}x_n\cos(m\pi\widehat{x}). \tag{3.38}$$

Grouping the terms with the same index m in cosine, a system of linear equations of x_m can be obtained as:

$$\bar{\bar{A}}\bar{x} = \bar{f}, \tag{3.39}$$

where $\bar{x}$ is the vector of unknown coefficient x_m and $\bar{f}$ is the vector of f_m in Eq. (3.34). The matrix $\bar{\bar{A}}$ contains elements $A_{00} = 1 - \frac{k_{00}}{4}$, $A_{0n} = -\frac{1}{2}k_{0n}$, $A_{n0} = -\frac{k_{n0}}{4}$, $A_{nn} = 1 - \frac{1}{2}k_{nn}$ and $A_{nm} = -\frac{1}{2}k_{nm}$ ($m \neq n \neq 0$). Expressions of the elements in $\bar{\bar{A}}$ can be obtained analytically for the specific kernel here and are given in Appendix B for the steady-state heat conduction with diffuse walls. Since there is no row or column in $\bar{\bar{A}}$ that is all zeros or a constant multiple of another row or column, it is always guaranteed that $\bar{\bar{A}}$ is non-singular and its inverse exists.

Solving the matrix system yields x_m and thus the temperature $\Delta\widetilde{T}(\widehat{x})$, $\widetilde{g_\omega^+}(x)$, and $\widetilde{g_\omega^-}(x)$ can be obtained from $\Delta\widetilde{T}(\widehat{x})$ using Eqs. (3.26) & (3.27). Finally, the spectral heat is given by:

$$q_\omega(x) = \int_{-1}^{1} g_\omega v_\omega \mu d\mu = \int_{0}^{1} g_\omega^+ v_\omega \mu d\mu - \int_{0}^{1} g_\omega^- v_\omega \mu d\mu, \tag{3.40}$$

thereby closing the problem.

Summary of the method

We now summarize the key steps to implement our method. The first step is to determine the appropriate boundary conditions for the problem and compute the constants in Eqs. (3.26) & (3.27). Subsequently, the kernel function $K(\widehat{x}, \widehat{x'})$ and the inhomogenous function $f(\widehat{x})$ can be obtained from Eq. (3.20), and their Fourier coefficients can be computed using Eqs. (3.34) & (3.35). The elements in $\bar{\bar{A}}$ correspond to the Fourier coefficients of kernel function $K(\widehat{x}, \widehat{x'})$, and $\bar{f}$ is a vector of the Fourier coefficients of the inhomogeneous part of Eq. (3.29). We emphasize that analytic expressions for all of these elements exist and can be obtained; examples of these coefficients for steady heat conduction with non-black, diffuse boundaries are given in Appendix B. Once $\bar{\bar{A}}$ and $\bar{f}$ are obtained, Eq. (3.39) is solved by standard matrix methods to yield the coefficients x_m. Finally, $\Delta\widetilde{T}(\widehat{x})$ is given by $\sum_{m=0}^{N} x_m \cos(m\pi\widehat{x})$.

Efficiency of the method

The primary benefit of our method is the substantial reduction in computational cost compared to the widely used integral discretization approach. Since both $K_{(N)}(\widehat{x}, \widehat{x}')$ and $f_{(N)}(\widehat{x})$ converge to $K(\widehat{x}, \widehat{x}')$ and $f(\widehat{x})$ as $1/N^2$, only a few terms of expansion are required for accurate calculations. In practice, we find that only 20 terms are necessary before the calculation converges, meaning the required matrix is only 20×20. Compared to the traditional integral discretization method that requires a matrix on the order of 1000×1000 before convergence is achieved, our approach is at least 3 orders of magnitude faster. Further, as we will show in Section 3.3, our semi-analytical approach enables a closed-form solution for the cross-plane thermal conductivity of a thin film that is not possible to derive from the integral discretization method.

Demonstration of the method

As an example calculation, we consider steady-state heat conduction between two walls that are either black or non-black. In the former case, both wall emissivities ϵ_1 and ϵ_2 equal 1 while in the latter case they are set to 0.5. Assuming steady state and no heat generation inside the domain, $\eta = 0$, and $Q_\omega = 0$. The Fourier coefficients of $K(\widehat{x}, \widehat{x}')$ and $\bar{f}$ for these two specific cases are given in Appendix B. We perform our calculations for crystalline silicon, using the experimental dispersion in the [100] direction and assuming the crystals are isotropic. The numerical details concerning the dispersion and relaxation times are given in Ref. (*79*).

We calculate the deviational temperature distribution $\Delta T(\widehat{x})$ for different film thickness at different equilibrium temperatures as shown in Figs. 3.6 & 3.7 while keep-

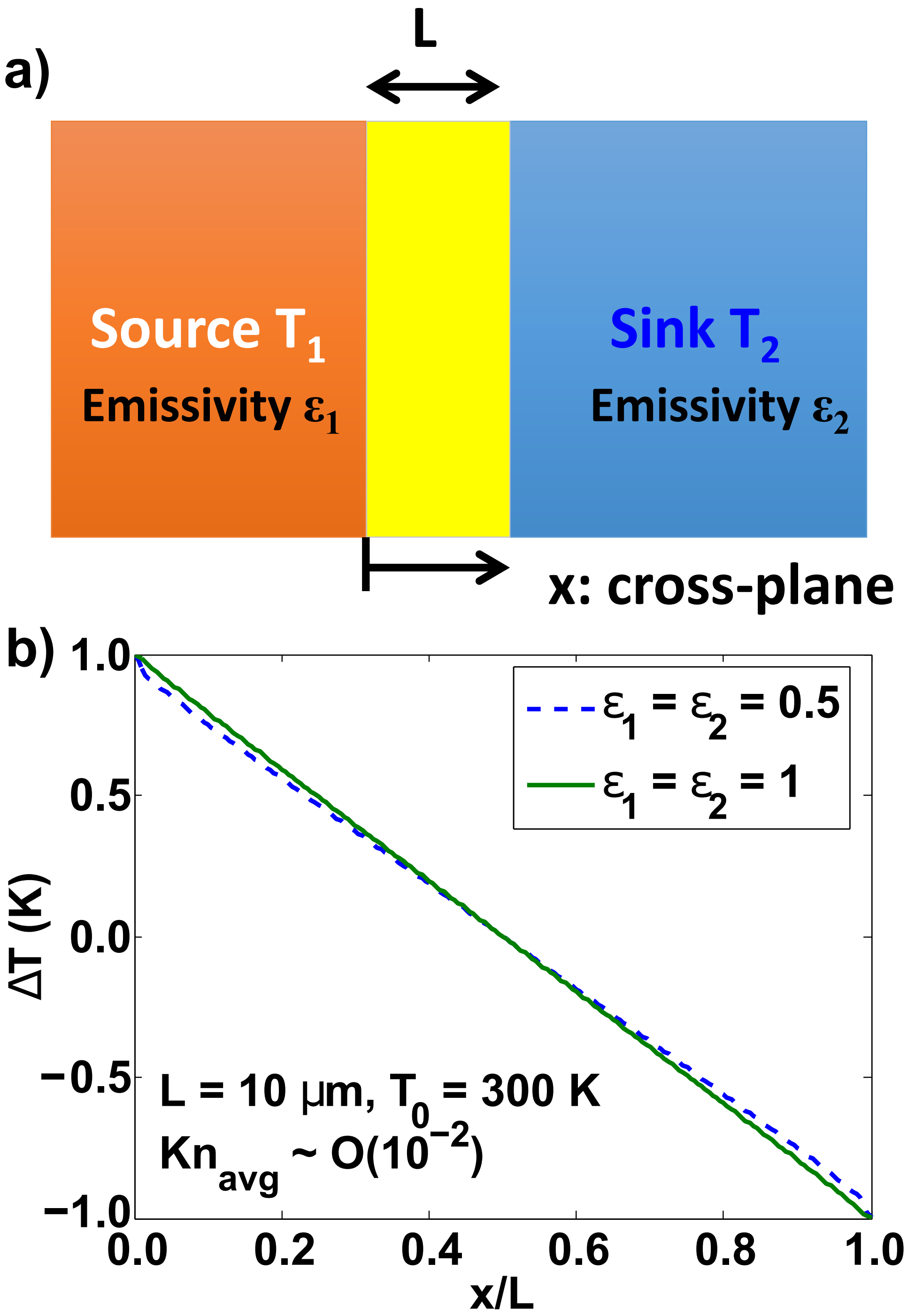

Figure 3.6: (a) Schematic of a planar slab with walls at different temperatures. (b)Temperature distribution $\Delta T(\widehat{x})$ for a planar slab with black walls (solid lines) and nonblack walls (dashed lines) when $\mathrm{Kn}_{avg} \sim O(10^{-2})$.

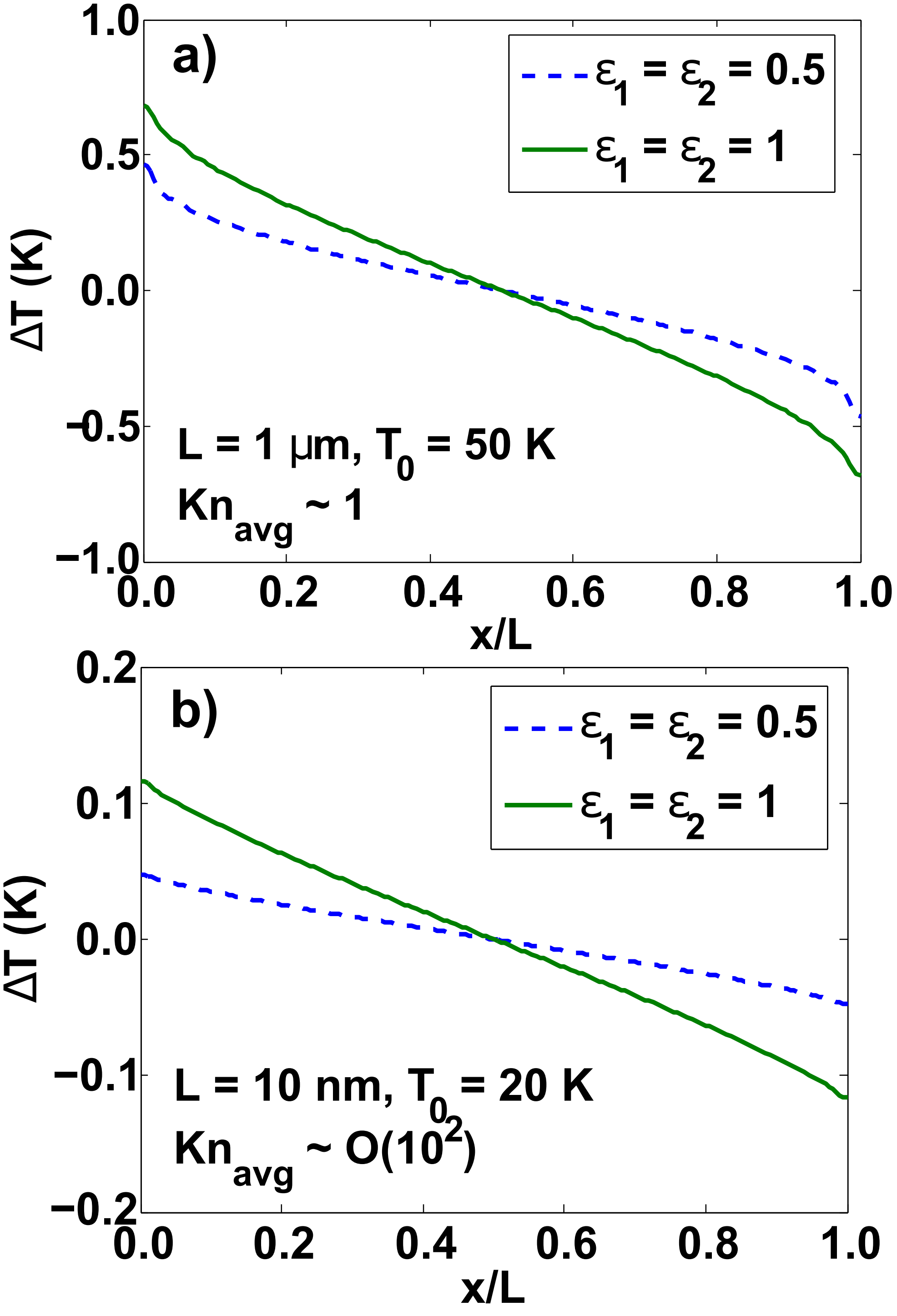

Figure 3.7: Temperature distribution $\Delta T(\widehat{x})$ for a planar slab with black walls (solid lines) and nonblack walls (dashed lines) when (a) $\mathrm{Kn}_{\mathrm{avg}} \sim 1$, and (b) $\mathrm{Kn}_{\mathrm{avg}} \sim O(10^2)$. As $\mathrm{Kn}_{\mathrm{avg}}$ increases, temperature slip at the boundaries grows larger.

ing $|\Delta T1| = |\Delta T_2| = 1$ K. When the averaged Knudsen number is small such that $\mathrm{Kn}_{avg} \ll 1$, the temperature profile remains linear. As thin film thickness decreases such that $\mathrm{Kn}_{avg} \sim 1$ or $\gg 1$, we observe a similar temperature slip as discussed in Ref. (*21*). These calculations take approximately one second to compute on a standard laptop computer. In contrast, the integral discretization method is at least 1000 times slower, requiring on the order of one hour to arrive at the same result.

In addition to the finite-layer geometry we consider above, the series expansion approach can be readily applied to many other thin film geometries, such as superlattices and the transducer film used in thermoreflectance experiments, by imposing different boundary conditions. Similar large reductions in computational cost can be expected for these cases.

Analytical formula for cross-plane thermal conductivity

Our semi-analytical approach also allows us to obtain a simple closed form expression for the cross-plane thermal conductivity as a function of film thickness, analogous to the Fuchs-Sondheimer expression for in-plane thermal conductivity. Such a formula allows the cross-plane thermal conductivity to be easily evaluated because the full solution of the BTE is no longer required. To derive this formula, we assume black walls and calculate the spatially averaged spectral heat flux that is integrated over the domain, defined as:

$$\begin{aligned}\int_0^1 q_\omega(\widehat{x})d\widehat{x} = \frac{1}{L}\int_0^L q_\omega(x)dx = \left(\frac{\Delta T_1 - \Delta T_2}{2}\right)\left[\frac{1}{3}C_\omega v_\omega \mathrm{Kn}_\omega - C_\omega v_\omega \mathrm{Kn}_\omega E_4\left(\frac{1}{\mathrm{Kn}_\omega}\right)\right] \\ + \frac{C_\omega v_\omega}{2\mathrm{Kn}_\omega}\left[\int_0^1\int_0^{\widehat{x}} \Delta T(\widehat{x}')E_2\left(\frac{|\widehat{x}' - \widehat{x}|}{\mathrm{Kn}_\omega}\right)d\widehat{x}'d\widehat{x} - \int_0^1\int_{\widehat{x}}^1 \Delta T(\widehat{x}')E_2\left(\frac{|\widehat{x}' - \widehat{x}|}{\mathrm{Kn}_\omega}\right)d\widehat{x}'d\widehat{x}\right]\end{aligned} \tag{3.41}$$

Once x_m is solved from Eq. (3.37), we can insert the Fourier series of $\Delta T(x)$ into Eq. (3.41), which leads to

$$\begin{aligned}\int_0^1 q_\omega(\widehat{x})d\widehat{x} &= \left[\left(\frac{\Delta T_1 - \Delta T_2}{2}\right)\frac{1}{3}C_\omega v_\omega \mathrm{Kn}_\omega - C_\omega v_\omega \mathrm{Kn}_\omega E_4\left(\frac{1}{\mathrm{Kn}_\omega}\right)\right] \\ &+ \frac{C_\omega v_\omega}{2\mathrm{Kn}_\omega}\sum_{m=1}^{\infty} x_m[1-(-1)^m]\int_0^1 \frac{(\mathrm{Kn}_\omega \mu)^2\left(1+e^{-\frac{1}{\mathrm{Kn}_\omega \mu}}\right)}{1+(\mathrm{Kn}_\omega \mu)^2(m\pi)^2}d\mu. \end{aligned} \tag{3.42}$$

According to Fourier's law, the integrated heat flux is given by

$$\int_0^1 q_\omega^f(\widehat{x})d\widehat{x} = \frac{1}{3}C_\omega v_\omega \mathrm{Kn}_\omega(\Delta T_1 - \Delta T_2). \tag{3.43}$$

The heat suppression function is defined as the ratio of the BTE and Fourier's heat flux(*118*), given as

$$S(\mathrm{Kn}_\omega, L) = \frac{1}{2} - \frac{3}{2}E_4\left(\frac{1}{\mathrm{Kn}_\omega}\right) + \frac{3}{2}\sum_{m=1}^{\infty} x_m[1-(-1)^m]\int_0^1 \frac{\mu^2\left(1+e^{-\frac{1}{\mathrm{Kn}_\omega \mu}}\right)}{1+(\mathrm{Kn}_\omega \mu)^2(m\pi)^2}d\mu. \tag{3.44}$$

Note that the suppression function in general not only depends on Kn_ω but also is a function of geometry through x_m. The reduced or apparent thermal conductivity at a given domain thickness L is then given by:

$$k(L) = \int_0^{\omega_m} \frac{1}{3}C_\omega v_\omega \Lambda_\omega S(\mathrm{Kn}_\omega, L)d\omega. \tag{3.45}$$

This formula is analogous to the Fuch-Sondheimer equation for transport along thin films and allows the evaluation of the cross-plane thermal conductivity provided the expansion coefficients x_m are known. However, obtaining the expansion coefficients still requires solving the BTE as described above. A more useful result would be a suppression function that depends only on the Knudsen number as is available for in-plane heat conduction with the Fuchs-Sondheimer formula.(*104*, *105*)

To overcome this difficulty, we derive a simplified form of Eq. (3.44) that is valid under the conditions of most experiments. Note from Fig. 3.6(b) that for $\mathrm{Kn}_{avg} \sim$

$O(10^{-2})$, the temperature distribution is still linear, allowing us to simplify Eq. (3.44) by inserting the linear temperature distribution. Doing so leads to a simplified suppression function:

$$S_{\text{simplified}}(\text{Kn}_\omega) = 1 + 3\text{Kn}_\omega \left[E_5 \left(\frac{1}{\text{Kn}_\omega} \right) - \frac{1}{4} \right]. \tag{3.46}$$

This equation depends only on the Knudsen number and hence can be used to directly evaluate the cross-plane thermal conductivity given the phonon dispersion. This equation is valid provided that the ballistic modes are only low frequency phonons that contribute little to heat capacity, a situation that occurs often in experiment because high frequency phonons have short MFPs, on the order of tens of nanometers, at temperatures exceeding 20 K.

One important observation from Fig. 3.8(a) is that the exact and simplified suppression functions converge to the same curve at large Kn_ω. Also note that as the slab thickness decreases, the Knudsen number of a phonon with a particular MFP becomes larger. Therefore, in the limit of very small distance between the boundaries, the only important portion of the suppression function is at large values of Knudsen number exceeding $\text{Kn}_\omega = 1$ because phonons possess a finite minimum MFP. This observation suggests that for practical purposes the simplified suppression can be used even outside the range in which it is strictly valid with good accuracy. This simplification is very desirable because the simplified suppression function only depends on the Knudsen number and thus can be applied without any knowledge of other material properties.

Next, we apply this simplified suppression function to extract information about the phonon MPFs from the experimental measurements. In several works, thermal conductivity over variable lengths of nanostructures such as nanotubes, graphene ribbons and SiGe nanowires was measured. In principle, the measurements should contain information about MFPs: if phonons have MFPs exceeding the distance

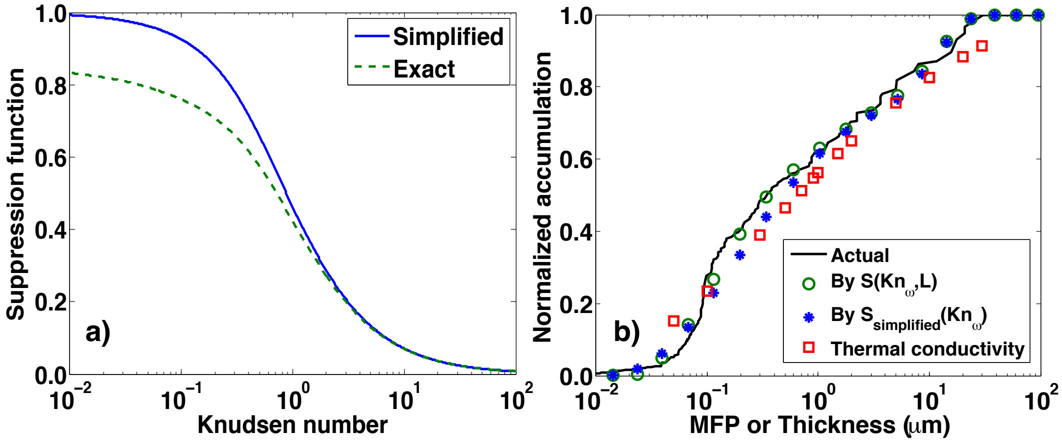

Figure 3.8: (a) Simplified (solid line) and exact (dashed line) suppression function versus Knudsen number. The exact and simplified suppression functions converge to the same curve at large Kn$_{\omega}$. (b) Example MFP reconstructions for silicon at 300 K using numerically simulated data. Plotted are the analytical MFP distribution (solid line), the numerical apparent thermal conductivities (squares), and the reconstructed MFP distribution by the exact suppression function (circles) and by the simplified suppression function (stars). The x axis corresponds to the MFP for the distributions and to the slab thickness for the thermal conductivity data. Both the exact and simplified suppression functions yield satisfactory MFP reconstruction results.

between the heat source and the heat sink, their contribution to thermal conductivity is reduced compared to that in the bulk material, and thus the deviations of the measured thermal conductivity from the bulk value provide information on the phonon MFPs. Prior studies extracted only an average MFP despite the fact that recent works have demonstrated that in many solids phonon MFPs vary over orders of magnitude, make the approximation of an average MFP for all phonons quite poor.

The method proposed by Minnich is able to extract spectral MFP spectra from variable-length thermal conductivity measurements by solving Eq. 3.45 as an inverse problem. The detailed description of the method is given in Ref. (*118*). Briefly, the variable-length thermal conductivities can be related to the MFP distribution $f(\Lambda_\omega)$ by

$$k_i = \int_0^\infty S(\mathrm{Kn}_\omega) f(\Lambda_\omega) d\Lambda_\omega, \tag{3.47}$$

where $S(\mathrm{Kn}_\omega)$ is the suppression function given by Eq. 3.44 or Eq. 3.46. If k_i's are known, $f(\Lambda_\omega)$ can be reconstructed using convex optimization.

To investigate the accuracy of Eq. 3.46, we perform the above reconstruction procedure to recover the MFP spectrum from thermal conductivity data as a function of slab thickness using both exact and simplified suppression functions. We synthesize effective thermal conductivities numerically using Eq. (3.45). Using these effective thermal conductivities and our knowledge of the suppression function, we use convex optimization to solve for the MFP spectrum. In the exact suppression function case, each slab thickness has its own suppression function given by Eq. (3.44) while in the simplified case Eq. (3.46) is used for all slab thicknesses.

As shown in Fig. 3.8(b), both the simplified and exact suppression functions yield satisfactory results. Even though the smallest thickness we consider here is 50 nm, close to the ballistic regime, the simplified suppression function still gives a decent prediction over the whole MFP spectrum, with a maximum of 15 % deviation from the actual MFP spectrum. For practical purposes, this deviation is comparable to uncertainties in experimental measurements and therefore the simplified suppression function can be used as an excellent approximation in the reconstruction procedure. This result demonstrates that length-dependent thermal conductivity measurements like those recently reported for SiGe nanowires(*119*) and graphene ribbons(*120*) can be used to reconstruct the full MFP spectrum rather than only an average MFP. We perform an investigation of our approach for this purpose in

Ref. (*121*).

3.4 Summary

In an infinite or semi-infinite domain, we have derived a new analytical Green's function of the multi-dimensional frequency-dependent BTE and demonstrated its capability to efficiently solve a wide range of problems that were previously intractable except using expensive numerical approaches. On the other hand, when the interested domain becomes finite, we have presented a series expansion method to solve the one-dimensional, transient frequency-dependent BTE and demonstrated its capability to describe cross-plane heat conduction in thin films. Our solution is valid from the diffusive to ballistic regimes, rigorously includes frequency dependence, and can be applied to a wide range of geometries.

With the time resolution on the order of tens of femtosecond from commercially available femtosecond laser sources and the spatial resolution on the order of tens of nanometers from nanoscale metallic heating structures, it becomes possible to directly access energy transport processes among phonons using ultrafast optical techniques. While ultrafast methods have shown their potential to probe the fundamental energy carriers, analysis of nanoscale energy transport occurring in those techniques remains challenging. With the BTE solutions we derived above, we are now able to accurately describe energy transport in some ultrafast optical experiments. In the next two chapter, we demonstrate how we are able to rigorously investigate the microscopic properties of thermal phonons using the unique combination of the ultrafast methods and BTE modeling.

Chapter 4

TRANSPORT REGIMES BEYOND DIFFUSION AND THEIR APPLICATIONS

Chapter 4 has been adapted from

(*1*) Chengyun Hua and Austin J. Minnich. "Transport regimes in quasiballistic heat conduction". In: *Phys. Rev. B* 89 (9 2014), p. 094302. DOI: `10.1103/PhysRevB.89.094302`. URL: `http://link.aps.org/doi/10.1103/PhysRevB.89.094302`.

4.1 Introduction

One advantage of analytical solutions to the phonon Boltzmann transport equation (BTE) is that just by looking at the form of the solution we could fully investigate heat conduction from diffusive to ballistic regimes as well as the transition regime, called quasiballistic transport.

Quasiballistic heat conduction occurs if a temperature gradient exists over length scales comparable to phonon mean free paths (MFPs).(*21*, *22*) In this regime, local thermal equilibrium does not exist and Fourier's law is no longer valid. Presently, quasiballistic transport is under investigation due to its potential to infer information about the MFPs of thermal phonons,(*118*) knowledge of which is crucial to engineer thermal conductivity but remains unknown for most solids.(*13*, *14*)

Quasiballistic transport was originally observed in macroscopic samples using heat pulse experiments(*18*) and later in silicon membranes using a microfabricated platform.(*122*) Nonlocal theories of heat conduction based on the BTE were introduced to describe the quasiballistic regime for phonons(*68*, *123*, *124*) and electrons.(*125*) Koh and Cahill reported modulation-frequency dependent thermal conductivities in a time-domain transient thermoreflectance (TDTR) experiment that they attributed to quasiballistic transport and suggested that the meansurements could be used to measure MFPs. Recently, quasiballistic transport has been observed in other experimental configurations.(*20*, *23–25*) Minnich introduced a reconstruction technique that described how to quantitatively recover the MFP spectra from observations of quasiballistic heat transfer.(*118*)

One notable experimental method for observing quasiballistic transport is the transient thermal grating (TTG) technique(*25*, *126*, *127*), in which the interference of two laser pulses creates a sinusoidal initial temperature profile with wavelength λ. The observed thermal decay yields information about the thermal properties of the material. Recent work has demonstrated that these measurements can also reveal MFPs if the grating wavelength is comparable to MFPs, but interpreting measurements using the reconstruction method introduced by Minnich requires a solution of the BTE. A previous work reported a modified "two-channel" model(*126*), in which low and high frequency phonons are described by the BTE and heat equation, respectively, but the extent of the validity of this model is unclear. An analysis within the framework of the BTE(*128*) has been recently reported but the analysis of the frequency-dependent BTE was solely numerical, complicating its use for the reconstruction method.

Here, we analyze thermal transport in TTG using the Green's function solution to the frequency-dependent BTE derived in Chapter 3. Our analysis demonstrates the existence of weakly and strongly quasiballistic transport regimes that are distinguished by the thermal decay time relative to the phonon relaxation times. We provide theoretical justification for the use of a modified diffusion theory to interpret observations of quasiballistic transport. Finally, we use our solution to derive a corrected suppression function that enables phonon MFP spectra to be measured more accurately. Our results will lead to a better understanding of phonon heat conduction in solids like thermoelectrics.

4.2 Modeling

We start with Eq. 3.1. Thermal transport in a TTG experiment, assuming only in-plane heat conduction and a small temperature rise, $\Delta T = T(x,t) - T_0$, relative to a reference temperature T_0, is described by the 1D frequency-dependent BTE,(*22*)

$$\frac{\partial g_\omega}{\partial t} + v_g \mu \frac{\partial g_\omega}{\partial x} = -\frac{g_\omega}{\tau_\omega} + \frac{1}{4\pi}\frac{C_\omega}{\tau_\omega}\Delta T + \frac{Q_\omega}{4\pi} \tag{4.1}$$

where $g_\omega = f_\omega(x,t,\mu) - f_0(T_0)$ is the deviational distribution function, $f_0 = f_0(x,t)$ is the equilibrium distribution function, $\mu = cos(\theta)$ is the directional cosine, v_ω is the phonon group velocity, τ_ω is the phonon relaxation time, and Q_ω is the spectral volumetric heat generation.

As treated in Chapter 3, to close the problem, energy conservation is used to relate g_ω to ΔT, given by

$$\int\int_0^{\omega_m}\left[\frac{g_\omega(x,t)}{\tau_\omega} - \frac{1}{4\pi}\frac{C_\omega}{\tau_\omega}\Delta T(x,t)\right] d\omega d\Omega = 0, \tag{4.2}$$

where $g_\omega = \hbar\omega D(\omega)(f_\omega(x,t,\theta) - f_0(T_0))$ is the desired deviational distribution function, $Q_\omega(x,t)$ is the spectral volumetric heat generation, $v_g(\omega,T)$ is the phonon group velocity, and $\tau(\omega,T)$ is the phonon relaxation time. Here, x is the spatial variable, t is the time, ω is the phonon frequency, T is the temperature, and $\mu = cos(\theta)$ is the directional cosine of the polar angle θ. $\hbar$ is the reduced Planck constant, $D(\omega)$ is the phonon density of states, f_{BE} is the Bose-Einstein distribution, and $C_\omega = \hbar\omega D(\omega)\frac{\partial f_{BE}}{\partial T}$ is the mode specific heat. The volumetric heat capacity is then given by $C = \int_0^{\omega_m} C_\omega d\omega$ and the thermal conductivity $k = \int_0^{\omega_m} k_\omega d\omega$, where $k_\omega = \frac{1}{3}C_\omega v_\omega \Lambda_\omega$ and $\Lambda_\omega = \tau_\omega v_\omega$ is the phonon MFP.

Since the initial temperature profile in TTG is sinusoidal, we can assume that both g_ω and ΔT are of the form e^{iqx}, where $q = 2\pi/\lambda$ is the grating wavevector, and the volumetric heat generation term in Eq. 4.1 has the following form:

$$Q_\omega = C_\omega e^{iqx}\delta(t), \tag{4.3}$$

where $\delta(t)$ denotes an impulse at $t = 0$, and the initial heat generation follows a thermal distribution. Substituting $g_\omega = \widetilde{g}_\omega(t,\mu)e^{iqx}$ and $\Delta T = \Delta\widetilde{T}(t)e^{iqx}$ into Eq. (4.1) leads to a first-order ODE for $\widetilde{g}_\omega(t)$. Collins *et. al.*(*128*) obtained an analytical solution by applying a Fourier transform to the grey form of this equation. Here, we extend the Fourier transform method to the frequency-dependent BTE.

Applying the Green's function method described in Section 3.2, we are able to decouple the nonlocal effects and directly obtain the following closed-form expression for the unknown distribution function $\widetilde{g}_\omega$ and transient temperature $\Delta\widetilde{T}$:

$$\mathcal{F}[\widetilde{g}_\omega](\eta) = \frac{1}{4\pi}\frac{C_\omega}{\tau_\omega}\frac{\mathcal{F}[\Delta\widetilde{T}](\eta)}{\gamma - i\eta} + \frac{C_\omega}{4\pi\tau_\omega}\frac{\Delta\widetilde{T}(0)}{\gamma - i\eta} \tag{4.4}$$

$$\mathcal{F}[\Delta\widetilde{T}](\eta) = \frac{\Delta\widetilde{T}(0)\int_0^{\omega_m}\frac{C_\omega}{\tau_\omega}\mathcal{A}(\eta)d\omega}{\int_0^{\omega_m}\frac{C_\omega}{\tau_\omega}[1-\mathcal{A}(\eta)]d\omega} \tag{4.5}$$

$$\mathcal{A}(\eta) = \frac{i}{2q\Lambda_\omega}\log\left(\frac{\tau_\omega\eta + q\Lambda_\omega + i}{\tau_\omega\eta - q\Lambda_\omega + i}\right), \tag{4.6}$$

where $\mathcal{F}$ denotes Fourier transform, $\gamma = (1 + iq\mu\Lambda_\omega)/\tau_\omega$, and η is the temporal Fourier variable. The time-domain solution is obtained by inverse fast Fourier transform. Therefore, we have derived an analytical solution to the frequency-dependent BTE that is valid from the ballistic to the diffusive regimes, enabling a more rigorous understanding of thermal transport in TTG.

We can gain insight into which parameters determine the transport regime from our solution. From Eq. (4.6), we identify two nondimensional parameters. One is the familiar phonon Knudsen number $\mathrm{Kn}_\omega = q\Lambda_\omega$, which compares the phonon MFP with a characteristic length, in this case $1/q$. To identify the second parameter, we notice that η^{-1} describes a time scale that we assign to be the characteristic thermal decay time Γ. We can therefore define a new non-dimensional parameter that we denote the transient number, given by $H_\omega = \tau_\omega/\Gamma$, which compares the phonon relaxation times with the thermal decay time Γ.

Note that the two parameters are not completely independent. For example, as the grating wavelength decreases, the thermal decay time also decreases. In the diffusion regime the relationship is trivial but in the quasiballistic and ballistic regimes the relationship becomes much more complex. While the Knudsen number can in principle completely distinguish the transport regime, we find that the transient number is an additional convenient parameter by which to specify the regime, particularly for quasiballistic transport where the specific Knudsen number at which a transition occurs is not obvious.

Therefore, together, these two numbers completely specify the transport regime. In the diffusive limit, length and time scales are much larger than the phonon MFPs and relaxation times, respectively, corresponding to $\mathrm{Kn}_\omega \ll 1$ and $H_\omega \ll 1$. In the ballistic regime, lengths and times are much smaller than MFPs and relaxation times, or $\mathrm{Kn}_\omega \gg 1$ and $H_\omega \gg 1$. The two regimes are well-understood limits of the BTE(*21*). Here, we focus on the intermediate range of the two limits, the quasiballistic regime.

4.3 Heat transport regimes

To begin, we examine the transient temperature decay in the different regimes as shown in Fig. 4.1. We perform our calculations for crystalline silicon, using the experimental dispersion in the [100] direction and assuming the crystals are isotropic. The numerical details concerning the dispersion and relaxation times are given by Minnich's recent work(*79*).

Diffusive and ballistic limits

We first confirm that our result correctly reproduces the diffusive and ballistic limits. Examining the limit of Eq. (4.5) when both phonon relaxation times and MFPs are much smaller than their corresponding characteristic scales ($H_\omega \ll 1$ & $\mathrm{Kn}_\omega^2 \ll 1$), we find that the solution reduces to the Fourier solution and the thermal decay

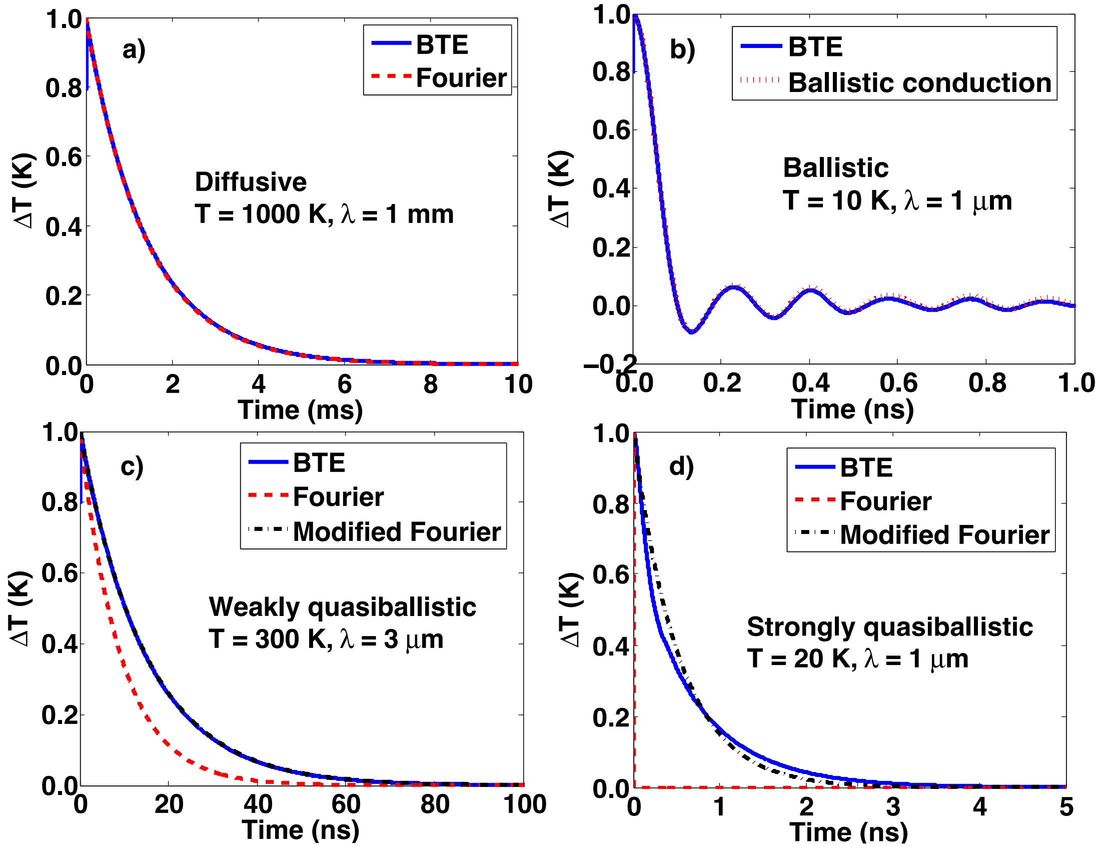

Figure 4.1: Temperature decay curves $\Delta\widetilde{T}$ in the (a) diffusive limit, (b) ballistic limit, (c) weakly quasiballistic regime, and (d) strongly quasiballistic regime. The BTE solutions are given by the solid lines, the Fourier solution by the dashed lines, the ballistic conduction solution by the dotted line, and the Modified Fourier solution by the dash-dotted lines.

time $\Gamma = (q^2\alpha)^{-1}$, where $\alpha = k/C$ is the Fourier thermal diffusivity. Fig. 4.1(a) demonstrates that the BTE solution agrees with the Fourier solution in this limit. Similarly, at the ballistic limit ($H_\omega \gg 1$ & $\mathrm{Kn}_\omega^2 \gg 1$) shown in Fig. 4.1b, the transient temperature given by Eq. (4.5) agrees with the ballistic solution of the BTE in which the relaxation times go to infinity.

Weakly quasiballistic regime

We now examine the intermediate quasiballistic regime by allowing the MFPs to be comparable to or greater than the grating wavevector while requiring the thermal decay time to be much longer than relaxation times, $\mathrm{Kn}_\omega^2 \sim 1$ but $H_\omega \ll 1$. We observe that the BTE solution does not agree with the Fourier's law solution, as shown in Fig. 4.1(c). However, we observe that the shape of the temperature decay remains exponential, as in Fourier's law, but with a smaller thermal conductivity. We denote this regime the weakly quasiballistic regime, and the Fourier solution with a modified thermal conductivity as the modified Fourier solution. So far, the validity of the modified Fourier model to describe quasiballistic thermal transport is largely based on experimental observations.(*25*) The only theoretical approach to explain this observation was developed by Maznev *et. al.*(*126*) Their modified "two-channel" model assumes that the low-frequency phonons, which are analyzed by the BTE, only interact with the thermal reservoir of high-frequency phonons, which are analyzed by the diffusion equation. However, the extent of the validity of this assumption is not clear.

Here, we give a more rigorous explanation using our solution. Under the assumption of $\mathrm{Kn}_\omega^2 \sim 1$ and $H_\omega \ll 1$, the Taylor expansion of Eq. 4.6 around $H_\omega = 0$ gives

$$\mathcal{A}(\eta) = i\eta_\omega\eta + \frac{\tan^{-1}(\mathrm{Kn}_\omega)}{\mathrm{Kn}_\omega} \sim 1. \tag{4.7}$$

We observe that in the denominator of Eq. (4.5), $1 - \mathcal{A}(\eta) \sim \tau_\omega$ and the full asymptotic expression of $\mathcal{A}(\eta)$ should be used while in the numerator, $\mathcal{A}(\eta)$ can be approximated 1. Therefore, Eq. (4.5) asymptotically approaches the following form:

$$\mathcal{F}[\Delta\widetilde{T}](\eta) \approx \frac{\Delta\widetilde{T}(0)}{q^2\alpha_{mod} - i\eta} \tag{4.8}$$

$$k_{mod} = \int_0^{\omega_m} k_\omega \left\{ \frac{3}{(\mathrm{Kn}_\omega)^2} \left[1 - \frac{\tan^{-1}(\mathrm{Kn}_\omega)}{\mathrm{Kn}_\omega} \right] \right\} d\omega, \tag{4.9}$$

where $\alpha_{mod} = k_{mod}/C$ is the apparent thermal diffusivity and k_{mod} is the modified thermal conductivity. Recognizing that Eq. (4.8) is simply the Fourier transform of an exponential decay, we find $\Delta\widetilde{T}(t) \approx \Delta\widetilde{T}(0)\exp\left(-q^2\alpha_{mod}t\right)$. Thus, the formal solution of the BTE is equivalent to a modified diffusion theory with a modified thermal conductivity given by Eq. (4.8). The thermal decay time $\Gamma = (q^2\alpha_{mod})^{-1}$. We term this simplified solution the weak solution to the BTE, valid in the weakly quasiballistic regime. The modified thermal conductivity is the same expression given by Maznev *et. al.*(*126*)

Most recent experimental observations of quasiballistic transport have occurred in this weakly quasiballistic regime. For instance, in the TTG measurement of silicon membranes reported by Johnson *et al.*,(*25*) the typical $\mathrm{Kn}_\omega \approx 2.5$ and $H_\omega \sim O(0.01)$, based on the median thermal phonon MFP at the room temperature. Therefore, their measurements fall into the weakly quasiballistic regime and a modified Fourier solution should explain the results, in agreement with the experiment.

Strongly quasiballistic regime

As the grating wavelength decreases, eventually the thermal decay becomes so fast that it is comparable to or greater than relaxation times such that $H_\omega \sim 1$ and $\mathrm{Kn}_\omega^2 \sim 1$. Here, the assumption made in the modified "two-channel" model is not valid because some phonons in the thermal reservoir are now ballistic. For silicon, this regime occurs at small grating wavelength ($\lesssim 0.5\ \mu m$) or at cryogenic temperatures. In this case, the BTE solution deviates from the exponential decay and can no longer be explained with any type of diffusion model as shown in Fig. 4.1d, and a full solution given by Eq. (4.5) is necessary. We denote this regime the strongly quasiballistic regime. The equivalent decay time Γ is given by $\int_0^\infty \Delta T(t)dt/\Delta T(0)$, which reduces to the corresponding thermal decay times in the other two regimes above.

4.4 Suppression function

We now seek to understand how the thermal length and time scales affect which phonons conduct heat in each regime. From our model, we can calculate the spectral thermal conductance, defined as the ratio of heat flux to the temperature difference

$$\sigma_\omega = \frac{\int\int q_\omega(x,t)dxdt}{\int\int \Delta T(x,t)dxdt} = \frac{\int\int \widetilde{q}(\eta)e^{iqx}dxd\eta}{\int\int \Delta\widetilde{T}(\eta)e^{iqx}dxd\eta}, \tag{4.10}$$

where $q_\omega(x,t) = \int g_\omega(x,t,\theta)v_\omega\cos(\theta)d\Omega$ is the spectral heat flux. In this way, we remove any spatial and temporal factors and can directly compare the heat flow induced by a unit temperature difference for each phonon mode.

Substituting Eqs. (4.4) & (4.5) into Eq. (4.10), we derive a general expression for the spectral thermal conductance

$$\sigma_\omega = \sigma_f\left\{\frac{3}{(\mathrm{Kn}_\omega)^2}\left[1-\frac{\tan^{-1}(\mathrm{Kn}_\omega)}{\mathrm{Kn}_\omega}\right][H_\omega+1]\right\}, \tag{4.11}$$

where $\sigma_f = k_\omega/(\lambda/2)$ is the Fourier thermal conductance. The term in the brackets, equal to the ratio of the BTE thermal conductance to the Fourier thermal conductance, was previously termed the suppression function $S(\mathrm{Kn}_\omega, H_\omega)$ by Minnich(*118*).

Now let us examine the thermal conductance in the two quasiballistic transport regimes discussed above, shown in Fig. 4.2. We compare the thermal conductance calculated by the Fourier's law, weak BTE and full BTE solutions.

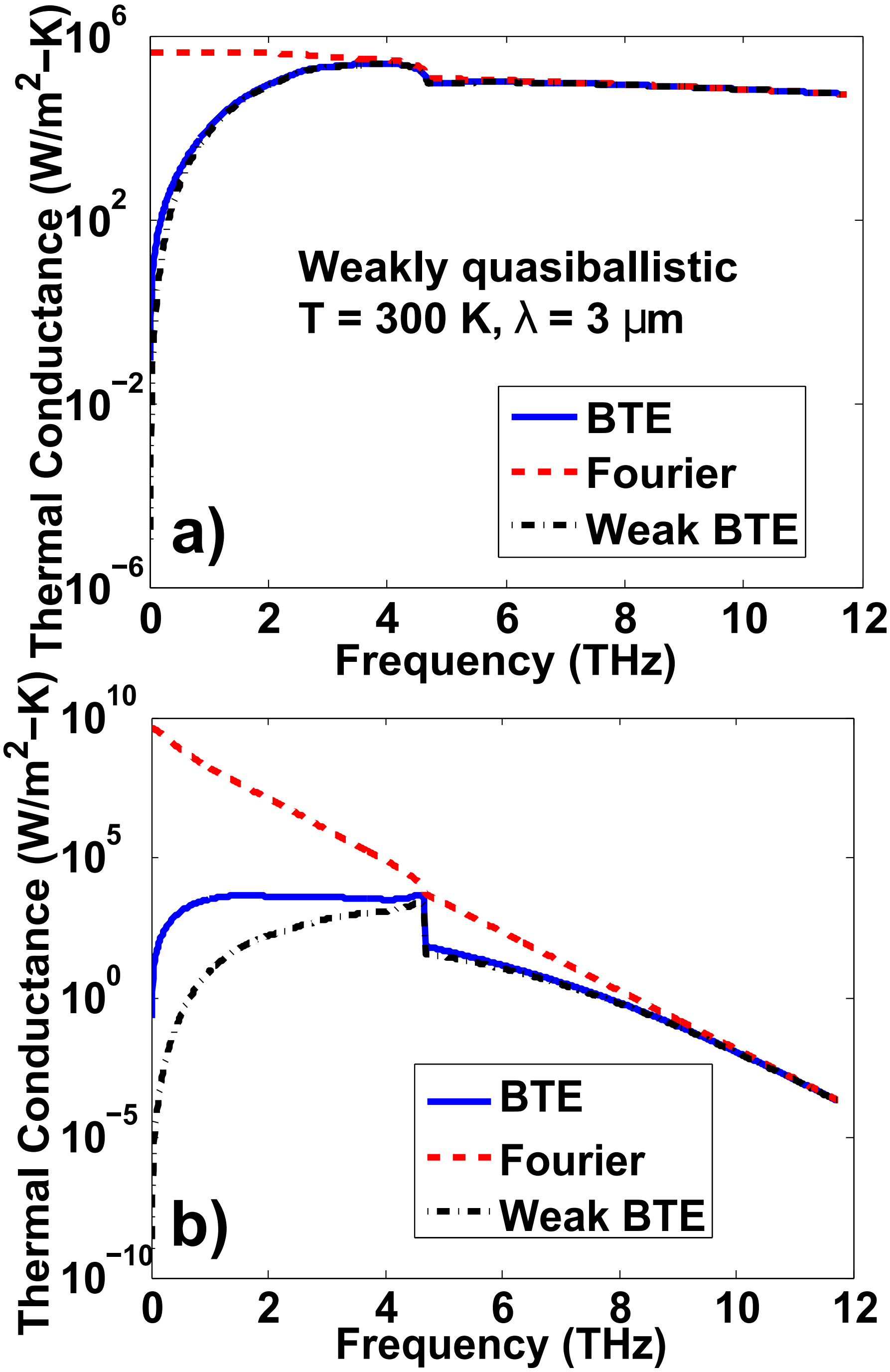

Figure 4.2: Spectral thermal conductance σ_ω in the (a) weakly quasiballistic regime and (b) strongly quasiballistic regime. The BTE solutions are given by the solid lines, the Fourier solution by the dashed lines, and the weak BTE solution by the dash-dotted lines.

In weakly quasiballistic regime, where $\mathrm{Kn}_\omega^2 \sim 1$ but $H_\omega \ll 1$ (Fig. 4.2(a)), $H_\omega + 1 \rightarrow 1$ and Eq. (4.11) reduces to $\sigma_\omega = \sigma_f S_{weak}(\mathrm{Kn}_\omega)$, where $S_{weak}(\mathrm{Kn}_\omega)$ is the same as the term in the brackets of Eq. (4.9). In this regime, Fourier's law overpredicts the heat flux but the weak BTE solution still accurately describes the spectral heat distribution. From Fig. 4.2(b), we see that the heat contribution from low frequency phonons is suppressed compared to the Fourier's law prediction.

In the strongly quasiballistic regime (Fig. 4.2(b)), the weak BTE solution does not accurately explain the spectral conductance and we must instead use Eq. (4.11). The full BTE solution predicts a more gradual suppression than the weak BTE solution for those low frequency phonons whose relaxation times are comparable to or greater than the thermal decay time Γ. This discrepancy is due to the correction term $H_\omega + 1$, which approaches its maximum value at low frequencies and reduces the suppression effects. Rewriting H_ω into $\Lambda_\omega/(v_\omega\Gamma)$ in Eq. (4.11), we find that our new suppression function decreases as $1/\Lambda_\omega$ in the long MFP limit, in agreement with the ballistic limit of the BTE(*21*) while $S_{weak}(\mathrm{Kn}_\omega)$ predicts a steeper slope, $1/\Lambda_\omega^2$, which is inconsistent with the ballistic limit. Therefore, our new suppression function provides a more accurate prediction of the heat flux suppression over the entire spectrum of phonons compared to the approximate approaches in the literature.(*126*, *128*)

4.5 Application

We now show the utility of these insights by demonstrating how our new suppression function may be used to more accurately measure MFP spectra. As proposed by Minnich(*118*), the apparent thermal conductivities can be related to the MFP distribution by the equation $k_{app} = \int_0^\infty S(\Lambda_\omega) f(\Lambda_\omega) d\Lambda_\omega$ where $S(\Lambda_\omega)$ is the suppression function, the phonon MFP Λ_ω is the independent variable and $f(\Lambda_\omega)$ is the desired MFP distribution. If the apparent thermal conductivities are experimentally

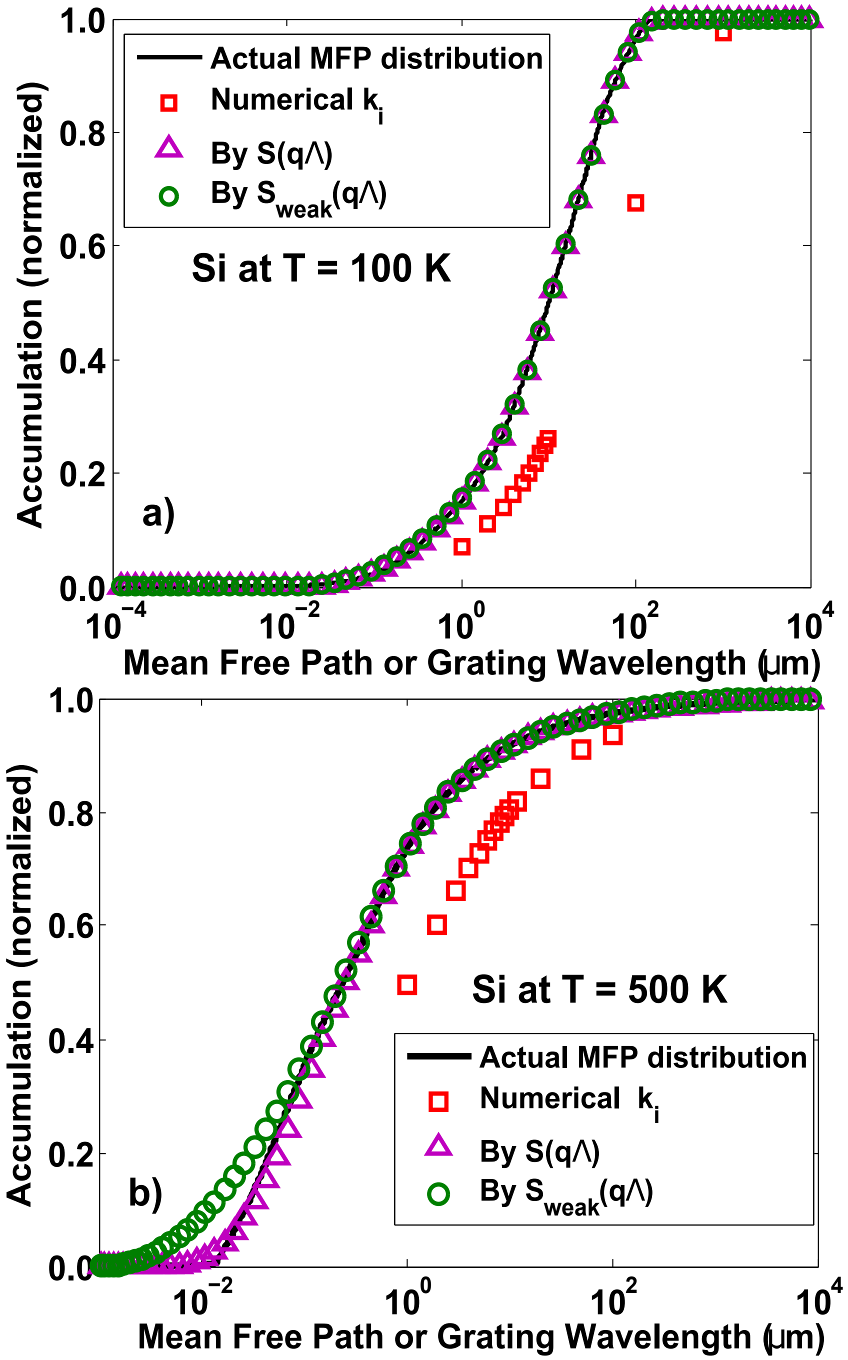

Figure 4.3: Example MFP reconstructions for silicon at (a) 100 K and (b) 500 K using numerically simulated data. Plotted are the analytical MFP distribution (solid line), the numerical apparent thermal conductivities (squares), the reconstructed MFP distributions by the general suppression function (triangles) and by the weak suppression function (circles). The x-axis corresponds to the MFP for the distributions and to the grating wavelength for the thermal conductivity data.

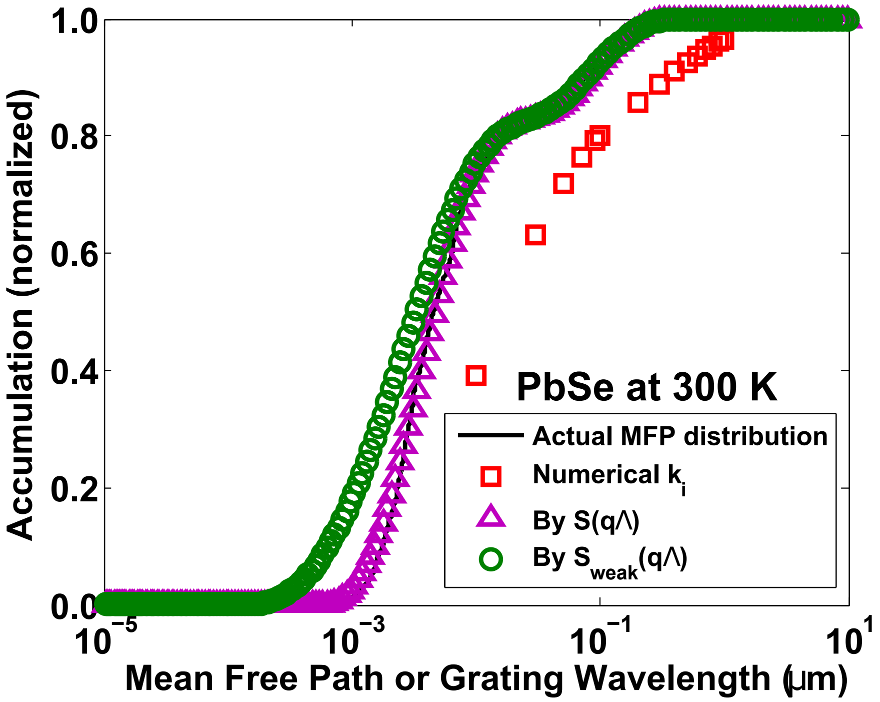

Figure 4.4: Example MFP reconstructions for PbSe at 300 K using numerically simulated data. Plotted are the analytical MFP distribution (solid line), the numerical apparent thermal conductivities (squares), the reconstructed MFP distributions by the general suppression function (triangles) and by the weak suppression function (circles). The x-axis corresponds to the MFP for the distributions and to the grating wavelength for the thermal conductivity data.

measured and the suppression function is known, then the MFP distribution can be reconstructed by solving the integral equation as an inverse problem.

From our analysis, we have already derived the necessary suppression function $S(\mathrm{Kn}_\omega, H_\omega)$ in Eq. (4.11). However, this suppression function depends both on the independent variable, the phonon MFP Λ_ω, as well as the unknown relaxation time τ_ω. To perform the reconstruction, Λ_ω should be the only unknown variable.

To overcome this problem, we rewrite τ_ω into Λ_ω/v_ω and assume that the phonon group velocity v_ω is equal to the average sound velocity v_s. This assumption is justified since for long MFP phonons for which the correction term is important, the group velocity of phonons is close to the sound speed, while for short MFP phonons this term is negligible and the choice of the velocity is irrelevant. The reconstruction is also insensitive to the precise choice of the value of v_s. For example, for PbSe, changing v_s from 2000 m/s to 1000 m/s causes only a 10 % maximum error in the reconstructed MFP distribution. Using this approximation, the suppression function is only a function of the independent variable Λ_ω.

To demonstrate the inversion procedure using this new suppression function, we perform numerical experiments in which we obtain the modified thermal conductivities of Silicon and PbSe at different temperatures for different grating wavelengths from the temperature decay curves predicted by the BTE. These modified thermal conductivities, along with the suppression function, are then used as inputs for the reconstruction procedure. Figs. 4.3 & 4.4 show the results of the MFP reconstruction for Si and PbSe using the general and weak suppression functions.

For materials with a MFP spectrum that is in the range of the experimental length scales, such as Silicon at 100 K, the measurements of the apparent thermal conductivities at different grating wavelengths span almost the entire range of phonon MFP spectrum. In this case, as shown in Fig. 4.3(a), both the weak and new suppression functions yield satisfactory results. However, phonon MFPs vary by orders of magnitude and some part of the spectrum may be inaccessible to experiment. For example, the smallest MFPs of Silicon at 500 K are around 10 nm and the smallest MFPs of PbSe at room temperature are around 1 nm. These length scales are too small to be accessed with present experimental methods, meaning the MFP distribution at small length scales must be extrapolated from measurements at larger length scales. Such an extrapolation requires evaluating the suppression function at large values of the argument, precisely in the range where the correction term to the new suppression function is important. As shown in Figs. 4.3(b) and 4.4, our new suppression function yields more accurate results at short MFPs while the weak suppression function overpredicts the MFP distribution.

4.6 Summary

We have analyzed thermal transport in TTG using the Green's function solution to the frequency-dependent BTE. We identify the thermal decay time relative to the relaxation times as a key nondimensional parameter that separate two quasiballistic transport regimes. If the thermal decay time is much larger than relaxation times, a modified diffusion theory is the formal solution of the BTE, providing theoretical justification for prior interpretations of experimental observations of quasiballistic transport. Further, we demonstrate how MFP spectra may be measured more accurately using our new suppression function.

Now we have both the theoretical tools and experimental techniques to study the microscopic transport processes of thermal phonons in bulk materials. In the next chapter, we will demonstrate a general route to directly study the microscopic transport processes at solid-solid interfaces using experiments. With both approaches, we will be able to obtain a comprehensive picture of nanoscale energy transport in solids.

Chapter 5

PHONON TRANSMISSION COEFFICIENTS AT SOLID INTERFACES

Chapter 5 has been adapted from

(*1*) Chengyun Hua et al. “Fresnel transmission coefficients for thermal phonons at solid interfaces”. In: *In review process* (2016).

5.1 Background

Transport across interfaces in heterogeneous media is a fundamental physical process that forms the basis for numerous widely used technologies. For example, the reflection and transmission of light at interfaces, as described by the Fresnel equations, enables wave-guiding with fiber-optics and anti-reflection coatings, among many other functionalities. Interfaces also play an essential role in phonon-mediated heat conduction in solids.(*129*, *130*) Material discontinuities lead to thermal phonon reflections that are manifested on a macroscopic scale as a thermal boundary resistance (TBR), also called Kapitza resistance, R_k, that relates the temperature drop at the interface to the heat flux flowing across it. TBR exists at the interface between any dissimilar materials due to differences in phonon states on each side of the interface.(*129*) Typical interfaces often possess defects or roughness which can lead to additional phonon reflections and hence higher TBR.

TBR plays an increasingly important role in devices, particularly as device sizes decrease below the intrinsic mean free paths (MFPs) of thermal phonons.(*130*) At sufficiently small length scales, TBR can dominate the total thermal resistance. For instance, the effective thermal conductivity of a superlattice can be orders of magnitude smaller than that of the constituent materials due to high TBR.(*113*, *131–133*) This physical effect has been used to realize thermoelectrics with high efficiency(*9*, *12*) and dense solids with exceptionally low thermal conductivity(*134*). On the other hand, TBR can lead to significant thermal management problems(*101*, *135*, *136*) in applications such as LEDs(*137*, *138*) and high power electronics(*136*, *139*).

Numerous works over several decades have investigated the microscopic origin of TBR at solid-solid interfaces, starting with studies performed at low temperatures (∼ 1 K), in which heat is carried predominantly by phonons with frequencies less than 1 THz.(*140*, *141*) At these low temperatures and for pristine, ordered interfaces, transmission coefficients can be obtained from continuum elastic theory in an analogy with Snell's law for light; this model is known as the acoustic mismatch model (AMM).(*142*, *143*) The AMM was shown to explain the experimentally measured values of TBR at various solid-solid interfaces.(*141*) At higher temperatures (above 1 K), heat transport across the interfaces was found to be sensitive to surface roughness. For the limit of completely diffuse scattering in which transmitted and reflected phonons cannot be distinguished, Swartz constructed the diffuse mismatch model (DMM).(*129*) Despite the success of these models at explaining TBR at low temperatures, they generally fail at temperatures larger than 40 K and are unable to account for the atomistic structure of the interface.

Recent works have focused on remedying these deficiencies. Optical methods enable the routine measurement of TBR over a wide range of temperatures for various metal-dielectric interfaces (*26–30*) as well as at interfaces with variable bonding strength. (*31*, *32*) Other works have examined the temperature dependence of the thermal conductivity(*62*) in nanocrystalline samples. Computational atomistic methods such as molecular dynamics(*144–152*) and atomistic Green's functions(*153–157*) have been extensively applied to obtain the transmission coefficients at interfaces with realistic atomic structure. These calculations generally predict the coefficients to decrease with increasing phonon frequency due to reflections of short wavelength phonons by atomistic roughness, a trend that is supported by basic wave physics and indirectly by experiment.(*62*, *158*) Despite all of these works, however, an unambiguous determination of the transmission coefficients at an actual interface has not yet been reported.

Here, we report the first measurements of the thermal phonon transmission coefficients at a solid interface using a combination of experimental observations of quasiballistic transport as introduction in Chapter 4 and advances in ab-initio transport modeling based on the Boltzmann transport equation (BTE) that are presented in Chapter 3. Unlike prior works in which considerable ambiguity remained in the values of the coefficients, our approach places tight constraints on the allowed spectral transmission profile. Applying our approach in conjunction with transmission electron microscopy (TEM), we are able to directly link atomic structure to the spectral content of heat crossing the interface for the first time. Our approach demonstrates a general route to directly experimentally study the microscopic transport processes governing interfacial heat conduction.

5.2 TDTR with ab-initio phonon transport modeling

Our measurement is based on the TDTR experiment, an optical pump-probe technique that is used to characterize thermal properties on micron length scales. In this experiment, a femtosecond pulsed laser beam is split into a pump and a probe beam. The pump pulse train is modulated at a frequency from 1 to 15 MHz to enable lock-in detection, and is then used to impulsively heat a metal film coated on the sample. The transient temperature decay at the surface is detected as a change in optical reflectance by the probe beam.(*159*) Extracting thermal properties requires solving a simple inverse problem in which the measured data sets are related to the desired properties by a macroscopic transfer function based on a multilayer heat diffusion model.(*160*, *161*) The thermal properties, such as substrate thermal conductivity and metal-substrate interface conductance are varied until the data and simulation match.

Although this approach is widely used, it has the drawback that the microscopic phonon properties are averaged into a single number, the interface conductance, resulting in minimal constraints on the allowed transmission coefficients. In this work, we instead aim to directly and unambiguously extract the transmission coefficients from TDTR data by replacing the macroscopic transfer function based on Fourier's law with a microscopic transfer function based on ab-initio phonon transport modeling. Mathematically, we write this problem as:

$$g = H(T_{12}(\omega)), \tag{5.1}$$

where $T_{12}(\omega)$ are the phonon frequency dependent transmission coefficients from layer 1, the metal transducer film, to layer 2, the substrate; H is the transfer function based on ab-initio phonon transport modeling; and g is the TDTR experimental data consisting of multiple transient data sets with different modulation frequencies. This equation represents an inverse problem for the transmission coefficients that can in principle be solved in an analogous manner to that employed for the macroscopic transfer function.

Although simple in principle, several challenges arise when trying to implement this strategy. First, it is essential that part of the non-equilibrium phonon distribution emerging from the interface propagate into the substrate ballistically. As illustrated in Fig. 5.1, when MFPs are much shorter than the characteristic length scale of the thermal gradient, information about the phonon distribution at the interface is lost due to scattering. On the other hand, if some phonons have sufficiently long MFPs, the non-equilibrium phonon distribution penetrates into the substrate and affects the resulting heat conduction, thereby providing direct information about the spectral content of heat crossing the interface. Fortunately, many experimental reports have demonstrated clear evidence of this quasiballistic heat transport regime

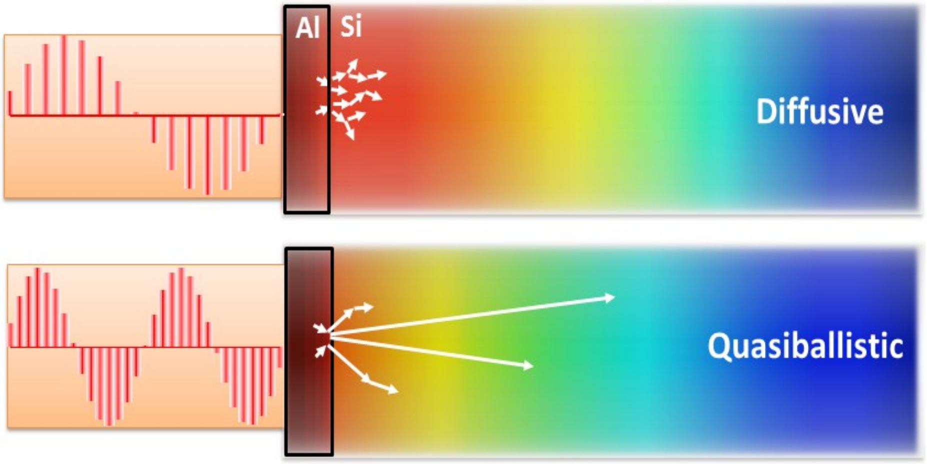

Figure 5.1: Schematic of the principle underlying the measurement of transmission coefficients. If the characteristic length scale of the thermal transport is much longer than the phonon MFPs, information about the interfacial distribution is lost due to strong scattering. If some MFPs are comparable to the thermal length scale, the non-equilibrium distribution at the interface propagates into the substrate where it can be detected.

in different material systems (*20*, *23*, *25*, *162–164*) including the transient thermal grating experiments discussed in Chapter 4. In this work, we interpret these effects as fundamentally originating from the non-equilibrium phonon distribution emerging from the interface.

Second, we must determine the microscopic transfer function that maps the transmission coefficients directly to the TDTR signal without any artificial fitting parameters. It is this step that has long impeded efforts to study interfaces due to the challenge of solving the BTE for the TDTR experiment. A number of simplified models(*79*, *126*, *164–168*) have been proposed to explain these observations. However, all of these models make various approximations that limit their predictive capability.

In this work, we overcome this challenge using two recent advances we reported for rigorously solving the spectral BTE under the relaxation time approximation (RTA), with no additional simplifications, that yield a factor of 10^4 speedup compared to existing methods and allows the first ab-initio phonon transport modeling of TDTR free of artificial parameters or simplifications of the phonon dispersion. First, we have obtained an analytical solution of the spectral BTE in a semi-infinite substrate subject to an arbitrary heating profile.(*169*) Second, we have employed a series expansion method to efficiently solve the BTE in the thin transducer film.(*170*) In this work, these two solutions are combined using a spectral interface condition(*79*) that expresses the conservation of heat flux at each phonon frequency to yield the necessary microscopic transfer function $H(T_{12}(\omega))$.

5.3 Derivation of transfer function $H(T_{12}(\omega))$

We now describe the derivation of the transfer function $H(T_{12}(\omega))$ that maps transmission coefficients to the TDTR amplitude and phase data. Thermal transport in TDTR experiments, assuming only cross-plane heat conduction, is described by the one-dimensional (1D) spectral Boltzmann transport equation (BTE) under relaxation time approximation (RTA)(*22*),

$$\begin{aligned} \frac{\partial g_\omega}{\partial t} &+ \mu v_\omega \frac{\partial g_\omega}{\partial x} = -\frac{g_\omega + f_0(T_0) - f_0(T)}{\tau_\omega} + \frac{Q_\omega}{4\pi} && (5.2) \\ f_0(T) &= \frac{1}{4\pi}\hbar\omega D(\omega) f_{BE}(T) \approx f_0(T_0) + \frac{1}{4\pi} C_\omega \Delta T, && (5.3) \end{aligned}$$

where $g_\omega = \hbar\omega D(\omega)[f_\omega(x,t,\mu) - f_0(T_0)]$ is the deviational distribution function, $f_0 = f_0(x,t)$ is the equilibrium distribution function, $\mu = cos(\theta)$ is the directional cosine, v_ω is the phonon group velocity, τ_ω is the phonon relaxation time, and $Q_\omega(x,t)$ is the spectral volumetric heat generation. Assuming a small temperature rise, $\Delta T = T - T_0$, relative to a reference temperature, T_0, the equilibrium distribution is proportional to ΔT, as shown in Eq. (5.3). Here, $\hbar$ is the reduced Planck constant, ω is the phonon frequency, $D(\omega)$ is the phonon density of states, f_{BE} is the Bose-Einstein distribution, and $C_\omega = \hbar\omega D(\omega)\frac{\partial f_{BE}}{\partial T}$ is the mode specific heat. The volumetric heat capacity is then given by $C = \int_0^{\omega_m} C_\omega d\omega$ and the Fourier thermal conductivity $k = \int_0^{\omega_m} k_\omega d\omega$, where $k_\omega = \frac{1}{3}C_\omega v_\omega \Lambda_\omega$ and $\Lambda_\omega = \tau_\omega v_\omega$ is the phonon MFP. To close the problem, energy conservation is used to relate g_ω to ΔT, given by

$$\int \int_0^{\omega_m} \left[\frac{g_\omega(x,t)}{\tau_\omega} - \frac{1}{4\pi}\frac{C_\omega}{\tau_\omega}\Delta T(x,t) \right] d\omega d\Omega = 0, \tag{5.4}$$

where Ω is the solid angle in spherical coordinates and ω_m is the cut-off frequency. Note that summation over phonon branches is implied without an explicit summation sign whenever an integration over phonon frequency or MFP is performed.

Before we solve Eq. (5.2), let us first briefly review the signal formation in TDTR. Since the thermal response given by the BTE is a linear time-invariant system, the output transient signal $Z(t)$ of TDTR can be represented in terms of frequency response solution through the following equation(*161*)

$$Z(t) = \sum_{n=-\infty}^{\infty} H(\omega_0 + n\omega_s) e^{in\omega_s t}, \tag{5.5}$$

where ω_0 is the reference angular frequency of the periodic heating, ω_s is the angular sampling frequency set by the repetition rate of the laser pulses, and $H(\eta)$ is surface temperature response subject to a periodic heating at frequency η. Therefore, to study the transient heat transport in TDTR, it is equivalent to solve the modulated heat conduction problem in the same geometry, a double-layer structure of a metal film on a substrate as shown in Fig. 5.2.

We now divide our discussion into three parts: transducer film, substrate, and interface. While the calculations for transducer film and substrate are treated using different techniques, the solutions in those two layers depend on each other through the appropriate interface conditions.

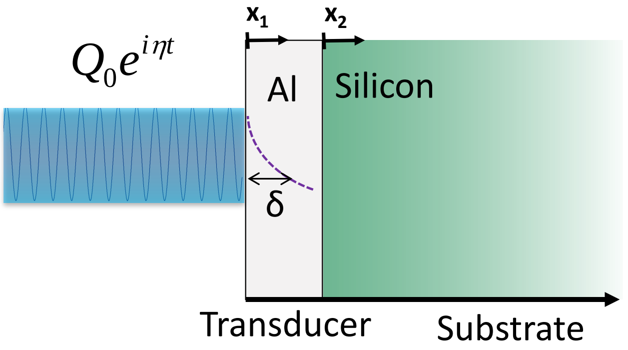

Figure 5.2: 2D schematic of the experimental configuration subject to a modulated heating source: a double layer structure of a transducer film on a substrate (sample). Q_0 is the amplitude of the heating source, η is angular modulation frequency, δ is the optical penetration depth of the heating source, and x is the cross-plane transport direction. x_1 and x_2 correspond to the coordinate systems used in transducer and substrate accordingly.

Transducer film

The metal thin film serves as an optical transducer that absorbs the incident optical energy, while also enabling the observation of temperature decay through the thermoreflectance coefficient. In our work, we neglect electrons and consider that heat is only carried by phonons in Al. This approximation is supported by prior works that found that the direct electron-phonon coupling transport mechanism is negligible for the materials considered here,(*26*, *171*, *172*) and thus the presence of electrons in our model is not necessary to accurately describe interfacial thermal transport for Al/Si interfaces. Moreover, in Section 5.11, we demonstrate the effects of electrons in Al are minimal to the TDTR signals.

Since the system is modulated at a given frequency η, we can assume that both $g_{1\omega}$ and ΔT_1 are of the form $e^{i\eta t}$. The volumetric heat generation in thin film is given by $Q_\omega = Q^0_\omega e^{i\eta t} e^{-x_1/\delta}$, where the amplitude of heating source $Q_0 = \int_0^{\omega_m} Q^0_\omega d\omega$. We also assume that phonons are specularly reflected at $x_1 = 0$, *i.e.* $\widetilde{g}_{1\omega}(x_1 =$

$0, \mu) = \widetilde{g}_{1\omega}(x_1 = 0, -\mu)$. Substituting $g_{1\omega} = \widetilde{g}_{1\omega}(x_1, \mu)e^{i\eta t}$, $\Delta T_1 = \Delta\widetilde{T}_1(x_1)e^{i\eta t}$ and the specular boundary condition at $x_1 = 0$ into Eq. (5.2) leads to a first-order ODE for $\widetilde{g}_{1\omega}(x_1, \mu)$, and its solution is given by

$$\begin{aligned}
\widetilde{g}^{+}_{1\omega}(x_1, \mu) &= B_\omega e^{-\frac{\gamma_{1\omega}}{\mu}(d+x_1)} + \int_0^d \frac{C_{1\omega}\Delta\widetilde{T}(x_1') + Q^0_\omega e^{-x/\delta}\tau_{1\omega}}{4\pi\Lambda_{1\omega}\mu} e^{\frac{\gamma_{1\omega}}{\mu}(x_1'+x_1)} dx_1' \\
&+ \int_0^{x_1} \frac{C_{1\omega}\Delta\widetilde{T}(x_1') + Q^0_\omega e^{-x/\delta}\tau_{1\omega}}{4\pi\Lambda_{1\omega}\mu} e^{\frac{\gamma_{1\omega}}{\mu}(x_1'-x_1)} dx_1' \ (\mu \in (0, 1]) \quad (5.6) \\
\widetilde{g}^{-}_{1\omega}(x_1, \mu) &= B_\omega e^{\frac{\gamma_{1\omega}}{\mu}(d-x_1)} \\
&- \int_x^d \frac{C_{1\omega}\Delta\widetilde{T}(x_1') + Q^0_\omega e^{-x/\delta}\tau_{1\omega}}{4\pi\Lambda_{1\omega}\mu} e^{\frac{\gamma_{1\omega}}{\mu}(x_1'-x_1)} dx_1' \ (\mu \in [-1, 0]), \quad (5.7)
\end{aligned}$$

where $\gamma_{1\omega} = (1 + i\eta\tau_{1\omega})/\Lambda_{1\omega}$, d is the film thickness, and B_ω are the unknown coefficients determined by the interface condition at $x_1 = d$. Here, $\widetilde{g}^{+}_{1\omega}(x_1, \mu)$ indicates the forward-going phonons and $\widetilde{g}^{-}_{1\omega}(x_1, \mu)$ the backward-going phonons.

To close the problem, we plug Eqs. (5.6) & (5.7) into Eq. (5.4) and obtained an integral equation for temperature as:

$$\Delta\widetilde{T}(\widehat{x}_1) - \int_0^1 \Delta\widetilde{T}(\widehat{x}_1')K(\widehat{x}_1', \widehat{x}_1)d\widehat{x}_1' = \int_0^{\omega_m} B_\omega F^1_\omega(\widehat{x}_1)d\omega + F^2(\widehat{x}_1), \quad (5.8)$$

where $\widehat{x}_1 = x_1/d$. The kernel function $K(\widehat{x}_1', \widehat{x})$ is given by

$$K(\widehat{x}_1', \widehat{x}_1) = \frac{1}{2\int_0^{\omega_m} \frac{C_{1\omega}}{\tau_{1\omega}}d\omega} \int_0^{\omega_m} \frac{C_{1\omega}}{\tau_{1\omega}\mathrm{Kn}_{1\omega}} \{E_1[\widehat{\gamma}_{1\omega}(\widehat{x}_1' + \widehat{x}_1)] + E_1[\widehat{\gamma}_{1\omega}|\widehat{x}_1' - \widehat{x}_1|]\}d\omega \quad (5.9)$$

and the two inhomogeneous functions are given by

$$\begin{aligned}
F^1_\omega(\widehat{x}_1) &= \frac{2\pi}{\int_0^{\omega_m} \frac{C_{1\omega}}{\tau_{1\omega}}d\omega} \frac{1}{\tau_{1\omega}} \{E_2[\widehat{\gamma}_{1\omega}(1 + \widehat{x}_1)] + E_2[\widehat{\gamma}_{1\omega}(1 - \widehat{x}_1)]\} \quad (5.10) \\
F^2(\widehat{x}_1) &= \frac{2\pi}{\int_0^{\omega_m} \frac{C_{1\omega}}{\tau_{1\omega}}d\omega} \int_0^1 \int_0^{\omega_m} \frac{Q^0_\omega e^{-\rho\widehat{x}_1'}}{\mathrm{Kn}_{1\omega}} \{E_1[\widehat{\gamma}_{1\omega}(\widehat{x}_1' + \widehat{x}_1)] + E_1[\widehat{\gamma}_{1\omega}|\widehat{x}_1' - \widehat{x}_1|]\}d\omega d\widehat{x}' \quad (5.11)
\end{aligned}$$

where $\mathrm{Kn}_{1\omega} = \Lambda_{1\omega}/d$ is the Knudsen number, $\widehat{\gamma}_{1\omega} = \frac{1+i\eta\tau_{1\omega}}{\mathrm{Kn}_{1\omega}}$, and $E_n(x)$ is the exponential integral given by(*21*):

$$E_n(x) = \int_0^1 \mu^{n-2}e^{-\frac{x}{\mu}}d\mu. \quad (5.12)$$

We apply the spectral method introduced in Section 3.3 to efficiently solve Eq. (5.8). Briefly, the functions in Eq. (5.8) can be expanded as a finite cosine series, such as

$$\Delta\widetilde{T}_{1(N)}(\widehat{x_1}) \approx \sum_{n=0}^{N} t_n \cos(n\pi\widehat{x_1}) \tag{5.13}$$

and

$$\begin{aligned} K_{(N)}(\widehat{x},\widehat{x'}) = \frac{1}{4}k_{00} \quad &+ \quad \frac{1}{2}\sum_{m=1}^{N} k_{m0} cos(m\pi\widehat{x}) + \frac{1}{2}\sum_{n=1}^{N} k_{0n} cos(n\pi\widehat{x'}), \\ &+ \quad \sum_{m=1}^{N}\sum_{n=1}^{N} k_{mn} cos(m\pi\widehat{x}) cos(n\pi\widehat{x'}) \end{aligned} \tag{5.14}$$

where N is the truncated basis number, and t_n's and k_{nm}'s are the Fourier coefficient. Similarly, $F^1_\omega(\widehat{x_1})$ and $F^2(\widehat{x_1})$ are also expanded in term of cosines. Following the steps in the above reference, we can express the temperature as

$$\Delta\widetilde{T}_1(\widehat{x_1}) = [\underline{\underline{A}}^{-1}(\underline{\underline{f_1}}\,\underline{B} + \underline{f_2})]^T \underline{\phi(x)} \tag{5.15}$$

where the matrix $\underline{\underline{A}}$ contains elements $A_{00} = 1 - \frac{k_{00}}{4}$, $A_{0n} = -\frac{1}{2}k_{0n}$, $A_{n0} = -\frac{k_{n0}}{4}$, $A_{nn} = 1 - \frac{1}{2}k_{nn}$ and $A_{nm} = -\frac{1}{2}k_{nm}$ $(m \neq n \neq 0)$ and $\underline{B}$ is a N_ω column vector of the unknown coefficients B_ω, where N_ω is the number of discretization in phonon frequency. $\underline{\underline{f_1}}$ is a $N \times N_\omega$ matrix, consisting of the Fourier coefficients of $F^1_{\omega_i}(\widehat{x_1})$ evaluated at each phonon frequency ω_i and $\underline{f_2}$ is a N column vector, consisting of the Fourier coefficients of $F^2(\widehat{x_1})$.

Then, $\widetilde{g}^+_{1\omega}(x_1, \mu)$ and $\widetilde{g}^-_{1\omega}(x_1, \mu)$ can be expressed in terms of the unknown coefficients B_ω by plugging Eq. (5.15) into Eqs. (5.6) and (5.7).

Substrate

The substrate can be treated as a semi-infinite region subject to a surface heat flux. Therefore, the BTE for the substrate becomes

$$i\eta\widetilde{g}_{2\omega} + \mu v_{2\omega}\frac{\partial\widetilde{g}_{2\omega}}{\partial x_2} = -\frac{\widetilde{g}_{2\omega}}{\tau_{2\omega}} + \frac{C_{2\omega}}{4\pi\tau_{2\omega}}\Delta\widetilde{T}(x_2) + \frac{1}{2}P_\omega v_{2\omega}|\mu|\delta(x_2), \tag{5.16}$$

where the unknown coefficients P_ω's are determined through the interface conditions.

We then apply the Green's function method given in Section 3.2. The unknown distribution function in spatial frequency domain is then written as

$$\widetilde{g}_{2\omega}(\eta, \xi_2) = \frac{C_{2\omega}}{4\pi}\frac{\Delta\widetilde{T}_2(\eta, \xi_2) + \frac{1}{2}P_\omega \Lambda_{2\omega}|\mu|/C_{2\omega}}{1 + i\eta\tau_{2\omega} + i\mu\xi_2\Lambda_{2\omega}}, \tag{5.17}$$

and the temperature profile

$$\Delta\widetilde{T}_2(\eta, \xi_2) = \frac{\int_0^{\omega_m} P_\omega v_{2\omega}\frac{1+i\eta\tau_{2\omega}}{(\Lambda_{2\omega}\xi_2)^2}\log\left[1 + \left(\frac{\Lambda_{2\omega}\xi_2}{1+i\eta\tau_{2\omega}}\right)^2\right] d\omega}{\int_0^{\omega_m} \frac{C_{2\omega}}{2\pi\tau_{2\omega}}\left[1 - \frac{1}{\Lambda_{2\omega}\xi_2}\tan^{-1}\left(\frac{\Lambda_\omega\xi_2}{1+i\eta\tau_{2\omega}}\right)\right] d\omega}, \tag{5.18}$$

where ξ_2 is the Fourier variable of x_2.

Again, to express $\widetilde{g}_{2\omega}$ only in terms of unknown coefficients P_ω, we simply plug Eq. (5.18) into Eq. (5.17).

Interface condition

The unknown coefficients in the solutions of transducer film and substrate are obtained by applying appropriate interface conditions. Here, we use the elastic transmission interface condition with mode conversion, closely following the work by Minnich *et al.*(*79*) Briefly, for a given mode i, the heat fluxes outgoing from the interface, $q_{1\omega}^{i-}$ and $q_{2\omega}^{i+}$, must be equal to the reflected and transmitted heat fluxes incident to the interface, $q_{1\omega}^{i+}$ and $q_{2\omega}^{i-}$. By assuming elastic and diffuse scattering, the transmission and reflection process for each phonon frequency is treated independently and the heat flux equality condition must be satisfied for each frequency and polarization.

The interface conditions are

$$\int_0^1 g_{2\omega}^{i+} v_{2\omega}^i \mu d\mu = \sum_j T_{12}^{ji}(\omega) \int_0^1 g_{1\omega}^{j+} v_{1\omega}^j \mu d\mu + \sum_j R_{21}^{ji}(\omega) \int_0^1 g_{2\omega}^{j-} v_{2\omega}^j \mu d\mu, \tag{5.19}$$

$$\int_0^1 g_{1\omega}^{i-} v_{1\omega}^i \mu d\mu = \sum_j T_{21}^{ji}(\omega) \int_0^1 g_{2\omega}^{j-} v_{2\omega}^j \mu d\mu + \sum_j R_{12}^{ji}(\omega) \int_0^1 g_{1\omega}^{j+} v_{1\omega}^j \mu d\mu, \tag{5.20}$$

where $T_{12}^{ji}(\omega)$ is the transmission coefficient of mode j at frequency ω from side 1 to side 2 as mode i, $R_{21}^{ji}(\omega)$ is the reflection coefficient of mode j at frequency ω from side 2 back into side 2 as mode i, and so on. $g_{1\omega}^{i\pm}$ from Sec. 5.3 and $g_{2\omega}^{i\pm}$ from Sec. 5.3 are evaluated at $x_1 = d$ and at $x_2 = 0$, respectively. Given the values of $T_{12}^{ij}(\omega)$, $R_{12}^{ij}(\omega)$, $T_{21}^{ij}(\omega)$ and $R_{21}^{ij}(\omega)$, the unknown coefficients P_ω and B_ω's are obtained by plugging Eqs. (5.6), (5.7), and (5.17) into Eqs. (5.19) and (5.20) and solving the linear system.

The next question is how $T_{12}^{ij}(\omega)$ is related to the other reflection and transmission coefficients. The reflection coefficients are related to the transmission coefficients by energy conservation given by

$$\sum_j T_{12}^{ij}(\omega) + R_{12}^{ij}(\omega) = 1, \tag{5.21}$$

and

$$\sum_j T_{21}^{ij}(\omega) + R_{21}^{ij}(\omega) = 1. \tag{5.22}$$

$T_{21}^{ji}(\omega)$ is related to $T_{12}^{ij}(\omega)$ through the principle of detailed balance, which requires that no net heat flux can transmit across the interface when both materials are at an equilibrium temperature T. Applying this condition to every phonon mode on each side of the interface for each polarization and frequency gives:

$$T_{12}^{ij}(\omega) C_{1\omega}^i v_{1\omega}^i = T_{21}^{ji}(\omega) C_{2\omega}^j v_{2\omega}^j. \tag{5.23}$$

Therefore, we need to specify $T_{12}^{ij}(\omega)$, $R_{12}^{ij}(\omega)$, and $R_{21}^{ij}(\omega)$.

Let us first consider a special case where no mode conversion is allowed ($T_{12}^{ij}(\omega)$, $T_{21}^{ij}(\omega)$, $R_{12}^{ij}(\omega)$, $R_{21}^{ij}(\omega) = 0$ for $i \neq j$). Then, the interface conditions become

$$\begin{aligned} \int_0^1 g_{2\omega}^{i+} v_{2\omega} \mu d\mu &= T_{12}^{ii}(\omega) \int_0^1 g_{1\omega}^{i+} v_{1\omega}^i \mu d\mu + R_{21}^{ii}(\omega) \int_0^1 g_{2\omega}^{i-} v_{2\omega}^i \mu d\mu, \quad (5.24) \\ \int_0^1 g_{1\omega}^{i-} v_{1\omega} \mu d\mu &= T_{21}^{ii}(\omega) \int_0^1 g_{2\omega}^{i-} v_{2\omega}^i \mu d\mu + R_{12}^{ii}(\omega) \int_0^1 g_{1\omega}^{i+} v_{1\omega}^i \mu d\mu, \quad (5.25) \end{aligned}$$

and the detail balance becomes

$$T_{12}^{ii}(\omega) C_{1\omega}^i v_{1\omega}^i = T_{21}^{ii}(\omega) C_{2\omega}^i v_{2\omega}^i. \quad (5.26)$$

Therefore, once $T_{12}^{ii}(\omega)$ is specified, all the other transmission and reflection coefficients are determined. For now, we only consider this special case and neglect the mode conversion in our BTE simulations. In Section 5.11, we show that the mode specific transmission coefficients cannot be resolved by the TDTR measurements and the measurable quantity is $\sum_j T_{12}^{ij}(\omega)$ instead of individual transmission coefficients. For simplicity, we will use $T_{12}(\omega, p)$ rather than the summation. Note that the only inputs to our calculation are the phonon dispersions and lifetimes, calculated using density functional theory (DFT) with no adjustable parameters by Jesús Carrete and Natalio Mingo using ShengBTE(*88*) and Phonony(*173*) from interatomic force constants obtained with VASP.(*91–94*) The details about converting the ab-initio calculations to an equivalent isotropic dispersion to reduce computational cost can be found in Appendix C. For Aluminum, the dispersion is calculated using the harmonic interatomic force constants, which are generated using Density Functional Perturbation Theory (DFPT) implemented in the ab-initio simulation package Quantum Espresso. The details about calculating phonon lifetimes in Al are given in Appendex D.5. Fig. 5.3 plots the phonon density of states, group velocity, and relaxation times as a function of phonon frequency in both Al and Si for the three acoustic branches.

The only unknown parameters in this model are the spectral transmission coefficients $T_{12}(\omega)$. In this work, we use $T_{12}(\omega)$ as the fitting parameter rather than using models like a gray model or DMM. The result of the BTE modeling can be written into a compact transfer function given as

$$g = H(T_{12}(\omega)), \tag{5.27}$$

where H is the microscopic transfer function based on BTE modeling, and g is the TDTR experimental data consisting of multiple transient data sets with different modulation frequencies. This microscopic transfer function maps the spectral transmission coefficients $T_{12}(\omega)$ into an observable quantity g. This equation can be solved as an inverse problem for the transmission coefficients. Therefore, we are able to interpret phonon transmission coefficients across an interface directly from the experiments without any artificial fitting parameters.

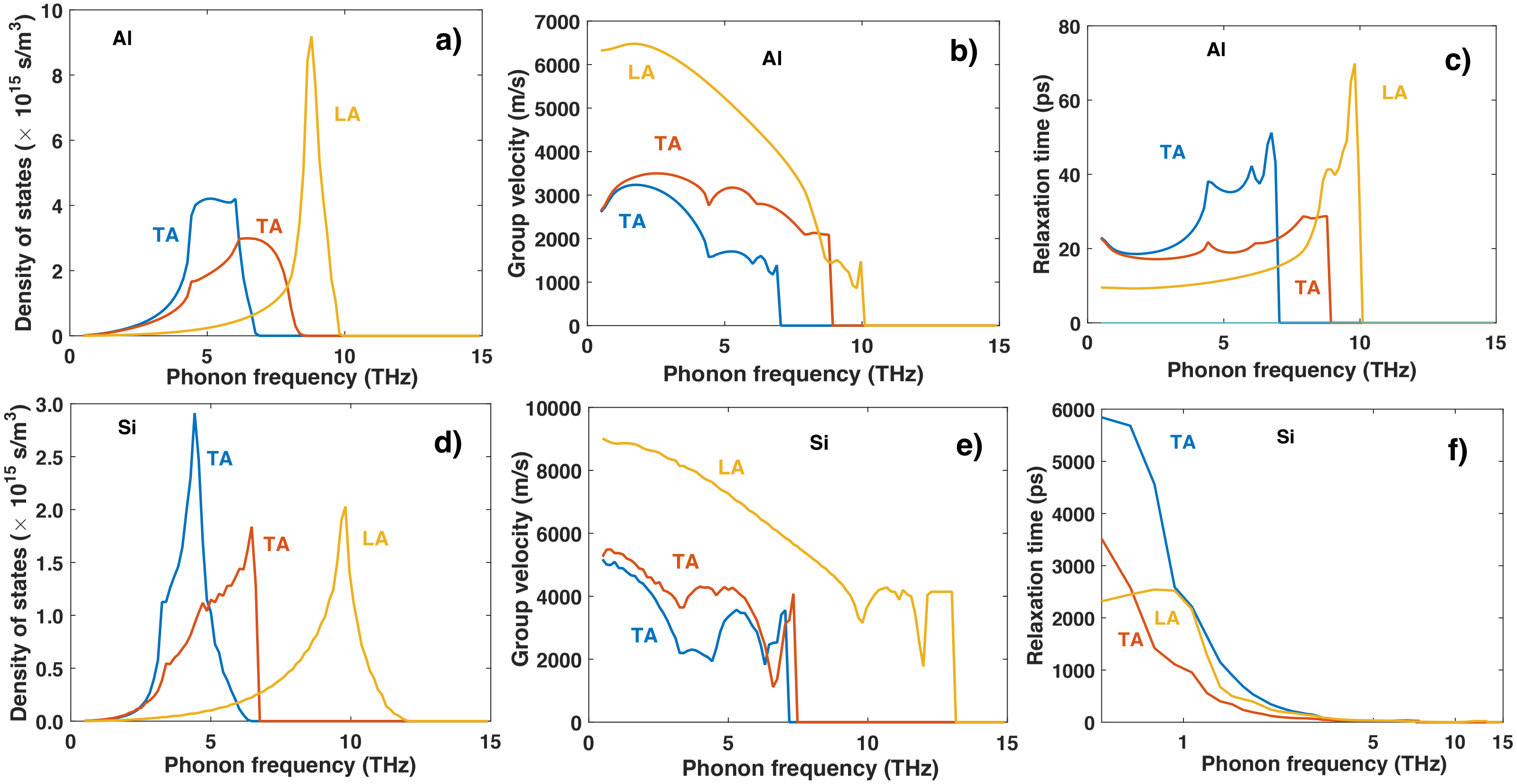

Figure 5.3: (a) Phonon density of states, (b) group velocity, and (c) relaxation times vesus phonon frequency for Al; (d) Phonon density of states, (e) group velocity, and (f) relaxation times versus phonon frequency for Silicon. Blue and red lines represent transverse acoustic modes, and yellow lines represent longitudinal acoustic modes.

5.4 Solution of inverse problem

The final challenge is to solve the inverse problem that identifies the transmission coefficients that best explain the observed data. From the BTE model, we obtain a surface temperature decay curve as a function of time just like the one measured in the experiments. For a given sample, the correct transmission coefficient profile as a function of phonon frequency will minimize the difference between the simulation curves and experimental TDTR traces at all modulation frequencies. By treating the transmission coefficients as fitting parameters, we avoid using the oversimplified models. To solve the inverse problem that identifies the transmission coefficients that best explain the observed data, we utilized particle swarm optimization (PSO) method to search for the optimal profile. The essential goal of PSO method is to minimize the objective function defined as

$$f = \alpha |g_{ab-initio}(T_{12}(\omega)) - g_{measured}| + (1-\alpha) \int \left(\frac{d^2 T_{12}}{d\omega^2} \right)^2 d\omega. \tag{5.28}$$

The first part of the equation evaluates the norm of the difference between the experimentally measured and BTE-simulated TDTR signals given a transmission profile profile $T_{12}(\omega)$. The second part of the equation evaluates the second derivative of the transmission coefficient profile, serving as the smoothness penalty function. Note that the smoothness of the profiles is the only constraint we impose in the objective function. The smoothing parameter α determines the relative importance of the second part to the first part. If $\alpha = 1$, then no smoothness constraint is imposed. Here, we use

$$\alpha = \frac{\int \left(\frac{d^2 T_{12}^0}{d\omega^2} \right)^2 d\omega}{|g_{ab-initio}(T_{12}^0(\omega)) - g_{measured}|}, \tag{5.29}$$

where $T_{12}^0(\omega)$ is the initial profile. The formula is chosen such that the first and second parts of the equation have the same order of magnitude.

To search for the optimal profile that minimizes the objective function, the PSO algorithm randomly initializes a collection of transmission coefficient profiles and evolves them in steps throughout the phase space which contains all possible transmission coefficient profiles. At each step and for each profile, the algorithm evaluates the objective function defined as above. After this evaluation, the algorithm decides how each profile should evolve according to the current best profile. The profile evolves, then the algorithm reevaluates. The algorithm stops when the objective function reaches the desired value. The transmission coefficient profile that achieves the minimum value of the objective function is the optimal profile that explains the data.

However, since the inverse problem is ill-posed, a unique solution does not exist. We use Gibbs sampling to explore adjacent regions of the optimal transmission coefficient profile. We first randomly generated 1000 profiles by perturbing the optimal profile with a smooth function defined using the following formula

$$\delta = A[r_1 \cos(2\pi\omega/\omega_{max} r_2 + 2\pi r_3) + r_4 \sin(2\pi\omega/\omega_{max} r_5 + 2\pi r_6)], \tag{5.30}$$

where the amplitude of the perturbation A is 0.1, and r_1, r_2, r_3, r_4, r_5 and r_6 are random numbers between 0 to 1. We evaluated the objective function at all the perturbed profiles and recorded the values. Then, we started the Gibbs sampling process. At each iteration, we randomly drew a profile, a, from the stored population and compared the value of its corresponding objective function, f_n to the one from the previous step, f_{n-1} evaluated at profile b. If f_n is less than f_{n-1}, we accepted a and kept f_n. If not, a random number r was drawn and compared to $u = p/(1 + p)$, where

$$p = \exp\left(\frac{f_n - f_{n-1}}{T_0}\right). \tag{5.31}$$

If r was smaller than u, then we accepted a and kept f_n. If not, we rejected a and updated f_n to be f_{n-1}. The system temperature, T_0, is chosen such that the stationary distribution is gradually changing. Here, T_0 is set to be the mean value of the objective functions of all the perturbed samples. We kept track of how many times each

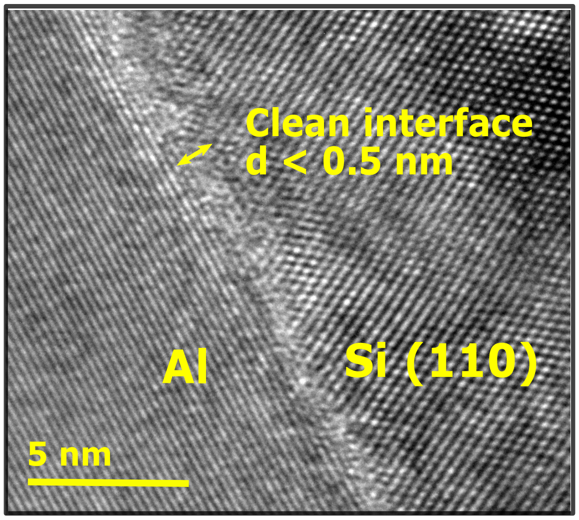

Figure 5.4: TEM image showing the clean interface of an Al/Si sample with the native oxide removed. The interface thickness is less than 0.5 nm.

profile was chosen at each iteration and generated a histogram of the occurrence frequency of each profile. We stopped the sampling process when the histogram became stationary. This occurrence frequency is also called the likelihood of the transmission coefficient profiles. The higher the value of a profile's likelihood is, the more likely the profile could fit the experimentally measured TDTR signals at different modulation frequencies. Thus by combining the PSO method with Gibbs sampling algorithm, we are able to determine the most likely transmission coefficients at the interface between Si and Al.

5.5 Measurements of phonon transmission coefficients

We demonstrate our transmission coefficient measurements on an Al film on Si substrate with the native oxide removed by Hydrofluoric acid prior to Al deposition, yielding a clean interface. The TEM image in Fig. 5.4 shows the interface thickness is less than 0.5 nm. The amplitude and phase of signals from the lock-in amplifier at different modulation frequencies are given in Fig. 5.5. For reference, solving the usual inverse problem with the macroscopic transfer function on this

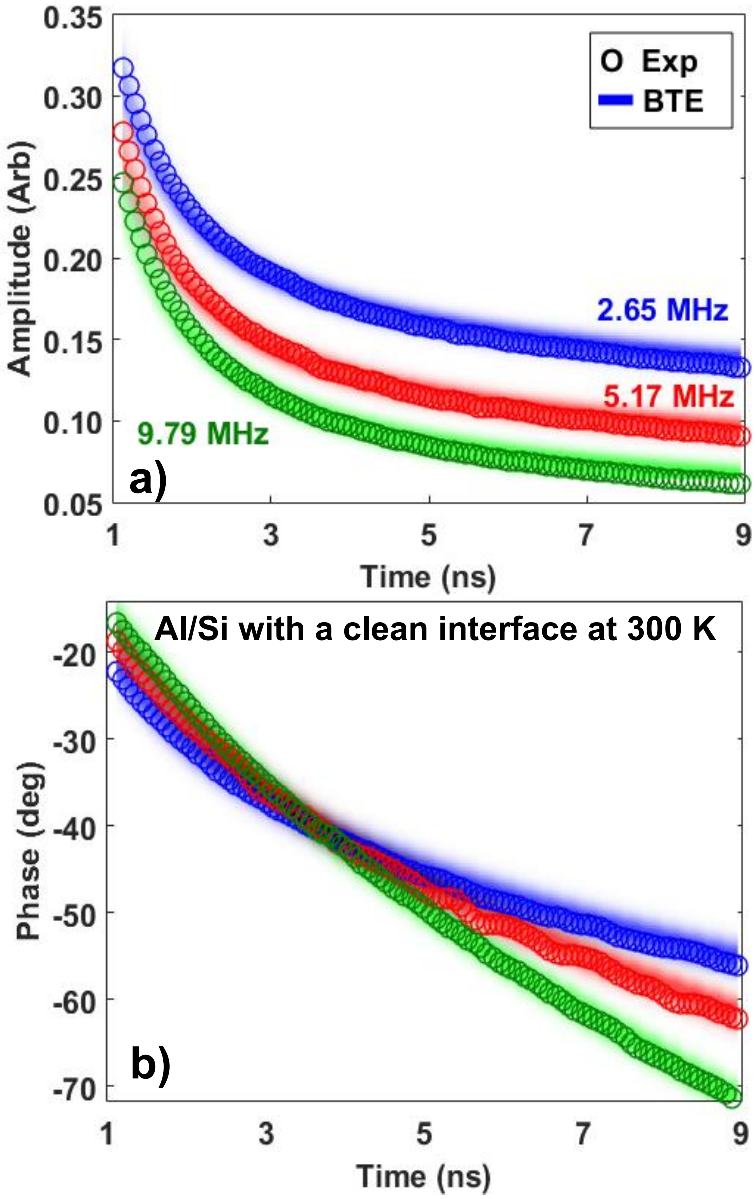

Figure 5.5: Experimental TDTR data (symbols) on this sample at $T = 300$ K for modulation frequencies $f = 2.68$, 5.51 and 9.79 MHz along with the (a) amplitude and (b) phase fit to the data from the BTE simulations (shaded regions), demonstrating excellent agreement between simulation and experiment. The shaded stripes denoted BTE simulations correspond to the likelihood of the measured transmission coefficients possessing a certain value as plotted in Fig. 5.6.

data set yields $G \approx 280$ MW/m^2-K and $k \approx 140$ W/m-K, in good agreement with prior works and literature values for the thermal conductivity of Si.(*20*, *158*) Although the good agreement is often taken as evidence that the macroscopic transfer function is valid for Si, this conclusion is incompatible with several independent ab-initio calculations that clearly show that heat is carried by phonons with MFPs exceeding the thermal penetration depth of TDTR.(*174*, *175*) This prediction has recently been experimentally confirmed by Cuffe *et al* using thermal measurements on variable thickness silicon membranes.(*176*) This fact implies that quasiballistic transport should be readily observable in a typical TDTR experiment on Si, despite the seemingly correct thermal properties measured. This apparent contradiction is resolved by observing that the signal measured in TDTR strongly depends on the spectral profile of the transmission coefficients in the quasiballistic regime, thereby providing the sensitivity necessary to solve the inverse problem given in Eq. 5.27.

We represent the transmission coefficient as a probability density plot, with the color intensity indicating the likelihood that a single transmission coefficient curve passing through a particular point at a given phonon frequency is able to simultaneously explain all of the data in Fig. 5.5, without any other adjustable parameters. The result is shown in Fig. 5.6(a). The figure shows that the transmission coefficient from Si to Al for longitudinal phonons, $\mathrm{T}_{\mathrm{Si}\rightarrow\mathrm{Al}}(\omega)$, starts at unity, its maximum possible value, and decreases steadily to near zero for high phonon frequencies (~ 10 THz). The transmission coefficient profiles for the other polarizations have similar shapes, and so throughout the paper we plot only the longitudinal transmission coefficients for simplicity. The transmission coefficients from Al to Si, $\mathrm{T}_{\mathrm{Al}\rightarrow\mathrm{Si}}(\omega)$ are calculated by satisfying the principle of detailed balance; the relationship between $\mathrm{T}_{\mathrm{Si}\rightarrow\mathrm{Al}}(\omega)$ and $\mathrm{T}_{\mathrm{Al}\rightarrow\mathrm{Si}}(\omega)$ reflects the differences in density of states and group velocity between the two materials. The transmission coefficients for each side of the interface and for the other polarizations are given in Appendix D.2.

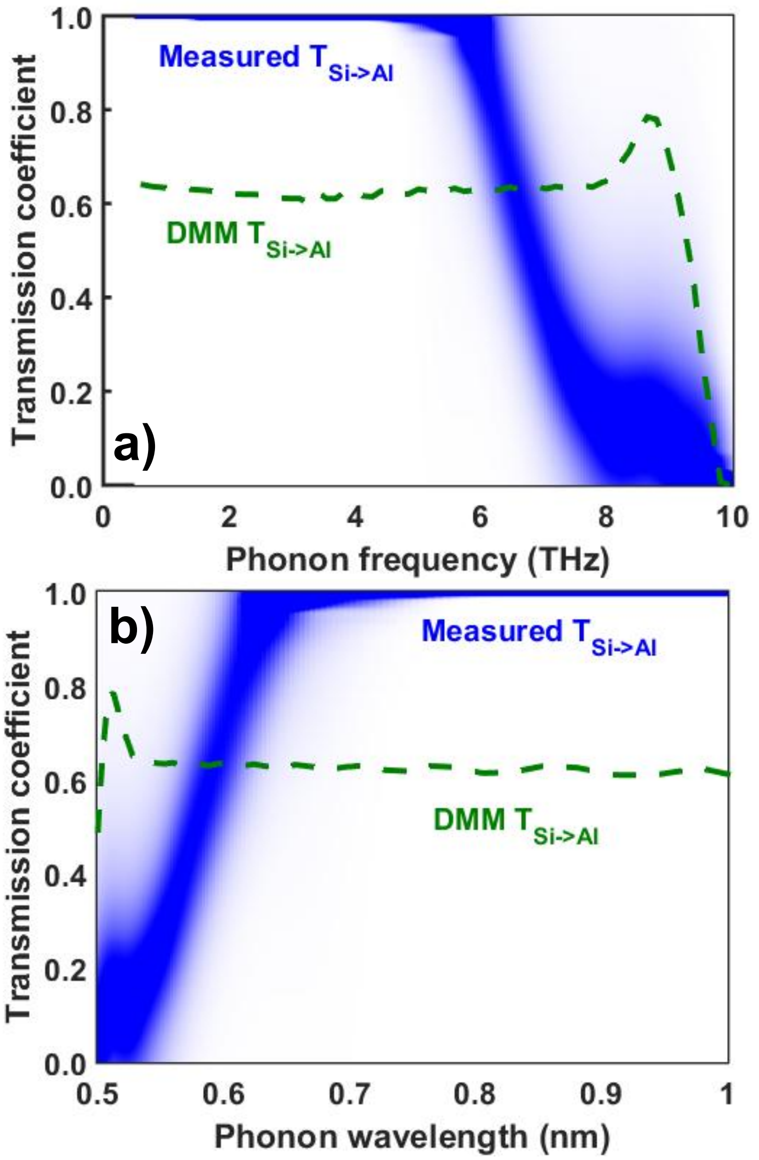

Figure 5.6: Transmission coefficients of longitudinal phonons $T_{Si\rightarrow Al}(\omega)$ (blue shaded region) versus (a) phonon frequency and (b) phonon wavelength, along with the DMM transmission coefficient profile (green dashed line) that gives the same interface conductance as the measured $T_{Si\rightarrow Al}(\omega)$. The intensity of the shaded region corresponds to the likelihood that the transmission coefficient possesses a given value.

Our measured transmission coefficient profile thus indicates that phonons with frequencies less than 4 THz are transmitted to the maximum extent allowed by the principle of detailed balance, while phonons with frequencies larger than 8 THz are nearly completely reflected at the interface. We now examine this result in context with the common models for transmission coefficients. The AMM is often cited as an appropriate model for transmission coefficients at sufficiently low phonon frequencies. At low phonon frequency ($<$ 1 THz), we find that at normal incidence, the transmission coefficients given by AMM is consistent with the measured value. However, the experimental work of Swartz and Pohl(*129*) clearly indicates that even for expitaxial interfaces the validity of the AMM is limited to phonons with frequencies in the hundreds of GHz that carry a small fraction of the heat at room temperature. Therefore, the AMM is not applicable for a wide spectrum of phonons studied here. For short wavelength phonons, the DMM would be expected to apply. At the highest phonon frequencies (shortest wavelengths), the DMM correctly predicts the trend of the measured transmission coefficients tending to zero. However, for most of the phonon spectrum, the DMM is inconsistent with our measurement as discussed in the following section.

5.6 Comparison of conventional models

In this section we provide additional evidence for the inadequacy of conventional models to explain our measurements. We consider two models: the gray model in which the transmission coefficient is a constant, independent of phonon frequency, and the diffuse mismatch model (DMM). The DMM is only determined by the phonon properties of the materials, such as density of states and phonon group velocity. Figs. 5.7(a) & (b) show the transmission coefficients from both sides of the interface using the DMM. The constant transmissivity value is chosen to yield an interface conductance $G = 284$ MW/m^2-K using the formula of Ref. (*79*). The

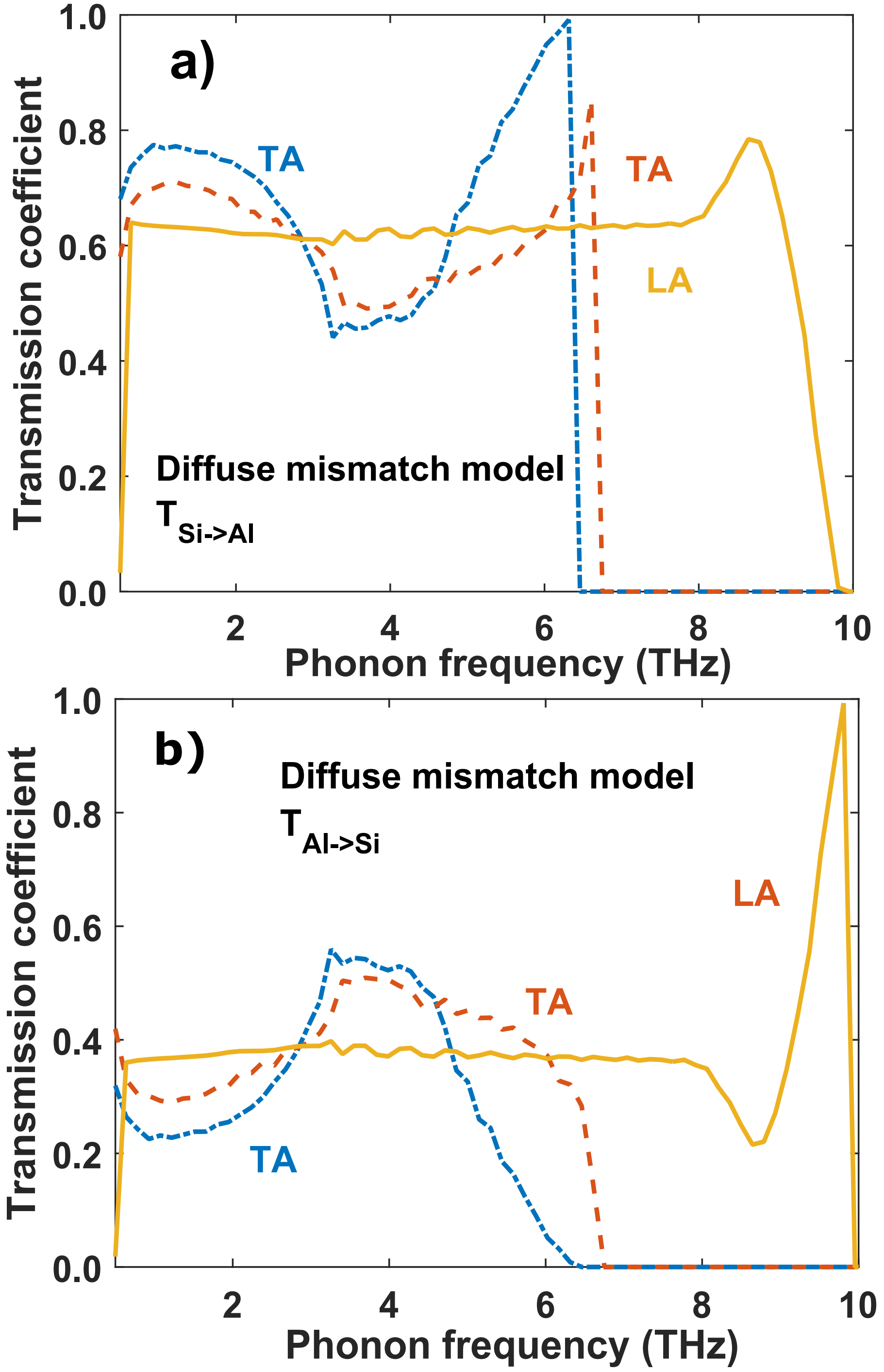

Figure 5.7: Transmission coefficients predicted by diffuse mismatch model (DMM) for each polarization (a) from Si to Al and (b) from Al to Si.

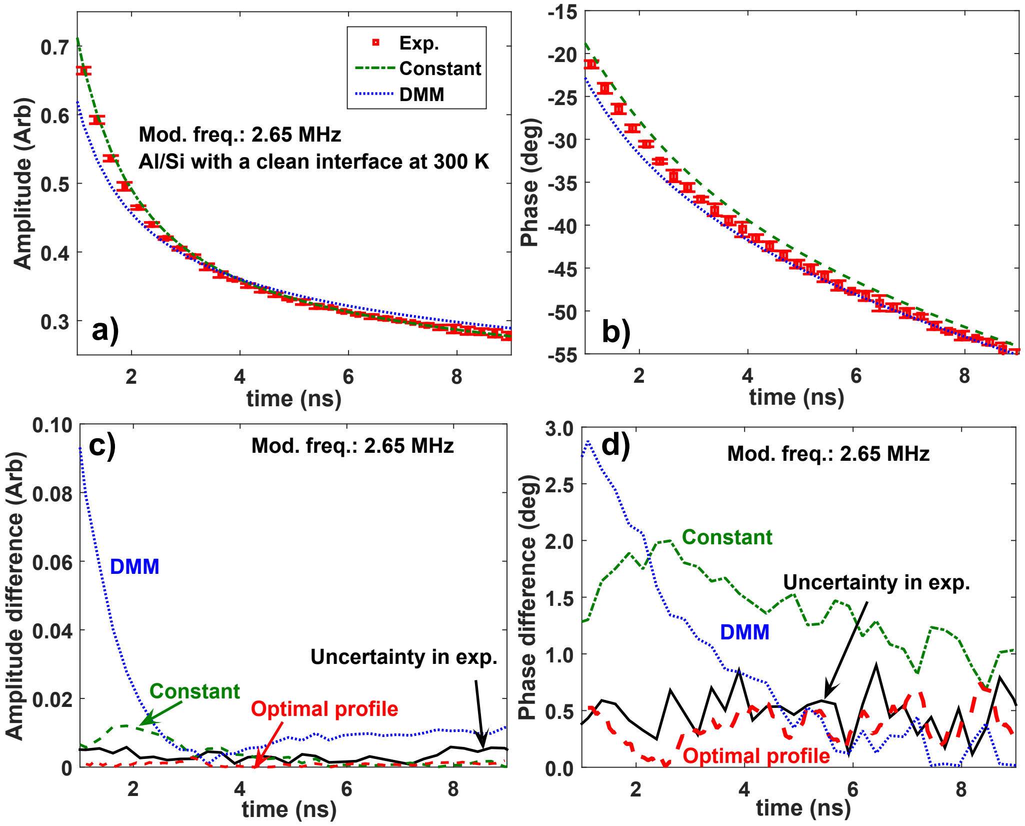

Figure 5.8: Experimental TDTR data (symbols) on Al/Si with a clean interface at 300 K for modulation frequency $f = 2.65$ MHz along with the (a) amplitude and (b) phase compared to the data from the BTE simulations using constant $T_{Si \to Al}$ (dash-dotted lines) and DMM (dotted lines). (c) Amplitude and (d) phase difference between averaged experimental data and the BTE simulations using constant $T_{Si \to Al}$ (dash-dotted lines), DMM (dotted lines), and the optimal profile in Fig. 2 of the main text (dashed lines). The solid line indicates the uncertainty in experiments.

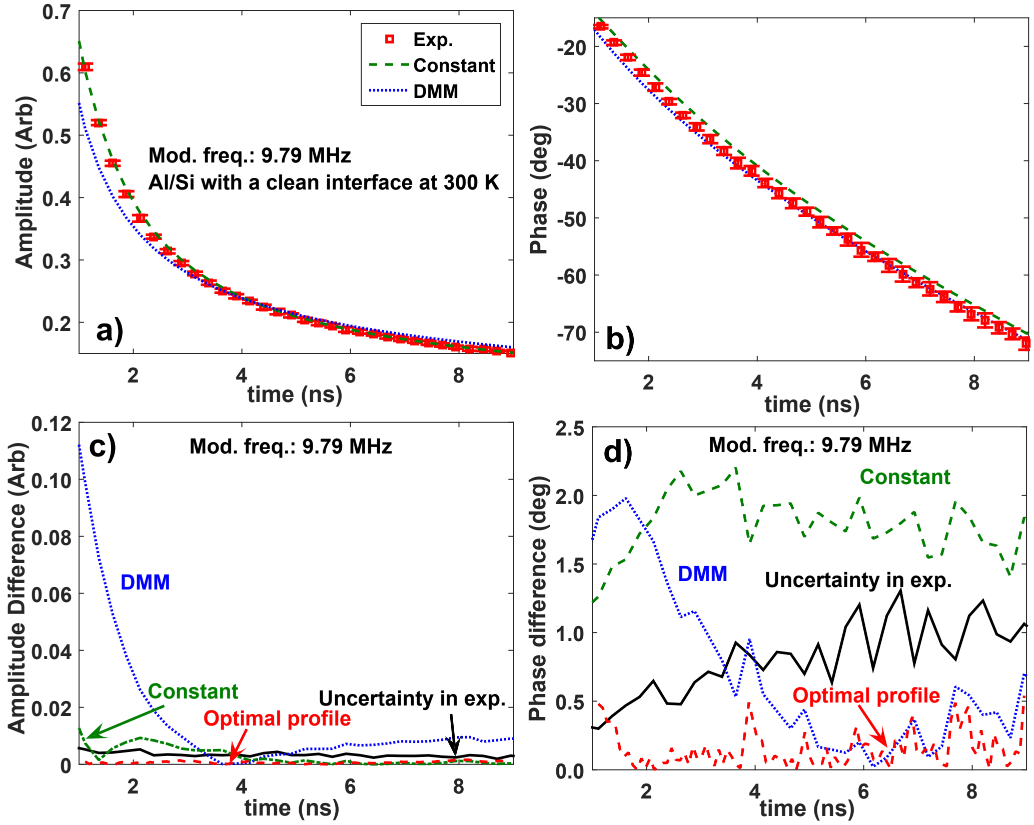

Figure 5.9: Experimental TDTR data (symbols) on Al/Si with a clean interface at 300 K for modulation frequency $f = 9.79$ MHz along with the (a) amplitude and (b) phase compared to the data from the BTE simulations using constant $T_{Si\rightarrow Al}$ (dash-dotted lines) and DMM (dotted lines). (c) Amplitude and (d) phase difference between averaged experimental data and the BTE simulations using constant $T_{Si\rightarrow Al}$ (dash-dotted lines), DMM (dotted lines), and the optimal profile in Fig. 2 of the main text (dashed lines). The solid line indicates the uncertainty in experiments.

measured value for the clean interface is 280 ± 10 MW/m^2-K.

Here, we demonstrate that neither of the models can explain the experimental TDTR data. As shown in Figs. 5.8 & 5.9, the use of a constant transmission coefficient in the BTE model overpredicts the phase values. Similarly, the DMM underpredicts both the amplitude and phase at the early time of the signals. In Figs. 5.8(c) & (d) and 5.9(c) & (d), we show the deviation in amplitude and phase between the averaged experimental data at a given modulation frequency and the BTE simulations using a constant profile and DMM, demonstrating that the deviation is far beyond the uncertainty in experimental data. The uncertainty is computed by calculating the standard deviation of both amplitude and phase data for multiple runs and multiple locations on a sample.

From these plots, it is clear that neither of the models is capable of explaining the data, and it is also clear that TDTR data depends on the spectral profile of the transmission coefficients. As can be seen in Fig. 5.5, the coefficients we obtain by solving the inverse problem described in Section 5.4 clearly give a superior fit to the measured data for all modulation frequencies for which measurements were performed.

A better comparison for our measurements is with atomistic calculations that are not subject to the highly restrictive assumptions of the AMM and DMM. Performing this comparison, we observe that our measurements agree with numerous molecular dynamics and atomistic Green's function calculations, essentially all of which predict a decreasing transmission coefficient with increasing phonon frequency.(*154–157*) In particular, our measurement of near-unity transmission for phonons with frequencies less than approximately 4 THz is consistent with atomistic calculations on acoustically-matched materials.(*155*, *177*) Our result also agrees with the experimental studies of polycrystalline silicon by Wang *et al*,(*62*) which suggested that transmission coefficient should decrease with increasing frequency. Our work is thus able to provide unambiguous experimental confirmation of these prior computational and experimental works for the first time while clearly showing that the coefficients predicted by simple models are qualitatively incorrect.

5.7 Interfacial heat flux

Using this transmission coefficient profile, we plot the spectral interfacial heat flux versus phonon frequency and accumulative heat flux versus phonon wavelength in Figs. 5.10. Our results show that most of interfacial heat flux is carried by phonons with frequencies less than 4 THz, with the contribution from higher frequencies strongly reduced due to their small transmission coefficients. In fact, we find that the contribution of phonons with frequencies less than 4 THz is essential to explain our observations: we are unable to explain the measured data without the contribution of phonons with frequencies less than 4 THz. Similarly, we find that we can only explain the measurements using the exact phonon dispersion for Al computed from DFT; simple dispersion relations such as Debye model cannot explain the data because they underestimate the contribution of low frequency phonons to thermal transport.

5.8 Robustness of the measured transmission coefficients

To confirm the robustness of the measured transmission coefficients, we conducted several additional experiments. First, since the energy transmission at the interfaces is considered elastic, the transmission coefficients in theory should be independent of temperature. We performed TDTR measurements on the same Al/Si sample at several temperatures higher than 300 K and compared the experimental results with the calculations using the same transmission coefficient profile measured at 300 K. As shown in Figs. 5.11, the calculation is in excellent agreement with experimental data at 400 K using exactly the same transmission coefficient profile obtained at 300

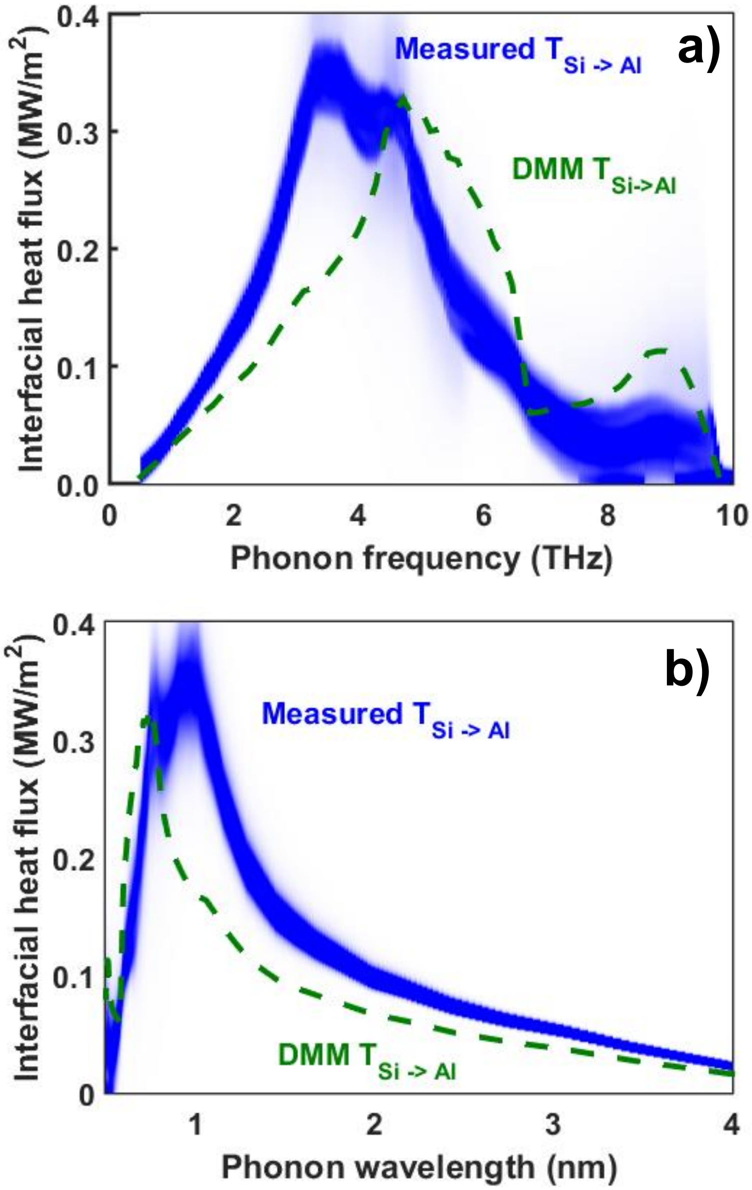

Figure 5.10: Spectral heat flux with the measured (blue shaded region) and DMM (green dashed line) transmission coefficient profiles across the interface versus (a) phonon frequency and (b) phonon wavelength. Phonons with frequencies less than approximately 4 THz carry a significant amount of heat across the interface. The intensity of the shaded region reflects the likelihood of the corresponding transmission coefficients.

K. Note that this comparison does not require any adjustable parameters. Additional measurements at various temperatures are given in the Supplementary Information, and all give excellent agreement.

Second, we measured the transmission coefficients for Al on SiGe. While this material has an additional point defect scattering mechanism compared to pure Si, we expect the transmission coefficients to be nearly the same given that the host lattice is unchanged. The details about point defect scattering in SiGe are given in Appendix D.5. Fig. 5.12 plots the amplitude and phase of the surface temperature decays at different modulation frequencies, demonstrating that the same transmission coefficient profile shown in Fig. 5.6(a) yields a signal that agrees well with this independent data set, again without any adjustable parameters. This result confirms that the measured transmission coefficients for Si and SiGe substrates are indeed the same.

5.9 Effects of atomic structures

We next seek to determine how the atomic structure of the interface affects the spectral content of the phonons carrying heat across the interface. We conducted additional measurements for Al on Si with a native oxide layer (thickness $\sim$ 1 nm as shown in a TEM image in Fig. 5.13(a)) and Si with thermally grown oxide layer (thickness $\sim$ 3.5 nm as shown in a TEM image in Fig. 5.13(b)). Since the oxide layers are sufficiently thin to neglect their thermal capacitance and we only care about the net transmission across the thin layer, we can treat them as part of the interface(*178*) that modifies the transmission coefficient profile.

By solving the inverse problem with the measurement as in Figs. 5.14 & 5.15 as input, we are able to find the transmission coefficient profiles for these two cases as shown in Figs. 5.16. Compared to a clean interface, the transmission coefficients for Al on Si with a native oxide are reduced for most of the phonon modes, except those

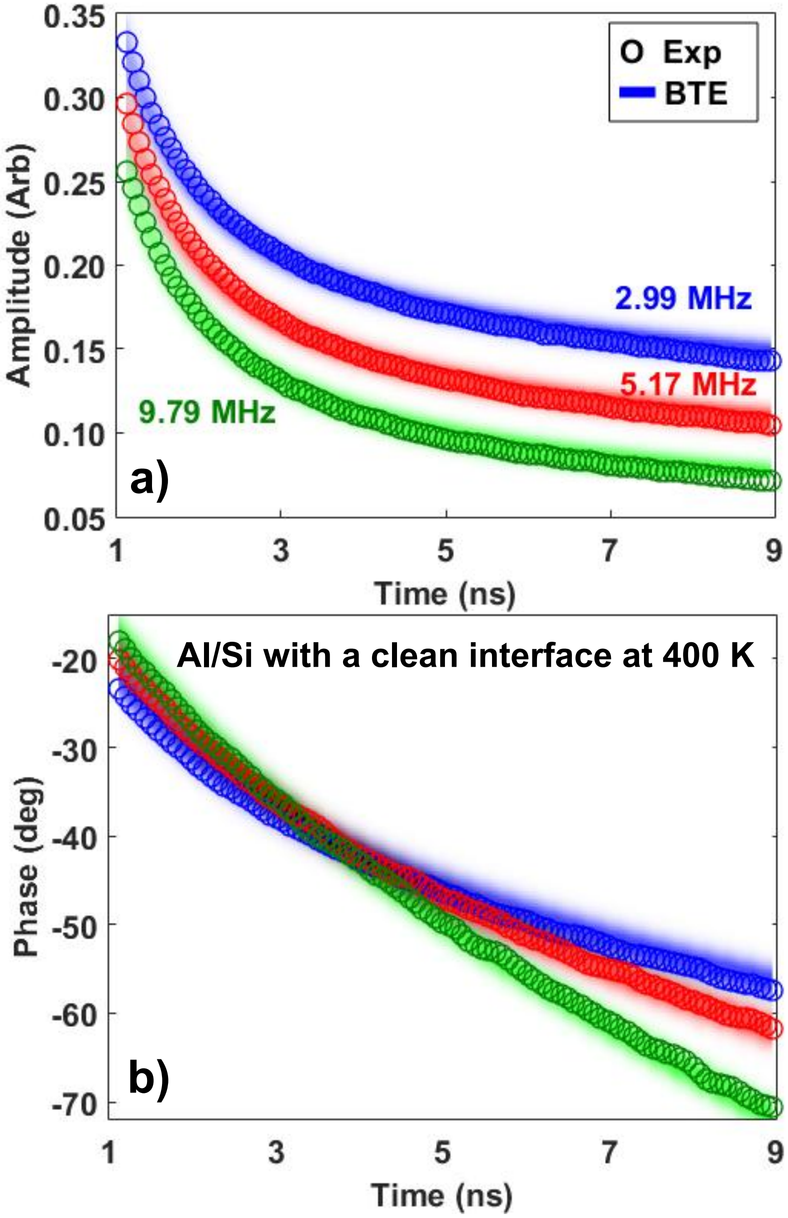

Figure 5.11: (a) Amplitude and (b) phase as a function of time at modulation frequencies $f = 2.99$, 5.17 and 9.79 MHz from experiments (symbols) and simulations (shaded regions) for Al on Si with a clean interface at 400 K. The magnitude and trend of the experimental data are reproduced using the same transmission coefficient profile as in Fig. 5.6 without any adjustable parameters.

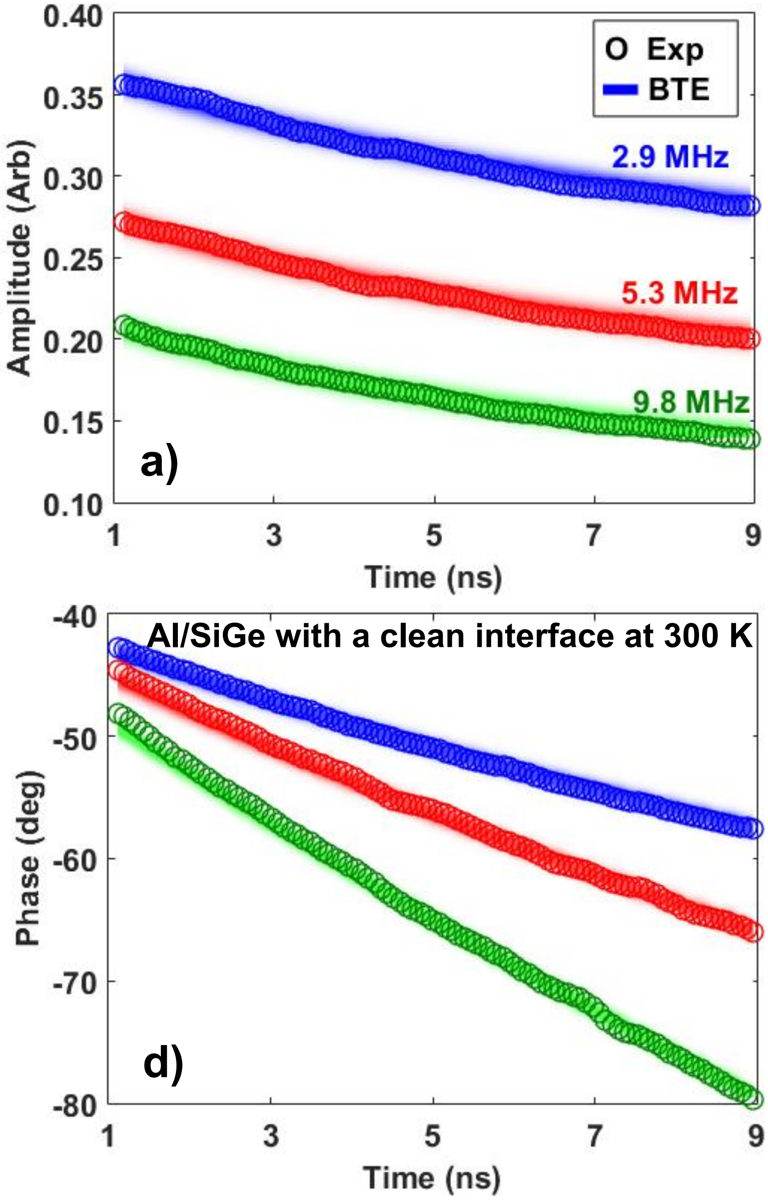

Figure 5.12: (a) Amplitude and (b) phase as a function of time at modulation frequencies $f = 2.9$, 5.3 and 9.8 MHz from experiments (symbols) and simulations (shaded regions) for Al on SiGe with a clean interface at 300 K. The magnitude and trend of the experimental data are reproduced using the same transmission coefficient profile as in Fig. 5.6 without any adjustable parameters.

with long wavelength longer than 1 nm. When the roughness of the interface increases with a thicker oxide layer, the transmission coefficient keeps decreasing and more phonons, especially those with wavelengths between 1 and 3 nm, are reflected at the interface. Therefore, our measurements show that phonons with wavelength shorter than the interface roughness are more likely to be reflected by the interface than phonons with wavelength longer than the interface roughness, and as the interface gets rougher, a larger fraction of the phonon spectrum is affected by the interface. In contrast to prior approaches that measure only interface conductance, here we are able to precisely and unambiguously identify which phonons are more likely to be reflected due to atomic-scale changes in the interface structure for the first time.

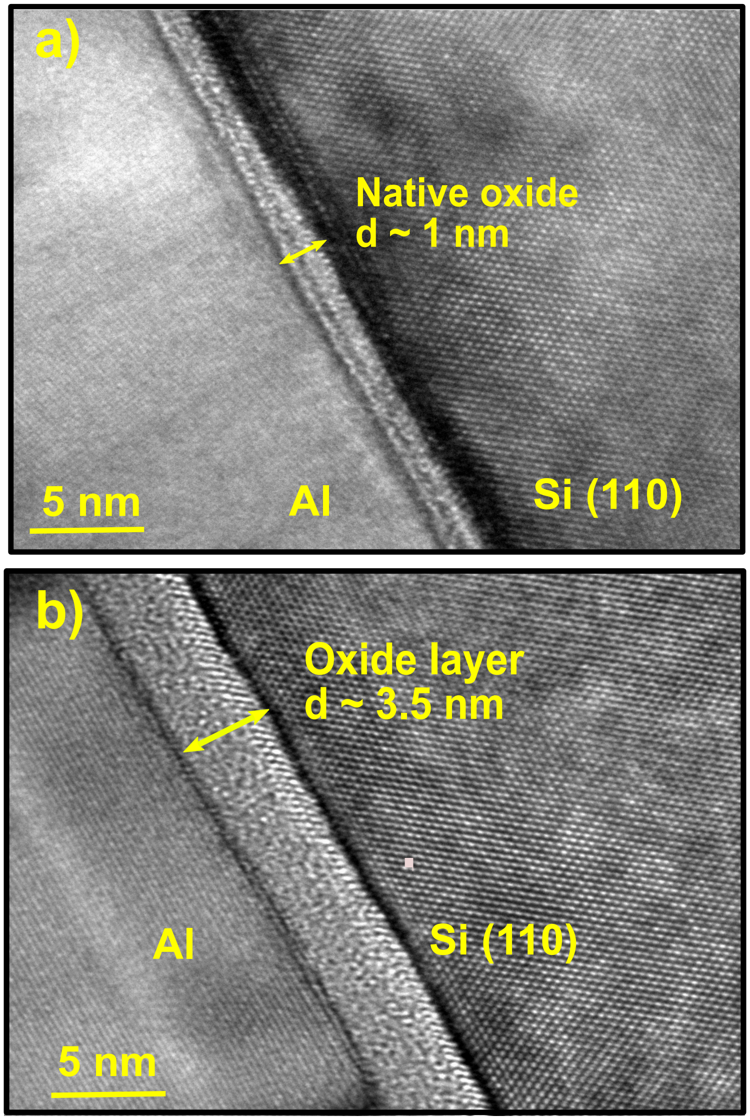

Figure 5.13: TEM images showing the Al/Si sample with (a) native oxide layer (thickness ~ 1 nm) and (b) thermally grown oxide layer (thickness ~ 3.5 nm).

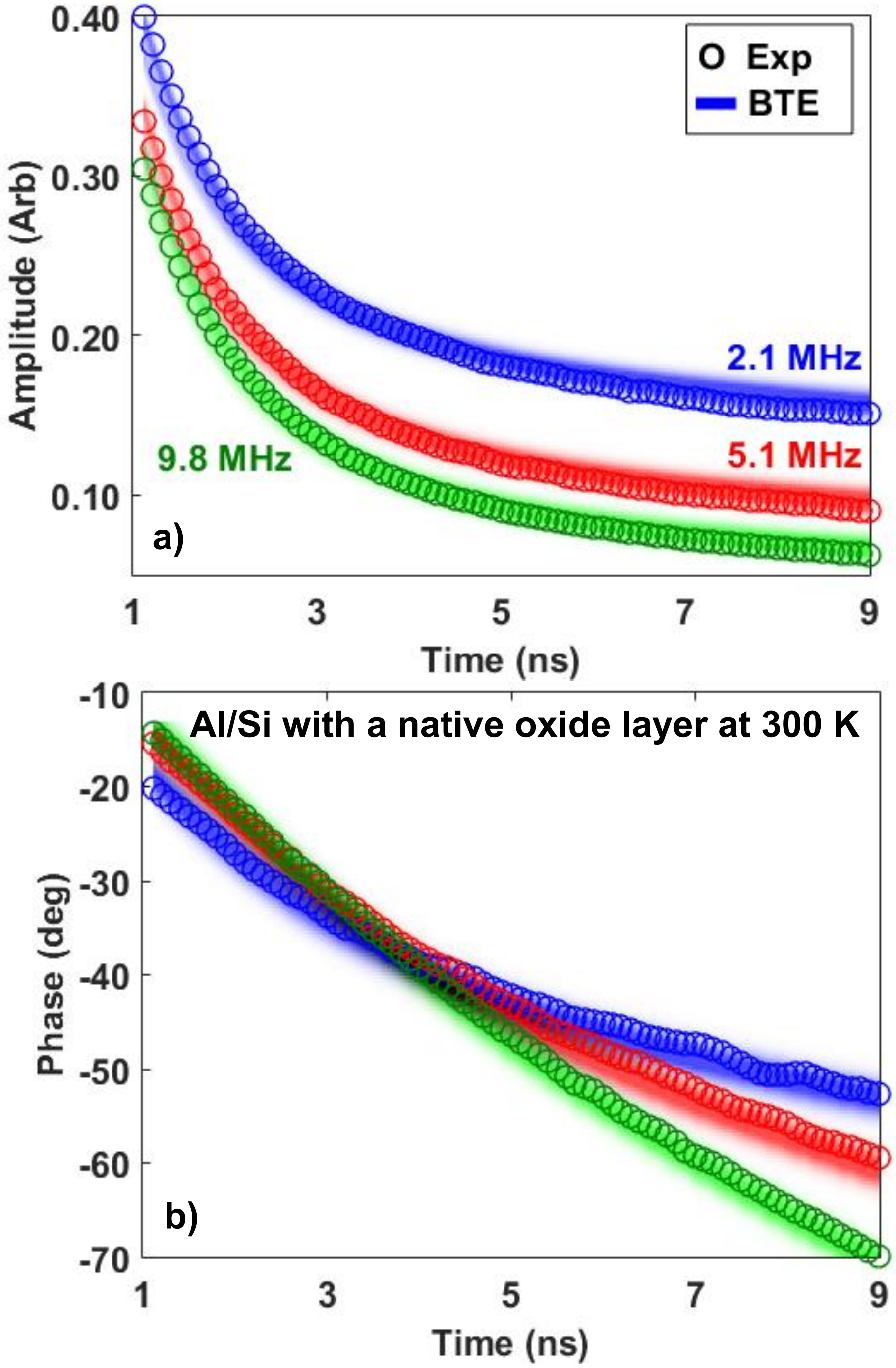

Figure 5.14: (a) Amplitude and (b) phase of the surface temperature decay curves at modulation frequencies $f = 1.43$, 5.10, and 9.80 MHz of experiments (symbols) and simulations (shaded regions) for Al on Si with native oxide layer.

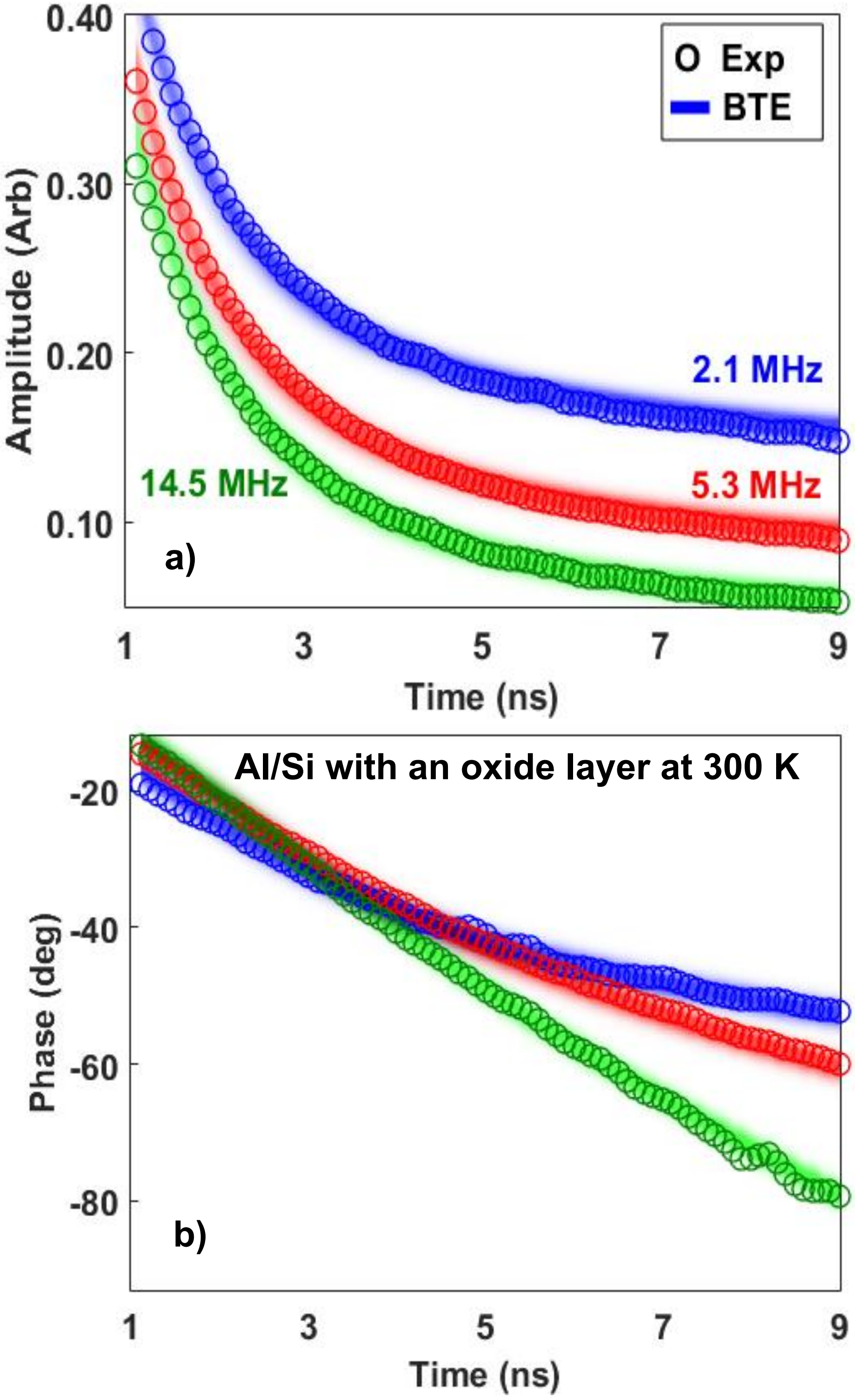

Figure 5.15: (a) Amplitude and (b) phase of the surface temperature decay curves at modulation frequencies f = 1.43, 5.10, and 9.80 MHz of experiments (symbols) and simulations (shaded regions) for Al on Si with a thermally grown oxide layer.

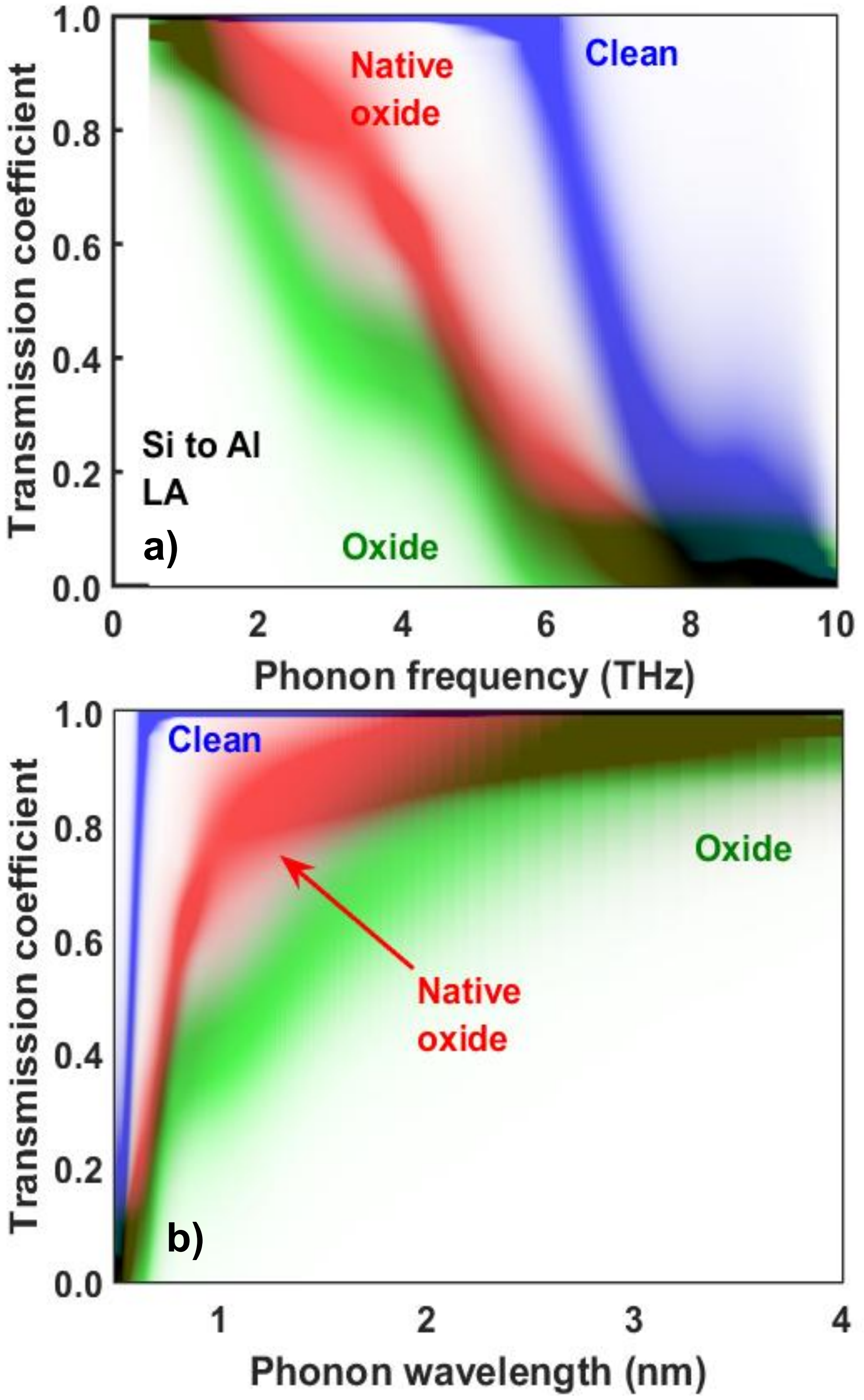

Figure 5.16: Transmission coefficient profiles versus (a) phonon frequency and (b) phonon wavelength for longitudinal modes from Si to Al with a clean interface, with a native oxide layer and with a thermally grown oxide layer. As the interface gets rougher, phonons with frequencies less than 6 THz are more likely to be reflected.

5.10 Role of electrons

The response of a metal to an intense, ultrashort laser pulse is a complex event involving physics that span transport regimes from femtoseconds to microseconds and longer. Initially, photons are absorbed over the duration of the laser pulse by a subset of free electrons in the metal. The hot electrons then interact with the lattice through scattering events.(*179*) To determine the contribution to energy transport from the electrons in Al thin film, we perform the simulations based on a two-temperature model that is able to account for the effects of electrons. Briefly, the two temperature model uses spectral phonon BTE described in Sec. 5.3 coupled with a heat diffusion equation that describes the temperature evolution of the electrons in the Al thin films after absorption of an optical femtosecond laser pulse. The coupled equations are given as following:

$$C_{el}\frac{\partial T_{el}}{\partial t} = \frac{\partial}{\partial x}\left(k_{el}\frac{\partial T_{el}}{\partial x}\right) - g(T_{el} - T_{ph}) \tag{5.32}$$

$$\frac{\partial g_\omega}{\partial t} + \mu v_\omega \frac{\partial_\omega}{\partial x} = -\frac{g_\omega + f_0(T_0) - f_0(T_{ph})}{\tau_\omega} + g(T_{el} - T_{ph}) + \frac{Q_\omega(x,t)}{4\pi}, \tag{5.33}$$

where T_{el} and T_{ph} are the temperatures of the electrons and phonons, respectively, and C_{el} and k_{el} are the volumetric heat capacity and the thermal conductivity of the electrons in Al, respectively. The phonon temperature is linearly coupled to the electron temperature through the electron-phonon coupling coefficient g. The values of all the constants in Eq. 5.32 are tabulated in Table D.1. This system of the equations is solved by a standard finite difference method in a two layered geometry.

We compare the surface temperature responses to a heat impulse with and without the effects of electrons. As shown in Fig. 5.17, due to strong electron-phonon coupling, electrons only affect the heat conduction shortly after the absorption of a heat pulse. After the first 100 ps, the heat conduction is dominated by the phonons. Since a typical signal in a TDTR experiment is usually measured after 500 ps, whether

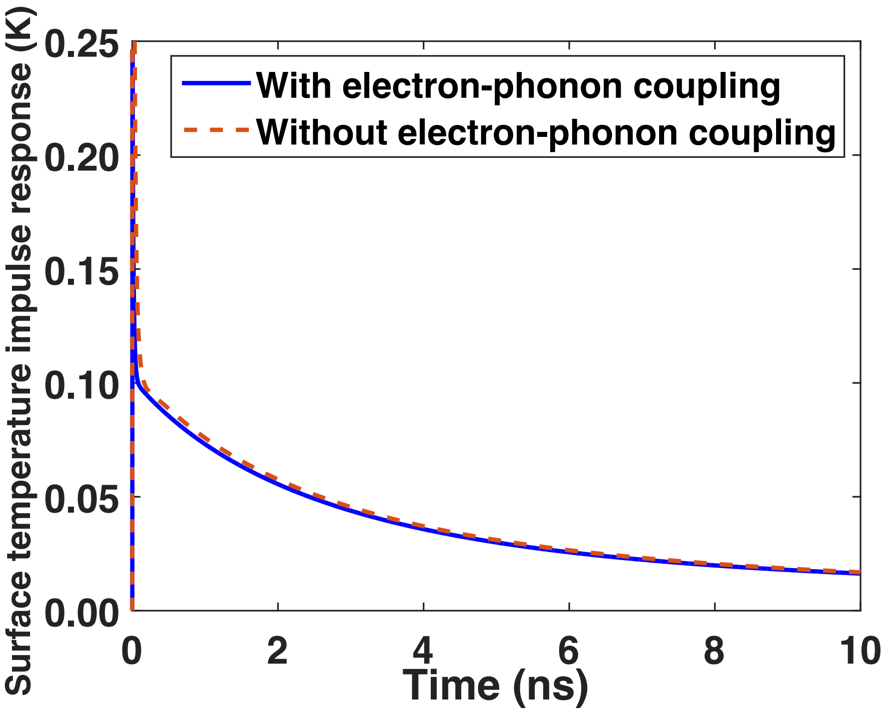

Figure 5.17: The surface temperature decay subject to an surface impulse heating for Al on Si with (solid blue line) and without (dashed red line) the effects of electrons. After 100 ps, the heat is dominated by phonons and there is little contribution from the electrons. Therefore, the electrons have negligible effects on the signal on the timescale relevant to the heat conduction across interfaces.

heat is attributed to phonons or electrons in the metal has a negligible effect on the signal on the timescales that is interested in the experiments. Therefore, our neglect of electrons has no effect on our transmission coefficient measurement.

5.11 Effects of mode conversion

When phonons cross an interface they can change their frequency, in an inelastic process, or polarization, known as mode conversion, which can influence thermal interface conductance.(*180*) In our work, we do not consider inelastic scattering. We justify the neglect of inelastic scattering through the work of prior numerical studies, which have provide evidence that the phonon transmission between two slightly dissimilar crystalline solids is elastic.(*181*) Considering the phonon frequencies between Al and Si are very similar, there is no evidence that inelastic processes should play a role in the interfacial transport for Al/Si interfaces.

We have carefully examined the effect of mode conversion on our conclusions by rigorously including this process in our BTE model. To examine whether conversion between polarizations would affect the phonon transport across the interface, we conducted our BTE simulation assuming modes maintain their polarization after crossing the interface, or allowing them to change to any polarization while keeping the total transmission coefficient the same. Keeping the total transmission coefficient for a given polarization. Keeping $\sum_j T_{12}^{ij}(\omega)$ invariant, we randomly partitioned $\sum_j T_{12}^{ij}(\omega)$, $\sum_j R_{12}^{ij}(\omega)$ and $\sum_j R_{21}^{ij}(\omega)$ into two different combinations of $T_{12}^{ij}(\omega)$, $R_{12}^{ij}(\omega)$ and $R_{21}^{ij}(\omega)$;in other words, randomly between all the polarizations on the opposite side of the interface. In Fig. 5.18, we show that the surface temperature decay with and without conversion between polarization are essentially identical. Moreover, the spectral interfacial heat flux is also identical with and without conversion. Therefore, we conclude that mode conversion does not have an observable effect on the signal.

The reason that our measurement is not sensitive to mode conversion is that the polarizations in Si do not have extremely dissimilar mean free paths. As our measurement approach relies on the lack of scattering of some modes near the interface, the only way the mode conversion could affect our measurements would be if one polarization consistently changed to another polarization after transmitting through the interface with a drastically different mean free path than the original polarization. Our calculations clearly show that the difference in mean free paths between the polarizations is not sufficient to affect our calculations and hence have any effect on our conclusions.

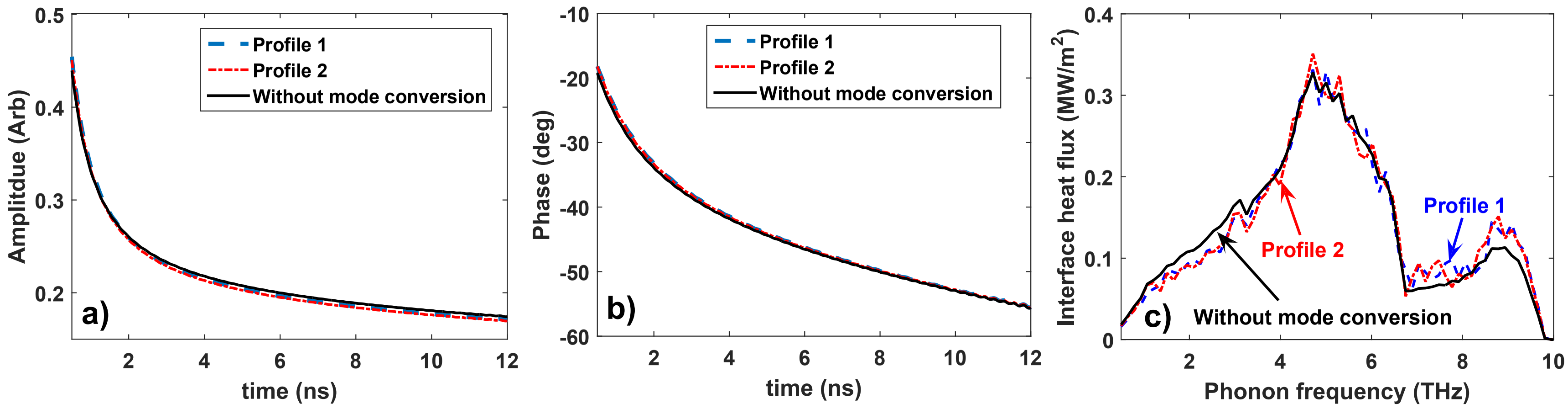

Figure 5.18: TDTR surface temperature decay curves along with (a) amplitude and (c) phase using different transmission coefficient profiles with two completely random partitions of transmitting modes to different polarizations (dashed and dash-dotted lines) and without mode conversion (solid line; assuming phonons maintain their polarization as they cross the interface). (c) Spectral interfacial heat flux versus phonon frequency predicted using different transmission coefficient profiles with mode conversion (dashed and dash-dotted lines) and without mode conversion. Mode conversion does not have an effect on the signal and conclusions beyond the uncertainties already considered in our model.

5.12 Discussion

Our work has considerable implications for thermal metrology and technological applications. First, we have shown that TDTR is capable of providing considerable microscopic detail about thermal phonons if the measurements can be properly interpreted using a microscopic transfer function with ab-initio input. Unlike with the macroscopic transfer function, our approach provides quantitative details on the spectral content of the heat carried by phonons in the sample. As a corollary, using the macroscopic transfer function to interpret TDTR data on certain samples can lead to erroneous results. For example, the apparently correct measurement of silicon thermal conductivity appears to be a fortuitous cancellation of two factors: the high transmission coefficient of low frequency phonons leads to an increased contribution to heat flux that offsets the deviation from Fourier's law that occurs due to a lack of scattering. If these two factors were not balanced, the apparent thermal conductivity of Si would not coincide with the bulk value. Therefore, the conventional TDTR interpretation does not necessarily provide the actual physical properties of the materials.

Second, our measurements show that the spectral profile of transmission coefficients is essential to understanding thermal transport across interfaces. Due to a lack of knowledge about interfaces, the phonon transmission coefficients are often predicted with a variety of simple models. However, this work shows that none of these models are capable of explaining the experimental measurements. Therefore, including an accurate spectral transmission coefficient profile is essential to properly describing thermal phonon transport across interfaces.

Third, our work provides strong evidence that elastic transmission of phonons across an interface is the dominant energy transmission mechanism for materials with similar phonon frequencies. Our microscopic transfer function does not incorporate electrons or inelastic scattering yet is able to explain all of the measurements we performed. We conclude that inelastic transmission and coupling between electrons in metals and phonons in semiconductors have little influence on the energy transport for the materials considered here.

Fourth, our results demonstrate that disorder at interfaces plays an important role in the spectral content of the heat transmitted through the interface and provides strategies to alter interface conductance. For instance, in applications like LEDs where the heat dissipation rate across interfaces is to be enhanced, the key to increasing interface conductance is to minimize the reflection of high frequency phonons (with wavelength shorter than the surface roughness of the interface) by reducing defects; low frequency phonons (with wavelength longer than the surface roughness of the interface) are likely to be mostly transmitted already. On the other hand, the strong frequency dependence of the transmission coefficients can be exploited to create thermal phonon filters to selectively remove parts of phonon spectrum, analogous to optical long-pass filters. Phonons with wavelength much longer than the characteristic roughness of an interface are more likely transmitted through the interface while short-wavelength phonons are mostly reflected. The thermal phonon spectrum responsible for heat conduction can thus be manipulated by controlling the atomistic roughness of an interface.

Finally, our work exemplifies the powerful insights into heat conduction at the atomic scale that can be obtained through the interwoven application of experimental measurements in the quasiballistic heat conduction regime, ab-initio phonon transport modeling, and electron microscopy. Through our approach, we are able to directly link the atomic structure of an interface to the spectral content of heat crossing it for the first time. Such a capability will permit the rational understanding and control of interfacial heat transport at the atomic level, a capability that is expected to impact numerous application.

Chapter 6

CONCLUSIONS AND OUTLOOK

6.1 Summary

Precise control of thermal phonons, which are the primary heat carriers in solids, is a fascinating and rapidly growing field which could make substantial contributions to greatly expand the range of performance of existing materials and devices as well as innovate new materials and device designs. Interfaces play an essential role in phonon-mediated heat conduction in solids. The ability to manipulate thermal phonons using interfaces could impact applications ranging from thermoelectric waste heat recovery to heat dissipation in electronics. Despite the importance of interfaces and decades of work, interfacial thermal phonon transport remains one of the most poorly understood transport processes. This thesis has explored the physics of interfacial heat transport by phonons, and helped identify how we are able to use atomic structures to control phonon transport in solids. Using a combination of modeling and experiment we are able to better understand phonon transport across interfaces, and we introduce a new approach by which the microscopic properties of thermal phonons can be extracted from thermal measurements.

Chapter 2 has studied the impact of frequency-dependent grain boundary scattering in nanocrystalline silicon and silicon germanium alloys using a novel frequency-dependent variance-reduced Monte Carlo technique. This method allows us to simulate the thermal phonon transport in a realistic 3D geometry of a complex nanograin structure. We find that the grain boundary may not be as effective as predicted by the commonly used gray model in scattering certain phonons, with a substantial amount of heat being carried by low frequency phonons with mean free paths (MFPs) longer than the grain size. Significant potential to improve the efficiency of nanocrystalline silicon and silicon germanium exists if these phonons can be scattered. Our work provides important insight into how to further increase the thermoelectric performance of nanostructured silicon and silicon-germanium alloys.

The rest of the thesis focuses on how to measure microscopic properties of thermal phonons directly from experimental measurements. In Chapter 3, we have presented two new analytical methods to solve the frequency-dependent, multidimensional Boltzmann transport equation (BTE) under relaxation time approximation that enables simple, closed-form solutions to complex problems that have been tractable previously only using computational expensive simulations. Our new solutions are valid from diffusive to ballistic transport regimes, rigorously including frequency-dependence of phonon properties, and can be applied to complex geometries.

Chapter 4 has applied the analytical methods to study the heat conduction in transient grating (TG) spectroscopy, which has been of intense interest recently because of the possibility of measure MFP spectra using observations of quasiballistic heat conduction. The derived analytical solution provides a more rigorous mathematical formulation to interpret the TG measurement and therefore enables MFP spectra to be measured more accurately.

In Chapter 5, we have reported the first measurement of the transmission coefficients for thermal phonons at a metal-semiconductor interface. Our approach exploits the advances in ab-initio thermal phonon transport modeling we present in Chapter 3 to directly extract the coefficients from the data of an optical thermal experiment for the first time. With our approach, we are able to directly link the atomic structure of an interface to the spectral content of the heat crossing it for the first time. Our measurements reveal that phonons with wavelength shorter than the interface roughness are more likely to be reflected by the interface than phonons with wavelength longer than the interface roughness, and as the interface gets rougher, a larger fraction of the phonon spectrum is affected by the interface. In contrast to prior approaches that measure only interface conductance, here we are able to precisely and unambiguously identify which phonons are more likely to be reflected due to atomic-scale changes in the interface structure for the first time. Our work also demonstrates a general approach by which the microscopic properties of thermal phonons can be extracted from thermal measurements, and thus sets the stage for additional seminal measurements.

6.2 Future work

One important conclusion of this thesis is that the combination of ab-initio transport modeling and ultrafast optical techniques could yield tremendous microscopic information about thermal phonons that is not previously accessible only through ultrafast experiments. In a sense, then, the work presented here is only the beginning because it demonstrates a general route by which the microscopic processes of thermal phonon transport can be studied from thermal measurements. With this approach, many other transport processes such as phonon scattering by defects and electron-phonon coupling in semiconductors can be explored.

The future work consists of measuring transmission coefficients for increasingly complex materials. The simplest next step would be to perform similar transmission coefficient measurements at other metal-silicon interfaces for different types of interfaces, *i.e.* atomically smooth or textured interfaces. Then, the method can be extended to study more complicated interface geometries, *i.e.* grain boundaries or superlattices.

Half-Heusler compounds have been attractive thermoelectric materials because they are usually environmentally friendly, mechanically, and thermally robust. However, their high thermal conductivity has impeded the progress of making them commercially viable. Nanostructured Half-Heusler thermoelectrics has been demonstrated with an improved efficiency. This improvement again is attributed to a reduction in thermal conductivity by grain boundary scattering of phonons as nanocrystalline silicon and silicon-germanium discussed in Chapter 1. However, the microscopic properties of Half-Heusler such as phonon MFPs is still unclear. A systematic study on the microscopic transport processes occurring in nanostructured Half-Heuslers is necessary to further improve their efficiency as thermoelectrics. For future work, one can use the method described in Chapter 4 to measure the MFP spectra in both bulk and nanocrystalline Half-Heusler compounds. By comparing the two spectra, one can get a microscopic quantitative picture of how specific phonons are affected by the grain boundaries. The mode-specific phonon transmission coefficients can be recovered by fitting the BTE-simulated MFP spectrum to the measurements. The variance reduced Monte Carlo algorithm introduced in Chapter 2 could be used to simulate the thermal transport. Rather than a simple 3D grain structure used in this work, one could extend the simple structure to the real structures as characterized by the transmission electron microscopy.

Superlattices, a periodic structure of layers of two or more, are another materials of great interests though little is known about microscopic phonon transport processes in them. A similar study on the interfacial heat transport as done in Chapter 5 could be carried out after one extends the two-layer BTE solution to include multiple layers.

Next, more attention is worth drawing to further explore the energy transport in the transition regime between ballistic and diffusive propagation. This regime holds valuable information on the nature of energy carriers in solids. Our work has identified two sub categories within this transition regime, demonstrating that this transition regime might be more complicated than previously understood. Other recent work(*182*) has demonstrated that there might be another new regime where heat dissipation efficiency could be enhanced even when characteristic length are much smaller than the energy carriers' MFPs. A comprehensive picture of nanoscale energy transport is not only necessary but also crucial to achieve precise control of heat in solids.

Besides phonons, electrons also play a crucial role in energy transport in metals and semiconductors. Electron and phonon coupling is ubiquitous in condensed matter. Electron scattering by phonons is one of the major processes which determines the transport characteristics in metals and semiconductors. With the advance in first-principle calculations, it is now possible to get the spectral properties of electrons in both metal and semiconductor-based materials, which provides inputs for electron transport modeling. As previously done for phonon transport, one can rigorously investigate the electron-phonon interaction in semiconductor/metal-based materials using the combination of ab-initio transport modeling and ultrafast optical techniques done previously for phonon transport.

These are just a few of the possibilities which could yield important and useful information about nanoscale energy transport. Energy manipulation at the nanoscale is at the forefront of modern technological innovation, and our understanding of energy transport at this scale would lead to more robust and efficient methods of designing frontier materials and devices. We hope this thesis has given insights into microscopic processes of energy carriers in solids and will be useful for achieving our ultimate goal of energy manipulation.

BIBLIOGRAPHY

(*1*) J. P. Dismukes et al. “Thermal and Electrical Properties of Heavily Doped GeSi Alloys up to 1300 K”. In: *Journal of Applied Physics* 35.10 (1964).

(*2*) D. M. Rowe, V. S. Shukla, and N. Savvides. “Phonon scattering at grain boundaries in heavily doped fine-grained silicon-germanium alloys”. In: *Nature* 290.5809 (1981), pp. 765–766.

(*3*) Giri Joshi et al. “Enhanced Thermoelectric Figure-of-Merit in Nanostructured p-type Silicon Germanium Bulk Alloys”. In: *Nano Letters* 8.12 (2008), pp. 4670–4674.

(*4*) X. W. Wang et al. “Enhanced thermoelectric figure of merit in nanostructured n-type silicon germanium bulk alloy”. In: *Applied Physics Letters* 93.19, 193121 (2008), pp. –. DOI: `http://dx.doi.org/10.1063/1.3027060`. URL: `http://scitation.aip.org/content/aip/journal/apl/93/19/10.1063/1.3027060`.

(*5*) G. H. Zhu et al. “Increased Phonon Scattering by Nanograins and Point Defects in Nanostructured Silicon with a Low Concentration of Germanium”. In: *Phys. Rev. Lett.* 102 (19 2009), p. 196803. DOI: `10.1103/PhysRevLett.102.196803`. URL: `http://link.aps.org/doi/10.1103/PhysRevLett.102.196803`.

(*6*) Sabah K. Bux et al. “Nanostructured Bulk Silicon as an Effective Thermoelectric Material”. In: *Advanced Functional Materials* 19.15 (2009), pp. 2445–2452. ISSN: 1616-3028. DOI: `10.1002/adfm.200900250`. URL: `http://dx.doi.org/10.1002/adfm.200900250`.

(*7*) A. J. Minnich. “Phonon heat conduction in layered anisotropic crystals”. In: *Phys. Rev. B* 91 (8 2015), p. 085206. DOI: `10.1103/PhysRevB.91.085206`. URL: `http://link.aps.org/doi/10.1103/PhysRevB.91.085206`.

(*8*) Zhong Yan et al. “Graphene quilts for thermal management of high power GaN transistors”. In: *Nature Communications* 3.827 (2012). DOI: `10.1038/ncomms1828`.

(*9*) Bed Poudel et al. “High-Thermoelectric Performance of Nanostructured Bismuth Antimony Telluride Bulk Alloys”. In: *Science* 320.5876 (2008), pp. 634–638.

(*10*) Rutvik J. Mehta et al. “A new class of doped nanobulk high-figure-of-merit thermoelectrics by scalable bottom-up assembly”. In: *Nat Mater* 11 (2012), 233–240s. DOI: `10.1038/nmat3213`.

(*11*) K. Biswas et al. “Strained endotaxial nanostructures with high thermoelectric figure of merit”. In: *Nature Chemistry* 3 (2011), pp. 160–166. DOI: `10.1038/nchem.955`.

(*12*) K. Biswas et al. “High-performance bulk thermoelectrics with all-scale hierarchical architectures”. In: *Nature* 489 (2012), pp. 414–418. DOI: `10.1038/nature11439`.

(*13*) C. Dames and G. Chen. “Thermal conductivity of nanostructured thermoelectric materials”. In: *Thermoelectrics Handbook: Macro to Nano* Chapter 42, CRC Press, ed. D. Rowe (2005).

(*14*) A. J. Minnich et al. “Bulk nanostructured thermoelectric materials: current research and future prospects”. In: *Energy Environ. Sci.* 2 (5 2009), pp. 466–479. DOI: `10.1039/B822664B`. URL: `http://dx.doi.org/10.1039/B822664B`.

(*15*) Conyers Herring. “Role of Low-Energy Phonons in Thermal Conduction”. In: *Phys. Rev.* 95 (4 1954), pp. 954–965. DOI: `10.1103/PhysRev.95.954`. URL: `http://link.aps.org/doi/10.1103/PhysRev.95.954`.

(*16*) C. Thomsen et al. “Surface generation and detection of phonons by picosecond light pulses”. In: *Phys. Rev. B* 34 (6 1986), pp. 4129–4138. DOI: `10.1103/PhysRevB.34.4129`. URL: `http://link.aps.org/doi/10.1103/PhysRevB.34.4129`.

(*17*) O. Delaire et al. “Giant anharmonic phonon scattering in PbTe”. In: *Nat Mater* advance online publication (June 2011).

(*18*) R. J. von Gutfeld and A. H. Nethercot. “Heat Pulses in Quartz and Sapphire at Low Temperatures”. In: *Phys. Rev. Lett.* 12.23 (1964), pp. 641–644.

(*19*) M. Highland et al. “Ballistic-phonon heat conduction at the nanoscale as revealed by time-resolved x-ray diffraction and time-domain thermoreflectance”. In: *Phys. Rev. B* 76 (7 2007), p. 075337. DOI: `10.1103/PhysRevB.76.075337`. URL: `http://link.aps.org/doi/10.1103/PhysRevB.76.075337`.

(*20*) A. J. Minnich et al. “Thermal Conductivity Spectroscopy Technique to Measure Phonon Mean Free Paths”. In: *Phys. Rev. Lett.* 107 (9 2011), p. 095901. DOI: `10.1103/PhysRevLett.107.095901`. URL: `http://link.aps.org/doi/10.1103/PhysRevLett.107.095901`.

(*21*) Gang Chen. *Nanoscale Energy Transport and Conversion*. New York: Oxford University Press, 2005.

(*22*) A. Majumdar. “Microscale heat conduction in dielectric thin-films”. In: *J. heat transfer* 115 (1 1993), pp. 7–16.

(*23*) Mark E. Siemens et al. “Quasi-ballistic thermal transport from nanoscale interfaces observed using ultrafast coherent soft X-ray beams”. In: *Nat. Mater.* 9 (1 2010), pp. 26–30. DOI: `http://dx.doi.org/10.1038/nmat2568`.

(*24*) Keith T. Regner et al. "Broadband phonon mean free path contributions to thermal conductivity measured using frequency domain thermoreflectance". In: *Nat. Commum.* 4.1640 (2013).

(*25*) Jeremy A. Johnson et al. "Direct Measurement of Room-Temperature Nondiffusive Thermal Transport Over Micron Distances in a Silicon Membrane". In: *Phys. Rev. Lett.* 110 (2 2013), p. 025901. DOI: `10.1103/PhysRevLett.110.025901`. URL: `http://link.aps.org/doi/10.1103/PhysRevLett.110.025901`.

(*26*) Ho-Ki Lyeo and David G. Cahill. "Thermal conductance of interfaces between highly dissimilar materials". In: *Phys. Rev. B* 73 (14 2006), p. 144301. DOI: `10.1103/PhysRevB.73.144301`. URL: `http://link.aps.org/doi/10.1103/PhysRevB.73.144301`.

(*27*) P. M. Norris and P. E. Hopkins. "Examining interfacial diffuse phonon scattering through transient thermoreflectance measurements of thermal boundary conductance". In: *Journal of Heat Transfer* 131 (4 2009), p. 043207. DOI: `10.1115/1.3072928`.

(*28*) Ramez Cheaito et al. "Thermal boundary conductance accumulation and interfacial phonon transmission: Measurements and theory". In: *Phys. Rev. B* 91 (3 2015), p. 035432. DOI: `10.1103/PhysRevB.91.035432`. URL: `http://link.aps.org/doi/10.1103/PhysRevB.91.035432`.

(*29*) Aaron J. Schmidt et al. "Thermal conductance and phonon transmissivity of metal–graphite interfaces". In: *Journal of Applied Physics* 107.10, 104907 (2010), p. 104907. DOI: `http://dx.doi.org/10.1063/1.3428464`. URL: `http://scitation.aip.org/content/aip/journal/jap/107/10/10.1063/1.3428464`.

(*30*) John C. Duda et al. "Role of dispersion on phononic thermal boundary conductance". en. In: *Journal of Applied Physics* 108.7 (2010), p. 073515. ISSN: 00218979. DOI: `10.1063/1.3483943`. URL: `http://scitation.aip.org/content/aip/journal/jap/108/7/10.1063/1.3483943` (visited on 06/24/2015).

(*31*) Peter J. O'Brien et al. "Bonding-induced thermal conductance enhancement at inorganic heterointerfaces using nanomolecular monolayers". en. In: *Nature Materials* (2012). ISSN: 1476-1122. DOI: `10.1038/nmat3465`. URL: `http://www.nature.com.clsproxy.library.caltech.edu/nmat/journal/vaop/ncurrent/full/nmat3465.html` (visited on 11/18/2012).

(*32*) M. D. Losego et al. "Effects of chemical bonding on heat transport across interfaces". In: *Nature Materials* 11 (6 2012), pp. 502–506. DOI: `10.1038/NMAT3303`.

(*33*) David G. Cahill et al. “Nanoscale thermal transport. II. 2003–2012”. In: *Applied Physics Reviews* 1.1 (Jan. 2014), p. 011305. ISSN: 1931-9401. DOI: `10.1063/1.4832615`. URL: `http://scitation.aip.org/content/aip/journal/apr2/1/1/10.1063/1.4832615` (visited on 01/18/2014).

(*34*) Eric Pop. “Energy dissipation and transport in nanoscale devices”. In: *Nano Research* 3.3 (May 2010), pp. 147–169.

(*35*) A. Majumdar. “Microscale Heat Conduction in Dielectric Thin Films”. In: *Journal of Heat Transfer* 115.1 (1993), pp. 7–16.

(*36*) Subrahmanyan Chandrasekhar. *Radiative Transfer*. en. Courier Dover Publications, Apr. 1950. ISBN: 9780486318455.

(*37*) K. M. Case. “Elementary solutions of the transport equation and their applications”. In: *Annals of Physics* 9.1 (1960), pp. 1 –23. ISSN: 0003-4916. DOI: `http://dx.doi.org/10.1016/0003-4916(60)90060-9`.

(*38*) C. E. Siewert and P. F. Zweifel. “An exact solution of equations of radiative transfer for Local Thermodynamic Equilibrium in the non-gray case. Picket fence approximation”. In: *Annals of Physics* 36.1 (1966), pp. 61 –85. ISSN: 0003-4916. DOI: `http://dx.doi.org/10.1016/0003-4916(66)90290-9`. URL: `http://www.sciencedirect.com/science/article/pii/0003491666902909`.

(*39*) M. M. R. Williams. “The energy-dependent Milne Problem with a simple scattering kernel”. In: *Nuclear Science and Engineering* 18 (1964), pp. 260–270.

(*40*) G. Chen. “Nonlocal and Nonequilibrium Heat Conduction in the Vicinity of Nanoparticles”. In: *Journal of Heat Transfer* 118.3 (1996), pp. 539–545.

(*41*) Ronggui Yang et al. “Simulation of Nanoscale Multidimensional Transient Heat Conduction Problems Using Ballistic-Diffusive Equations and Phonon Boltzmann Equation”. In: *Journal of Heat Transfer* 127.3 (2005), pp. 298–306. DOI: `10.1115/1.1857941`. URL: `http://link.aip.org/link/?JHR/127/298/1`.

(*42*) Gang Chen. “Ballistic-Diffusive Heat-Conduction Equations”. In: *Phys. Rev. Lett.* 86 (11 2001), pp. 2297–2300. DOI: `10.1103/PhysRevLett.86.2297`. URL: `http://link.aps.org/doi/10.1103/PhysRevLett.86.2297`.

(*43*) J. Ordonez-Miranda, Ronggui Yang, and J. J. Alvarado-Gil. “A constitutive equation for nano-to-macro-scale heat conduction based on the Boltzmann transport equation”. In: *Journal of Applied Physics* 109.8, 084319 (2011), pp. –. DOI: `http://dx.doi.org/10.1063/1.3573512`. URL: `http://scitation.aip.org/content/aip/journal/jap/109/8/10.1063/1.3573512`.

(*44*) Z. Tian, S. Lee, and G. Chen. "Heat transfer in thermoelectric materials and devices". In: *J. Heat Transfer* 135 (6 2013), p. 061605. DOI: `10.1115/1.4023585`.

(*45*) J. P. Heremans et al. "When thermoelectrics reached the nanoscale". In: *Nature Nanotechnology* 8 (2013), pp. 471–473. DOI: `10.1038/nnano.2013.129`.

(*46*) Shannon K. Yee et al. "$ per W metrics for thermoelectric power generation: beyond ZT". In: *Energy Environ. Sci.* 6 (9 2013), pp. 2561–2571. DOI: `10.1039/C3EE41504J`. URL: `http://dx.doi.org/10.1039/C3EE41504J`.

(*47*) Carolina Abs da Cruz et al. "Thermal conductivity of nanocrystalline SiGe alloys using molecular dynamics simulations". In: *Journal of Applied Physics* 114.16, 164310 (2013), pp. –. DOI: `http://dx.doi.org/10.1063/1.4826526`. URL: `http://scitation.aip.org/content/aip/journal/jap/114/16/10.1063/1.4826526`.

(*48*) Claudio Melis and Luciano Colombo. "Lattice Thermal Conductivity of $\mathrm{Si}_{1-x}\mathrm{Ge}_x$ Nanocomposites". In: *Phys. Rev. Lett.* 112 (6 2014), p. 065901. DOI: `10.1103/PhysRevLett.112.065901`. URL: `http://link.aps.org/doi/10.1103/PhysRevLett.112.065901`.

(*49*) Arun Bodapati et al. "Vibrations and thermal transport in nanocrystalline silicon". In: *Phys. Rev. B* 74 (24 2006), p. 245207. DOI: `10.1103/PhysRevB.74.245207`. URL: `http://link.aps.org/doi/10.1103/PhysRevB.74.245207`.

(*50*) P. K. Schelling, S. R. Phillpot, and P. Keblinski. "Phonon wave-packet dynamics at semiconductor interfaces by molecular-dynamics simulation". In: *Applied Physics Letters* 80 (2002), p. 2484. ISSN: 00036951. DOI: `10.1063/1.1465106`. URL: `http://link.aip.org/link/APPLAB/v80/i14/p2484/s1&Agg=doi`.

(*51*) Chris Kimmer et al. "Scattering of phonons from a high-energy grain boundary in silicon: Dependence on angle of incidence". In: *Phys. Rev. B* 75 (14 2007), p. 144105. DOI: `10.1103/PhysRevB.75.144105`. URL: `http://link.aps.org/doi/10.1103/PhysRevB.75.144105`.

(*52*) Hong Zhao and Jonathan B. Freund. "Phonon scattering at a rough interface between two fcc lattices". In: *Journal of Applied Physics* 105.1, 013515 (2009), pp. –. DOI: `http://dx.doi.org/10.1063/1.3054383`. URL: `http://scitation.aip.org/content/aip/journal/jap/105/1/10.1063/1.3054383`.

(*53*) Xiaobo Li and Ronggui Yang. "Effect of lattice mismatch on phonon transmission and interface thermal conductance across dissimilar material interfaces". In: *Phys. Rev. B* 86 (5 2012), p. 054305. DOI: `10.1103/PhysRevB.`

86.054305. URL: `http://link.aps.org/doi/10.1103/PhysRevB.86.054305`.

(*54*) Zhiting Tian, Keivan Esfarjani, and Gang Chen. "Enhancing phonon transmission across a Si/Ge interface by atomic roughness: First-principles study with the Green's function method". In: *Phys. Rev. B* 86 (23 2012), p. 235304. DOI: `10.1103/PhysRevB.86.235304`. URL: `http://link.aps.org/doi/10.1103/PhysRevB.86.235304`.

(*55*) Qing Hao et al. "Theoretical studies on the thermoelectric figure of merit of nanograined bulk silicon". In: *Applied Physics Letters* 97.6, 063109 (2010), pp. –. DOI: `http://dx.doi.org/10.1063/1.3478459`. URL: `http://scitation.aip.org/content/aip/journal/apl/97/6/10.1063/1.3478459`.

(*56*) Qing Hao. "Effective medium formulation for phonon transport analysis of nanograined polycrystals". In: *Journal of Applied Physics* 111.1 (Jan. 2012), pp. 014307–014307–5.

(*57*) Qing Hao. "Influence of structure disorder on the lattice thermal conductivity of polycrystals: A frequency-dependent phonon-transport study". In: *Journal of Applied Physics* 111.1 (Jan. 2012), pp. 014309–014309–4. ISSN: 00218979. DOI: `doi:10.1063/1.3675466`. URL: `http://jap.aip.org/resource/1/japiau/v111/i1/p014309_s1`.

(*58*) Jun Zhou et al. "Semiclassical model for thermoelectric transport in nanocomposites". In: *Phys. Rev. B* 82 (11 2010), p. 115308. DOI: `10.1103/PhysRevB.82.115308`. URL: `http://link.aps.org/doi/10.1103/PhysRevB.82.115308`.

(*59*) Ming-Shan Jeng et al. "Modeling the Thermal Conductivity and Phonon Transport in Nanoparticle Composites Using Monte Carlo Simulation". In: *Journal of Heat Transfer* 130.4, 042410 (2008), p. 042410. DOI: `10.1115/1.2818765`. URL: `http://link.aip.org/link/?JHR/130/042410/1`.

(*60*) A. J. Minnich et al. "Modeling study of thermoelectric SiGe nanocomposites". In: *Physical Review B* 80.15, 155327 (2009), p. 155327. DOI: `10.1103/PhysRevB.80.155327`. URL: `http://link.aps.org/abstract/PRB/v80/e155327`.

(*61*) Chandan Bera et al. "Thermoelectric properties of nanostructured $Si_{1-x}Ge_x$ and potential for further improvement". In: *Journal of Applied Physics* 108.12, 124306 (2010), pp. –. DOI: `http://dx.doi.org/10.1063/1.3518579`. URL: `http://scitation.aip.org/content/aip/journal/jap/108/12/10.1063/1.3518579`.

(*62*) Zhaojie Wang et al. "Thermal Conductivity of Nanocrystalline Silicon: Importance of Grain Size and Frequency-Dependent Mean Free Paths". In: *Nano Lett.* 11.6 (2011), pp. 2206–2213.

(*63*) A. Ward and D. A. Broido. “Intrinsic phonon relaxation times from first-principles studies of the thermal conductivities of Si and Ge”. In: *Phys. Rev. B* 81 (2010), p. 085205.

(*64*) Jean-Philippe M. Peraud and Nicolas G. Hadjiconstantinou. “Efficient simulation of multidimensional phonon transport using energy-based variance-reduced Monte Carlo formulations”. In: *Physical Review B* 84.20 (Nov. 2011), p. 205331.

(*65*) R. Peierls. “On the kinetic theory of thermal conduction in crystals”. In: *Ann. Physik* 3 (1929), p. 1055.

(*66*) M M R Williams. “Some comments on the propagation of temperature waves in insulators”. In: *Journal of Physics D: Applied Physics* 4.8 (1971), p. 1201. URL: `http://stacks.iop.org/0022-3727/4/i=8/a=322`.

(*67*) S Simons. “The application of high frequency thermal propagation data to the measurement of phonon relaxation times”. In: *Journal of Physics C: Solid State Physics* 4.14 (1971), p. 2089. URL: `http://stacks.iop.org/0022-3719/4/i=14/a=024`.

(*68*) G. D. Mahan and Francisco Claro. “Nonlocal theory of thermal conductivity”. In: *Phys. Rev. B* 38.3 (1988), pp. 1963–1969. DOI: `10.1103/PhysRevB.38.1963`.

(*69*) A. A. Joshi and A. Majumdar. “Transient ballistic and diffusive phonon heat transport in thin films”. In: *Journal of Applied Physics* 74.1 (1993), pp. 31–39.

(*70*) Keivan Esfarjani, Gang Chen, and Harold T. Stokes. “Heat transport in silicon from first-principles calculations”. In: *Phys. Rev. B* 84 (8 2011), p. 085204. DOI: `10.1103/PhysRevB.84.085204`. URL: `http://link.aps.org/doi/10.1103/PhysRevB.84.085204`.

(*71*) D. A. Broido, A. Ward, and N. Mingo. “Lattice thermal conductivity of silicon from empirical interatomic potentials”. In: *Phys. Rev. B* 72.1 (2005), p. 014308. DOI: `10.1103/PhysRevB.72.014308`.

(*72*) S. J. Narumanchi, J. Y. Murthy, and C. H. Amon. “Submicron heat transport model is silicon accounting for phonon dispersion and polarization”. In: *J. Heat Transfer* 126 (2005), pp. 946–955.

(*73*) Alan J. H. McGaughey and Ankit Jain. “Nanostructure thermal conductivity prediction by Monte Carlo sampling of phonon free paths”. In: *Applied Physics Letters* 100.6, 061911 (2012), pp. –. DOI: `http://dx.doi.org/10.1063/1.3683539`. URL: `http://scitation.aip.org/content/aip/journal/apl/100/6/10.1063/1.3683539`.

(*74*) Jean-Philippe M. Peraud and Nicolas G. Hadjiconstantinou. "An alternative approach to efficient simulation of micro/nanoscale phonon transport". In: *Applied Physics Letters* 101.15, 153114 (2012), pp. –. DOI: `http://dx.doi.org/10.1063/1.4757607`. URL: `http://scitation.aip.org/content/aip/journal/apl/101/15/10.1063/1.4757607`.

(*75*) J.-P. M. Peraud, C. D. Landon, and N. G. Hadjiconstantinou. "Monte Carlo methods for solving the Botlzmann transport equation". In: *Annual Review of Heat Transfer* (2014), pp. 205–265. DOI: `10.1615/AnnualRevHeatTransfer:2014007381`.

(*76*) Jean-Philippe M. PÉRAUD, Colin D. LANDON, and Nicolas G. HADJICONSTANTINOU. "Deviational methods for small-scale phonon transport". In: *Mechanical Engineering Reviews* 1.2 (2014), FE0013–FE0013. DOI: `10.1299/mer.2014fe0013`.

(*77*) Jean-Philippe M. Péraud and Nicolas G. Hadjiconstantinou. "Adjoint-based deviational Monte Carlo methods for phonon transport calculations". In: *Phys. Rev. B* 91 (23 2015), p. 235321. DOI: `10.1103/PhysRevB.91.235321`. URL: `http://link.aps.org/doi/10.1103/PhysRevB.91.235321`.

(*78*) Qing Hao, Gang Chen, and Ming-Shan Jeng. "Frequency-dependent Monte Carlo simulations of phonon transport in two-dimensional porous silicon with aligned pores". In: *Journal of Applied Physics* 106.11, 114321 (2009), p. 114321.

(*79*) A. J. Minnich et al. "Quasiballistic heat transfer studied using the frequency-dependent Boltzmann transport equation". In: *Phys. Rev. B* 84 (23 2011), p. 235207. DOI: `10.1103/PhysRevB.84.235207`. URL: `http://link.aps.org/doi/10.1103/PhysRevB.84.235207`.

(*80*) M. G. Holland. "Analysis of Lattice Thermal Conductivity". In: *Phys. Rev.* 132.6 (1963), pp. 2461–2471.

(*81*) Asegun S. Henry and Gang Chen. "Spectral Phonon Transport Properties of Silicon Based on Molecular Dynamics Simulations and Lattice Dynamics". In: *Journal of Computational and Theoretical Nanoscience* 5 (2008), pp. 141–152.

(*82*) P. G. Klemens. In: *Proc. Phys. Soc. A* 68.12 (1955), p. 1113. DOI: `10.1088/0370-1298/68/12/303`.

(*83*) J. M. Ziman. *Electrons and Phonons*. Clarendon Press: Oxford, 1960.

(*84*) Mona Zebarjadi et al. "Power Factor Enhancement by Modulation Doping in Bulk Nanocomposites". In: *Nano Letters* 11.6 (2011), pp. 2225–2230. DOI: `10.1021/nl201206d`. URL: `http://pubs.acs.org/doi/abs/10.1021/nl201206d`.

(*85*) C. Dames and G. Chen. “Thermal conductivity of nanostructured thermoelectric materials”. In: *CRC Thermoelectrics Handbook: Macro to Nano*. Ed. by D. Rowe. CRC Press, 2005.

(*86*) Fan Yang and Chris Dames. “Mean free path spectra as a tool to understand thermal conductivity in bulk and nanostructures”. In: *Phys. Rev. B* 87 (3 2013), p. 035437. DOI: `10.1103/PhysRevB.87.035437`. URL: `http://link.aps.org/doi/10.1103/PhysRevB.87.035437`.

(*87*) I. S. Gradshteyn and I. M. Ryzhik. *Table of integrals, series and products*. Academic Press, INC, 1980.

(*88*) Wu Li et al. “Thermal conductivity of diamond nanowires from first principles”. In: *Phys. Rev. B* 85 (2012), p. 195436.

(*89*) W. Li et al. “ShengBTE:a solver of the Botlzmann transport equation for phonons”. In: *Computer Physics Communications* 185 (6 2014), pp. 1747–58. DOI: `10.1016/j.cpc.2014.02.015`.

(*90*) Atsushi Togo. *Phonony*. v1.8.5. URL: `http://phonopy.sourceforge.net`.

(*91*) G. Kresse and J. Hafner. “Ab initio molecular dynamics for liquid metals”. In: *Phys. Rev. B* 48 (17 1993), pp. 13115–13118. DOI: `10.1103/PhysRevB.48.13115`. URL: `http://link.aps.org/doi/10.1103/PhysRevB.48.13115`.

(*92*) G. Kresse and J. Hafner. “Ab initio molecular-dynamics simulation of the liquidmetalamorphous-semiconductor transition in germanium”. In: *Phys. Rev. B* 49 (20 1994), pp. 14251–14269. DOI: `10.1103/PhysRevB.49.14251`. URL: `http://link.aps.org/doi/10.1103/PhysRevB.49.14251`.

(*93*) Kresse G. and J Furthmuller. “Efficiency of ab-initio total energy calculations for metals and semiconductors using a plane-wave basis set”. In: *Computational Materials Science* 6 (1 1996), pp. 15–50. DOI: `10.1016/0927-0256(96)00008-0`.

(*94*) G. Kresse and J. Furthmuller. “Efficient iterative schemes for ab initio total-energy calculations using a plane-wave basis set”. In: *Phys. Rev. B* 54 (16 1996), pp. 11169–11186. DOI: `10.1103/PhysRevB.54.11169`. URL: `http://link.aps.org/doi/10.1103/PhysRevB.54.11169`.

(*95*) David J. Griffiths. *Introduction to electrodynamics*. 3rd. Upper Saddle River, N. J.: Prentice Hall, 1999.

(*96*) Yan Wang, Haoxiang Huang, and Xiulin Ruan. “Decomposition of coherent and incoherent phonon conduction in superlattices and random multilayers”. In: *Phys. Rev. B* 90 (16 2014), p. 165406. DOI: `10.1103/PhysRevB.90.165406`. URL: `http://link.aps.org/doi/10.1103/PhysRevB.90.165406`.

(*97*) Xinjiang Wang and Baoling HUang. “Computational Study of In-Plane Phonon Transport in Si Thin Films”. In: *Scientific Reports* 4.6399 (). DOI: `10.1038/srep06399`.

(*98*) Alexander A. Balandin and Denis L. Nika. “Phononics in low-dimensional materials”. In: *Materials Today* 15.6 (2012), pp. 266 –275. ISSN: 1369-7021. DOI: `http://dx.doi.org/10.1016/S1369-7021(12)70117-7`. URL: `http://www.sciencedirect.com/science/article/pii/S1369702112701177`.

(*99*) Ihtesham Chowdhury et al. “On-chip cooling by superlattice-based thin-film thermoelectrics”. In: *Nature Nanotechnology* 4.4 (Jan. 2009), pp. 235–238. ISSN: 1748-3387. DOI: `10.1038/nnano.2008.417`. URL: `http://www.nature.com/nnano/journal/v4/n4/abs/nnano.2008.417.html`.

(*100*) Zonghui Su et al. “Layer-by-layer thermal conductivities of the Group III nitride films in blue/green light emitting diodes”. In: *Applied Physics Letters* 100.20, 201106 (2012), pp. –. DOI: `http://dx.doi.org/10.1063/1.4718354`. URL: `http://scitation.aip.org/content/aip/journal/apl/100/20/10.1063/1.4718354`.

(*101*) Arden L. Moore and Li Shi. “Emerging challenges and materials for thermal management of electronics”. In: *Materials Today* 17.4 (2014), pp. 163 –174. ISSN: 1369-7021. DOI: `http://dx.doi.org/10.1016/j.mattod.2014.04.003`. URL: `http://www.sciencedirect.com/science/article/pii/S1369702114001138`.

(*102*) Yee Kan Koh et al. “Heat-Transport Mechanisms in Superlattices”. In: *Advanced Functional Materials* 19.4 (2009), pp. 610–615. ISSN: 1616-3028. DOI: `10.1002/adfm.200800984`. URL: `http://dx.doi.org/10.1002/adfm.200800984`.

(*103*) Jungwan Cho et al. “Phonon scattering in strained transition layers for GaN heteroepitaxy”. In: *Phys. Rev. B* 89 (11 2014), p. 115301. DOI: `10.1103/PhysRevB.89.115301`. URL: `http://link.aps.org/doi/10.1103/PhysRevB.89.115301`.

(*104*) F. Fuchs. “the conductivity of thin metallic films according to the electron theory of metals”. In: *Proceedings of Cambridge Philosophy Society* 34 (1938), pp. 100–108.

(*105*) E. H. Sondheimer. “The mean free path of electrons in metals”. In: *Advances in physics* 1 (1952), pp. 1–42.

(*106*) G. Chen and C. L. Tien. “Thermal conductivities of quantum well structures”. In: *Journal of thermophysics and heat transfer* 7 (2 1993), pp. 311–318.

(*107*) Gang Chen. “Size and interface effects on thermal conductivity of superlattices and periodic thin-film structures”. In: *Journal of Heat Transfer* 119 (), pp. 220–229.

(*108*) Sandip Mazumder and Arunava Majumdar. “Monte Carlo Study of Phonon Transport in Solid Thin Films Including Dispersion and Polarization”. In: *Journal of Heat Transfer* 123.4 (2001), pp. 749–759. DOI: `10.1115/1.1377018`. URL: `http://link.aip.org/link/?JHR/123/749/1`.

(*109*) S. Chandrasekhar and G. Munch. “The Theory of the Fluctuations in Brightness of the Milky way I.” In: *Astrophysical Journal* 112 (Nov. 1950), p. 380. DOI: `10.1086/145353`.

(*110*) R. Bellman and G. M. Wing. *An introduction to invariant imbedding*. New York, Wiley, 1975.

(*111*) Kenneth M. Case and Paul F. Zweifel. *Linear transport theory*. Addison-Wesley Publishing Company, Inc, 1967.

(*112*) C.C. Lii and M.N. Özişik. “Transient radiation and conduction in an absorbing, emitting, scattering slab with reflective boundaries”. In: *International Journal of Heat and Mass Transfer* 15.5 (1972), pp. 1175 –1179. ISSN: 0017-9310. DOI: `http://dx.doi.org/10.1016/0017-9310(72)90248-7`. URL: `http://www.sciencedirect.com/science/article/pii/0017931072902487`.

(*113*) G. Chen. “Thermal conductivity and ballistic-phonon transport in the cross-plane direction of superlattices”. In: *Phys. Rev. B* 57 (23 1998), pp. 14958–14973. DOI: `10.1103/PhysRevB.57.14958`. URL: `http://link.aps.org/doi/10.1103/PhysRevB.57.14958`.

(*114*) G. Chen and T. F. Zeng. “Nonequilibrium phonon and electron transport in heterostructures and superlattices”. In: *Microscale thermophysical engineering* 5 (2 2001), pp. 71–88.

(*115*) T. F. Zeng and G. Chen. “Phonon heat conduction in thin films: impact of thermal boundary resistance and internal heat generation”. In: 123 (2001), pp. 340–347.

(*116*) A. D. Polyanin and A. V. Manzhirov. *Handbook of integral equations*. Chapman & Hall/CRC, 2008.

(*117*) H. F. Weinberger. *A first course in partial differential equations with complex variables and transform methods*. Dover Publications, INC., 1995.

(*118*) A. J. Minnich. “Determining Phonon Mean Free Paths from Observations of Quasiballistic Thermal Transport”. In: *Phys. Rev. Lett.* 109 (20 2012), p. 205901. DOI: `10.1103/PhysRevLett.109.205901`. URL: `http://link.aps.org/doi/10.1103/PhysRevLett.109.205901`.

(*119*) Tzu-Kan Hsiao et al. “Observation of room-temperature ballistic thermal conduction persisting over 8.3 μm in SiGe nanowires”. In: *Nature Nanotechnology* 8 (2013), pp. 534–538. DOI: `10.1038/nnano.2013.121`.

(*120*) Xiangfan Xu et al. “Length-dependent thermal conductivity in suspended single-layer graphene”. In: *Nature Communications* 5.3689 (2014). DOI: `10.1038/ncomms4689`.

(*121*) Hang Zhang et al. “Length dependent thermal conductivity measurements yield phonon mean free path spectra in nanostructures”. In: *Scientific Reports, Accepted* ().

(*122*) P. G Sverdrup et al. “Measurement of ballistic phonon conduction near hotspots in silicon”. In: *Appl. Phys. Lett.* 78.21 (May 2001), pp. 3331–3333. ISSN: 000 +36951. DOI: `doi:10.1063/1.1371536`. URL: `http://apl.aip.org/resource/1/applab/v78/i21/p3331_s1`.

(*123*) F Claro and G. D. Mahan. “Transient heat transport in solids”. In: *J. Appl. Phys.* 66.9 (1989), pp. 4213–4217. DOI: `10.1063/1.343960`. URL: `http://link.aip.org/link/?JAP/66/4213/1`.

(*124*) G Chen. “Nonlocal and Nonequilibrium Heat Conduction in the Vicinity of Nanoparticles”. In: *J. Heat Transfer* 118.3 (1996), pp. 539–545. DOI: `10.1115/1.2822665`. URL: `http://link.aip.org/link/?JHR/118/539/1`.

(*125*) Y. Ezzahri and A. Shakouri. “Ballistic and diffusive transport of energy and heat in metals”. In: *Phys. Rev. B* 79.18, 184303 (2009), p. 184303. DOI: `10.1103/PhysRevB.79.184303`. URL: `http://link.aps.org/abstract/PRB/v79/e184303`.

(*126*) A. A. Maznev, Jeremy A. Johnson, and Keith A. Nelson. “Onset of nondiffusive phonon transport in transient thermal grating decay”. In: *Phys. Rev. B* 84 (19 2011), p. 195206. DOI: `10.1103/PhysRevB.84.195206`. URL: `http://link.aps.org/doi/10.1103/PhysRevB.84.195206`.

(*127*) J. A. Rogers, Y. Yang, and K. A. Nelson. “Elastic modulus and in-plane thermal diffusivity measurements in thin polyimide films using symmetry-selective real-time impulsive stimulated thermal scattering”. In: *Appl. Phys. A: Materials Science & Processing* 58 (1994), pp. 523–534. URL: `http://dx.doi.org/10.1007/BF00332448`.

(*128*) Kimberlee C. Collins et al. “Non-diffusive relaxation of a transient thermal grating analyzed with the Boltzmann transport equation”. In: *Journal of Applied Physics* 114.10, 104302 (2013), pp. –. DOI: `http://dx.doi.org/10.1063/1.4820572`. URL: `http://scitation.aip.org/content/aip/journal/jap/114/10/10.1063/1.4820572`.

(*129*) E. T. Swartz and R. O. Pohl. “Thermal boundary resistance”. In: *Rev. Mod. Phys.* 61 (3 1989), pp. 605–668. DOI: `10.1103/RevModPhys.61.605`. URL: `http://link.aps.org/doi/10.1103/RevModPhys.61.605`.

(*130*) David G. Cahill et al. “Nanoscale thermal transport. II. 2003–2012”. In: *Applied Physics Reviews* 1.1, 011305 (2014), p. 011305. DOI: `http://dx.doi.org/10.1063/1.4832615`. URL: `http://scitation.aip.org/content/aip/journal/apr2/1/1/10.1063/1.4832615`.

(*131*) Sune Pettersson and G. D. Mahan. “Theory of the thermal boundary resistance between dissimilar lattices”. In: *Phys. Rev. B* 42.12 (Oct. 1990), pp. 7386–7390. DOI: `10.1103/PhysRevB.42.7386`. URL: `http://link.aps.org/doi/10.1103/PhysRevB.42.7386`.

(*132*) Jayakanth Ravichandran et al. “Crossover from incoherent to coherent phonon scattering in epitaxial oxide superlattices”. In: *Nature Materials* 13 (2014), pp. 168–172. DOI: `10.1038/nmat3826`.

(*133*) Peixuan Chen et al. “Role of Surface-Segregation-Driven Intermixing on the Thermal Transport through Planar Si/Ge Superlattices”. In: *Phys. Rev. Lett.* 111 (11 2013), p. 115901. DOI: `10.1103/PhysRevLett.111.115901`. URL: `http://link.aps.org/doi/10.1103/PhysRevLett.111.115901`.

(*134*) C. Chiritescu et al. “Ultralow thermal conductivity in disordered, layered WSe2 crystals”. In: *Science* 315 (5810 2007), pp. 351–353. DOI: `10.1126/science.1136494`.

(*135*) Eric Pop. “Energy dissipation and transport in nanoscale devices”. In: *Nano Research* 3.3 (2010), pp. 147–169. ISSN: 1998-0124. DOI: `10.1007/s12274-010-1019-z`. URL: `http://dx.doi.org/10.1007/s12274-010-1019-z`.

(*136*) Jungwan Cho and Kenneth E. Goodson. “Thermal transport: Cool electronics”. In: *Nature Materials* 14 (2015), pp. 136–137. DOI: `10.1038/nmat4194`.

(*137*) Zonghui Su et al. “Layer-by-layer thermal conductivities of the Group III nitride films in blue/green light emitting diodes”. In: *Applied Physics Letters* 100.20, 201106 (2012), p. 201106. DOI: `http://dx.doi.org/10.1063/1.4718354`. URL: `http://scitation.aip.org/content/aip/journal/apl/100/20/10.1063/1.4718354`.

(*138*) Nam Han et al. “Improved heat dissiapation in gallium nitride light-emitting diodes with embedded graphene oxide pattern”. In: *Nature Communications* 4 (2013), p. 1452. DOI: `10.1038/ncomms2448`.

(*139*) Zhong Yan et al. “Graphene quilts for thermal management of high-power GaN transistors”. In: *Nature Communications* 3 (2011), p. 827. DOI: `10.1038/ncomms1828`.

(*140*) Tom Klitsner and R. O. Pohl. “Phonon scattering at silicon crystal surfaces”. en. In: *Physical Review B* 36.12 (Oct. 1987), pp. 6551–6565. ISSN: 0163-1829. DOI: `10.1103/PhysRevB.36.6551`. URL: `http://link.aps.org/doi/10.1103/PhysRevB.36.6551` (visited on 04/20/2016).

(*141*) E. T. Swartz and R. O. Pohl. “Thermal resistance at interfaces”. In: *Applied Physics Letters* 51.26 (1987).

(*142*) I. M. Khalatnikov. “Teploobmen mezhdu tverdym telom I gelium — II”. In: *Sov. Phys. JETP* 22 (6 1952), pp. 687–704.

(*143*) W. A. Little. “THE TRANSPORT OF HEAT BETWEEN DISSIMILAR SOLIDS AT LOW TEMPERATURES”. In: *Canadian Journal of Physics* 37.3 (1959), pp. 334–349. DOI: `10.1139/p59-037`. eprint: `http://dx.doi.org/10.1139/p59-037`. URL: `http://dx.doi.org/10.1139/p59-037`.

(*144*) A. Maiti, G.D. Mahan, and S.T. Pantelides. “Dynamical simulations of nonequilibrium processes — Heat flow and the Kapitza resistance across grain boundaries”. In: *Solid State Communications* 102.7 (1997), pp. 517 –521. ISSN: 0038-1098. DOI: `http://dx.doi.org/10.1016/S0038-1098(97)00049-5`. URL: `http://www.sciencedirect.com/science/article/pii/S0038109897000495`.

(*145*) Robert J. Stevens, Leonid V. Zhigilei, and Pamela M. Norris. “Effects of temperature and disorder on thermal boundary conductance at solid–solid interfaces: Nonequilibrium molecular dynamics simulations”. In: *International Journal of Heat and Mass Transfer* 50.19–20 (2007), pp. 3977 –3989. ISSN: 0017-9310. DOI: `http://dx.doi.org/10.1016/j.ijheatmasstransfer.2007.01.040`. URL: `http://www.sciencedirect.com/science/article/pii/S0017931007001342`.

(*146*) E. S. Landry and A. J. H. McGaughey. “Thermal boundary resistance predictions from molecular dynamics simulations and theoretical calculations”. In: *Phys. Rev. B* 80 (16 2009), p. 165304. DOI: `10.1103/PhysRevB.80.165304`. URL: `http://link.aps.org/doi/10.1103/PhysRevB.80.165304`.

(*147*) Woon Ih Choi, Kwiseon Kim, and Sreekant Narumanchi. “Thermal conductance at atomically clean and disordered silicon/aluminum interfaces: A molecular dynamics simulation study”. In: *Journal of Applied Physics* 112.5, 054305 (2012), p. 054305. DOI: `http://dx.doi.org/10.1063/1.4748872`. URL: `http://scitation.aip.org/content/aip/journal/jap/112/5/10.1063/1.4748872`.

(*148*) R. E. Jones et al. “Investigation of size and electronic effects on Kapitza conductance with non-equilibrium molecular dynamics”. In: *Applied Physics Letters* 102.18, 183119 (2013), p. 183119. DOI: `http://dx.doi.org/10.1063/1.4804677`. URL: `http://scitation.aip.org/content/aip/journal/apl/102/18/10.1063/1.4804677`.

(*149*) N. Yang et al. “Thermal Interface Conductance between Aluminum and Silicon by Molecular Dynamics Simulations”. In: *Journal of Computational and Theoretical Nanoscience* in press (2013).

(*150*) Samy Merabia and Konstantinos Termentzidis. "Thermal boundary conductance across rough interfaces probed by molecular dynamics". In: *Phys. Rev. B* 89 (5 2014), p. 054309. DOI: `10.1103/PhysRevB.89.054309`. URL: `http://link.aps.org/doi/10.1103/PhysRevB.89.054309`.

(*151*) Zhi Liang and Pawel Keblinski. "Finite-size effects on molecular dynamics interfacial thermal-resistance predictions". In: *Phys. Rev. B* 90 (7 2014), p. 075411. DOI: `10.1103/PhysRevB.90.075411`. URL: `http://link.aps.org/doi/10.1103/PhysRevB.90.075411`.

(*152*) P. K. Schelling, S. R. Phillpot, and P. Keblinski. "Phonon wave-packet dynamics at semiconductor interfaces by molecular-dynamics simulation". In: *Applied Physics Letters* 80.14 (2002).

(*153*) W. Zhang, T.S. Fisher, and N. Mingo. "Simulation of interfacial phonon transport in Si-Ge heterostructure using an atomistic Green's function method". In: *Journal of heat transfer* 129 (4 2006), pp. 483–491. DOI: `10.1115/1.2709656`.

(*154*) Xiaobo Li and Ronggui Yang. "Effect of lattice mismatch on phonon transmission and interface thermal conductance across dissimilar material interfaces". In: *Phys. Rev. B* 86 (5 2012), p. 054305. DOI: `10.1103/PhysRevB.86.054305`. URL: `http://link.aps.org/doi/10.1103/PhysRevB.86.054305`.

(*155*) Zhiting Tian, Keivan Esfarjani, and Gang Chen. "Green's function studies of phonon transport across Si/Ge superlattices". In: *Phys. Rev. B* 89 (23 2014), p. 235307. DOI: `10.1103/PhysRevB.89.235307`. URL: `http://link.aps.org/doi/10.1103/PhysRevB.89.235307`.

(*156*) Zhen Huang, Timothy S. Fisher, and Jayathi Y. Murthy. "Simulation of phonon transmission through graphene and graphene nanoribbons with a Green's function method". In: *Journal of Applied Physics* 108.9, 094319 (2010), p. 094319. DOI: `http://dx.doi.org/10.1063/1.3499347`. URL: `http://scitation.aip.org/content/aip/journal/jap/108/9/10.1063/1.3499347`.

(*157*) Patrick E. Hopkins et al. "Extracting phonon thermal conductance across atomic junctions: Nonequilibrium Green's function approach compared to semiclassical methods". In: *Journal of Applied Physics* 106.6, 063503 (2009), p. 063503. DOI: `http://dx.doi.org/10.1063/1.3212974`. URL: `http://scitation.aip.org/content/aip/journal/jap/106/6/10.1063/1.3212974`.

(*158*) R. Wilson and D. Cahill. "Anisotropic failure of Fourier theory in time-domain thermoreflectance experiments". In: *Nature Communications* 5.5075 (2013). DOI: `10.1038/ncommms6075`.

(*159*) William S. Capinski and Humphrey J. Maris. "Improved apparatus for picosecond pump and probe optical measurements". In: *Review of Scientific Instruments* 67.8 (1996).

(*160*) David G. Cahill. "Analysis of heat flow in layered structures for time-domain thermoreflectance". In: *Review of Scientific Instruments* 75.12 (2004), pp. 5119–5122.

(*161*) Aaron J. Schmidt, Xiaoyuan Chen, and Gang Chen. "Pulse accumulation, radial heat conduction, and anisotropic thermal conductivity in pump-probe transient thermoreflectance". In: *Review of Scientific Instruments* 79.11, 114902 (2008), p. 114902. DOI: `http://dx.doi.org/10.1063/1.3006335`. URL: `http://scitation.aip.org/content/aip/journal/rsi/79/11/10.1063/1.3006335`.

(*162*) Yee Kan Koh and David G. Cahill. "Frequency dependence of the thermal conductivity of semiconductor alloys". In: *Physical Review B* 76.7, 075207 (2007), p. 075207.

(*163*) K. Regner et al. "Broadband phonon mean free path contributions to thermal conductivity measured using frequency-domain thermoreflectance". In: *Nature Communications* 4.1640 (2012). DOI: `10.1038/ncomms2630`.

(*164*) Bjorn Vermeersch et al. "Superdiffusive heat conduction in semiconductor alloys. II. Truncated Lévy formalism for experimental analysis". In: *Phys. Rev. B* 91 (8 2015), p. 085203. DOI: `10.1103/PhysRevB.91.085203`. URL: `http://link.aps.org/doi/10.1103/PhysRevB.91.085203`.

(*165*) R. B. Wilson et al. "Two-channel model for nonequilibrium thermal transport in pump-probe experiments". In: *Phys. Rev. B* 88 (14 2013), p. 144305. DOI: `10.1103/PhysRevB.88.144305`. URL: `http://link.aps.org/doi/10.1103/PhysRevB.88.144305`.

(*166*) K. T. Regner, A. J. H. McGaughey, and J. A. Malen. "Analytical interpretation of nondiffusive phonon transport in thermoreflectance thermal conductivity measurements". In: *Phys. Rev. B* 90 (6 2014), p. 064302. DOI: `10.1103/PhysRevB.90.064302`. URL: `http://link.aps.org/doi/10.1103/PhysRevB.90.064302`.

(*167*) Yee Kan Koh, David G. Cahill, and Bo Sun. "Nonlocal theory for heat transport at high frequencies". In: *Phys. Rev. B* 90 (20 2014), p. 205412. DOI: `10.1103/PhysRevB.90.205412`. URL: `http://link.aps.org/doi/10.1103/PhysRevB.90.205412`.

(*168*) Jesse Maassen and Mark Lundstrom. "Steady-state heat transport: Ballistic-to-diffusive with Fourier's law". In: *Journal of Applied Physics* 117.3, 035104 (2015), p. 035104. DOI: `http://dx.doi.org/10.1063/1.4905590`. URL: `http://scitation.aip.org/content/aip/journal/jap/117/3/10.1063/1.4905590`.

(*169*) Chengyun Hua and Austin J. Minnich. “Analytical Green’s function of the multidimensional frequency-dependent phonon Boltzmann equation”. In: *Phys. Rev. B* 90 (21 2014), p. 214306. DOI: `10.1103/PhysRevB.90.214306`. URL: `http://link.aps.org/doi/10.1103/PhysRevB.90.214306`.

(*170*) Chengyun Hua and Austin J. Minnich. “Semi-analytical solution to the frequency-dependent Boltzmann transport equation for cross-plane heat conduction in thin films”. In: *Journal of Applied Physics* 117.17, 175306 (2015). DOI: `http://dx.doi.org/10.1063/1.4919432`. URL: `http://scitation.aip.org/content/aip/journal/jap/117/17/10.1063/1.4919432`.

(*171*) Jaeho Lee et al. “Phonon and electron transport through Ge2Sb2Te5 films and interfaces bounded by metals”. In: *Applied Physics Letters* 102.19 (May 2013), p. 191911. ISSN: 0003-6951, 1077-3118. DOI: `10.1063/1.4807141`. URL: `http://scitation.aip.org/content/aip/journal/apl/102/19/10.1063/1.4807141` (visited on 03/12/2015).

(*172*) Ashutosh Giri et al. “Mechanisms of nonequilibrium electron-phonon coupling and thermal conductance at interfaces”. In: *Journal of Applied Physics* 117.10 (Mar. 2015), p. 105105. ISSN: 0021-8979, 1089-7550. DOI: `10.1063/1.4914867`. URL: `http://scitation.aip.org/content/aip/journal/jap/117/10/10.1063/1.4914867` (visited on 03/13/2015).

(*173*) Atsushi Togo. *Phonony*. v1.8.5. URL: `http://phonopy.sourceforge.net`.

(*174*) D. A. Broido et al. “Intrinsic lattice thermal conductivity of semiconductors from first principles”. In: *Applied Physics Letters* 91.23, 231922 (2007), p. 231922. DOI: `http://dx.doi.org/10.1063/1.2822891`. URL: `http://scitation.aip.org/content/aip/journal/apl/91/23/10.1063/1.2822891`.

(*175*) Keivan Esfarjani, Gang Chen, and Harold T. Stokes. “Heat transport in silicon from first-principles calculations”. In: *Phys. Rev. B* 84 (8 2011), p. 085204. DOI: `10.1103/PhysRevB.84.085204`. URL: `http://link.aps.org/doi/10.1103/PhysRevB.84.085204`.

(*176*) John Cuffe et al. “Reconstructing phonon mean free path contributions to thermal conductivity using nanoscale membranes”. In: *arXiv:1408.6747* (2014).

(*177*) Hong Zhao and Jonathan B. Freund. “Phonon scattering at a rough interface between two fcc lattices”. In: *Journal of Applied Physics* 105.1 (2009), pp. –. DOI: `http://dx.doi.org/10.1063/1.3054383`. URL: `http://scitation.aip.org/content/aip/journal/jap/105/1/10.1063/1.3054383`.

(*178*) Meng Shen and Pawel Keblinski. “Ballistic vs. diffusive heat transfer across nanoscopic films of layered crystals”. en. In: *Journal of Applied Physics* 115.14 (Apr. 2014), p. 144310. ISSN: 0021-8979, 1089-7550. DOI: `10.1063/1.4870940`. URL: `http://scitation.aip.org/content/aip/journal/jap/115/14/10.1063/1.4870940` (visited on 04/21/2016).

(*179*) Aaron J. Schmidt. “Optical Characterization of Thermal Transport from the nanoscale to macroscale”. PhD thesis. Massachusetts Institute of Technology, 2008.

(*180*) John C. Duda et al. “On the Assumption of Detailed Balance in Prediction of Diffusive Transmission Probability During Interfacial Transport”. en. In: *Nanoscale and Microscale Thermophysical Engineering* 14.1 (Mar. 2010), pp. 21–33. ISSN: 1556-7265, 1556-7273. DOI: `10.1080/15567260903530379`. URL: `http://www.tandfonline.com/doi/abs/10.1080/15567260903530379` (visited on 06/24/2015).

(*181*) Takuru Murakami et al. “Probing and tuning inelastic phonon conductance across finite-thickness interface”. In: *Applied Physics Express* 7.12 (2014), p. 121801. URL: `http://stacks.iop.org/1882-0786/7/i=12/a=121801`.

(*182*) Kathleen M. Hoogeboom-Pot et al. “A new regime of nanoscale thermal transport: Collective diffusion increases dissipation efficiency”. en. In: *Proceedings of the National Academy of Sciences* 112.16 (Apr. 2015), pp. 4846–4851. ISSN: 0027-8424, 1091-6490. DOI: `10.1073/pnas.1503449112`. URL: `http://www.pnas.org/lookup/doi/10.1073/pnas.1503449112` (visited on 06/12/2015).

(*183*) Kwangu Kang et al. “Two-tint pump-probe measurements using a femtosecond laser oscillator and sharp-edged optical filters”. In: *Review of Scientific Instruments* 79.11, 114901 (2008), pp. –. DOI: `http://dx.doi.org/10.1063/1.3020759`. URL: `http://scitation.aip.org/content/aip/journal/rsi/79/11/10.1063/1.3020759`.

(*184*) Shin-ichiro Tamura. “Isotope scattering of dispersive phonons in Ge”. In: *Phys. Rev. B* 27 (2 1983), pp. 858–866. DOI: `10.1103/PhysRevB.27.858`. URL: `http://link.aps.org/doi/10.1103/PhysRevB.27.858`.

(*185*) Jivtesh Garg et al. “Role of Disorder and Anharmonicity in the Thermal Conductivity of Silicon-Germanium Alloys: A First-Principles Study”. en. In: *Physical Review Letters* 106.4 (Jan. 2011). ISSN: 0031-9007, 1079-7114. DOI: `10.1103/PhysRevLett.106.045901`. URL: `http://link.aps.org/doi/10.1103/PhysRevLett.106.045901` (visited on 09/02/2015).

Appendix A

SPECULAR BOUNDARIES

Section 3.3 derived the BTE solutions in thin films with diffuse boundary scattering. Here, we derive the governing equation for the problem of nonblack, specular boundaries with wall temperatures ΔT_1 and ΔT_2, respectively. The boundary conditions can be written as:

$$\begin{aligned} \widetilde{g}_\omega^+(x=0,\mu) &= P_\omega = \epsilon_1 \frac{C_\omega}{4\pi}\Delta T_1 + (1-\epsilon_1)\widetilde{g}_\omega^-(x=0,-\mu) && \text{(A.1)} \\ \widetilde{g}_\omega^-(x=L,\mu) &= B_\omega = \epsilon_2 \frac{C_\omega}{4\pi}\Delta T_2 + (1-\epsilon_2)\widetilde{g}_\omega^+(x=L,-\mu), && \text{(A.2)} \end{aligned}$$

Applying the boundary conditions to Eqs. (5.6) & (5.7), we have

$$\begin{aligned} \widetilde{g}_\omega^+(x) &= F_1\Delta T_1 \frac{C_\omega}{4\pi} e^{-\frac{\gamma_\omega}{\mu}x} + (1-\epsilon_1)F_2\Delta T_2 \frac{C_\omega}{4\pi} e^{-\frac{\gamma_\omega}{\mu}(L+x)} \\ &+ (1-\epsilon_1)F_2 \int_0^L \frac{C_\omega \Delta\widetilde{T}(x') + \widetilde{Q}_\omega(x')\tau_\omega}{4\pi\Lambda_\omega\mu} e^{-\frac{\gamma_\omega}{\mu}(x'+x)} dx' \\ &+ \int_0^x \frac{C_\omega \Delta\widetilde{T}(x') + \widetilde{Q}_\omega(x')\tau_\omega}{4\pi\Lambda_\omega\mu} e^{\frac{\gamma_\omega}{\mu}(x'-x)} dx' \; (\mu \in [0,1]), && \text{(A.3)} \\ \widetilde{g}_\omega^-(x) &= F_2\Delta T_2 \frac{C_\omega}{4\pi} e^{-\frac{\gamma_\omega}{\mu}(L-x)} + (1-\epsilon_2)F_1\Delta T_1 \frac{C_\omega}{4\pi} e^{-\frac{\gamma_\omega}{\mu}(2L-x)} \\ &+ (1-\epsilon_2)F_1 \int_0^L \frac{C_\omega \Delta\widetilde{T}(x') + \widetilde{Q}_\omega(x')\tau_\omega}{4\pi\Lambda_\omega\mu} e^{-\frac{\gamma_\omega}{\mu}(2L-x'-x)} dx' \\ &+ \int_x^L \frac{C_\omega \Delta\widetilde{T}(x') + \widetilde{Q}_\omega(x')\tau_\omega}{4\pi\Lambda_\omega\mu} e^{-\frac{\gamma_\omega}{\mu}(x'-x)} dx' \; (\mu \in [0,1]), && \text{(A.4)} \end{aligned}$$

where $F_1 = \frac{\epsilon_1}{\epsilon_1+\epsilon_2-\epsilon_1\epsilon_2}$ and $F_2 = \frac{\epsilon_2}{\epsilon_1+\epsilon_2-\epsilon_1\epsilon_2}$.

To close the problem, we insert Eqs. (A.3) & (A.4) into Eq. (5.4) and nondimensionalize x by L. We then derive an integral equation for temperature for the specular boundary conditions, given by

$$\begin{aligned} 2\int_0^{\omega_m} \frac{C_\omega}{\tau_\omega} d\omega \Delta\widetilde{T}(\widehat{x}) &= \int_0^{\omega_m} \frac{C_\omega}{\tau_\omega} H_\omega(\widehat{x}) d\omega + \int_0^1 \int_0^{\omega_m} \widetilde{Q}_\omega(x') \frac{G_\omega(\widehat{x},\widehat{x}')}{\text{Kn}_\omega} d\omega d\widehat{x}' \\ &+ \int_0^1 \Delta\widetilde{T}(\widehat{x}') \int_0^{\omega_m} \frac{C_\omega G_\omega(\widehat{x},\widehat{x}')}{\text{Kn}_\omega \tau_\omega} d\omega d\widehat{x}', && \text{(A.5)} \end{aligned}$$

where $\widehat{x} = x/L$, $\mathrm{Kn}_\omega = \Lambda_\omega/L$ is the Knudsen number, $\widehat{\gamma}_\omega = \frac{1+i\eta\tau_\omega}{\mathrm{Kn}_\omega}$ and

$$\begin{aligned} H_\omega(\widehat{x}) &= F_1\Delta T_1 E_2(\widehat{\gamma}_\omega\widehat{x}) + F_2\Delta T_2 E_2(\widehat{\gamma}_\omega(1-\widehat{x})) \\ &+ (1-\epsilon_1)F_2\Delta T_2 E_2(\widehat{\gamma}_\omega(1+\widehat{x})) + (1-\epsilon_2)F_1\Delta T_1 E_2(\widehat{\gamma}_\omega(2-\widehat{x})) \end{aligned} \tag{A.6}$$

and

$$G_\omega(\widehat{x},\widehat{x}') = (1-\epsilon_1)F_2E_1(\widehat{\gamma}_\omega(\widehat{x}+\widehat{x}')) + (1-\epsilon_2)F_1E_1(\widehat{\gamma}_\omega(2-\widehat{x}-\widehat{x}')) + E_1(\widehat{\gamma}_\omega|\widehat{x}-\widehat{x}'|). \tag{A.7}$$

In this case, the inhomogeneous function becomes

$$f(\widehat{x}) = \frac{1}{2\int_0^{\omega_m}\frac{C_\omega}{\tau_\omega}d\omega}\left[\int_0^{\omega_m}\frac{C_\omega}{\tau_\omega}H_\omega(\widehat{x})d\omega + \int_0^1\int_0^{\omega_m}\widetilde{Q}_\omega(x')\frac{G_\omega(\widehat{x},\widehat{x}')}{\mathrm{Kn}_\omega}d\omega d\widehat{x}'\right] \tag{A.8}$$

and the kernel function becomes

$$K(\widehat{x},\widehat{x}') = \frac{1}{2\int_0^{\omega_m}\frac{C_\omega}{\tau_\omega}d\omega}\int_0^{\omega_m}\frac{C_\omega G_\omega(\widehat{x},\widehat{x}')}{\mathrm{Kn}_\omega\tau_\omega}d\omega. \tag{A.9}$$

With these results, the problem can be solved by following the same procedures described in Sec.3.3 are followed to formulate a linear system of equations. The solution of this system then yields the temperature Fourier coefficients.

Appendix B

FOURIER COEFFICIENTS FOR NONBLACK DIFFUSE BOUNDARIES

Section 3.3 demonstrated an example calculation for steady-state heat conduction between two walls that are either black or non-black. In this section we derive the Fourier coefficients of the kernel function $K(\widehat{x}, \widehat{x}')$ and the inhomogeneous function $f(\widehat{x})$ for these two specific cases.

For steady-state heat conduction between two non-black walls as studied in Sec. 3.3, the inhomogeneous function becomes

$$f(\widehat{x}) = \frac{1}{2\int_0^{\omega_m} \frac{C_\omega}{\tau_\omega} d\omega} \int_0^{\omega_m} \frac{C_\omega}{\tau_\omega} \left[A_{1\omega} E_2\left(\frac{\widehat{x}}{\mathrm{Kn}_\omega}\right) + A_{2\omega} E_2\left(\frac{1-\widehat{x}}{\mathrm{Kn}_\omega}\right) \right] d\omega. \tag{B.1}$$

Its Fourier coefficients in Eq. (3.34) are then given by:

$$f_0 = \frac{1}{2\int_0^{\omega_m} \frac{C_\omega}{\tau_\omega} d\omega} \int_0^{\omega_m} \frac{C_\omega \mathrm{Kn}_\omega}{\tau_\omega} (A_{1\omega} + A_{2\omega}) \left[1 - 2E_3\left(\frac{1}{\mathrm{Kn}_\omega}\right) \right] d\omega, \tag{B.2}$$

and

$$f_n = \frac{1}{\int_0^{\omega_m} \frac{C_\omega}{\tau_\omega} d\omega} \int_0^{\omega_m} \int_0^1 \frac{C_\omega}{\tau_\omega} \mathrm{Kn}_\omega \mu \frac{[A_{1\omega} + (-1)^n A_{2\omega}] - e^{-\frac{1}{\mathrm{Kn}_\omega \mu}} [(-1)^n A_{1\omega} + A_{2\omega}]}{1 + (\mathrm{Kn}_\omega \mu)^2 (n\pi)^2}, \tag{B.3}$$

providing the right-hand side of Eq. (3.39). Under the same assumption of diffuse, non-black walls, the kernel function becomes

$$K(\widehat{x}, \widehat{x}') = \frac{1}{2\int_0^{\omega_m} \frac{C_\omega}{\tau_\omega} d\omega} \int_0^{\omega_m} \frac{C_\omega G_\omega(\widehat{x}, \widehat{x}')}{\mathrm{Kn}_\omega \tau_\omega} d\omega, \tag{B.4}$$

where

$$\begin{aligned} G_\omega(\widehat{x}, \widehat{x}') &= E_2\left(\frac{\widehat{x}}{\mathrm{Kn}_\omega}\right) \left[D_\omega E_1\left(\frac{1-\widehat{x}'}{\mathrm{Kn}_\omega}\right) + B_{1\omega} E_1\left(\frac{\widehat{x}'}{\mathrm{Kn}_\omega}\right) \right] \qquad \text{(B.5)} \\ &+ E_2\left(\frac{1-\widehat{x}}{\mathrm{Kn}_\omega}\right) \left[D_\omega E_1\left(\frac{\widehat{x}'}{\mathrm{Kn}_\omega}\right) + B_{1\omega} E_1\left(\frac{1-\widehat{x}'}{\mathrm{Kn}_\omega}\right) \right] + E_1\left(\frac{|\widehat{x} - \widehat{x}'|}{\mathrm{Kn}_\omega}\right). \end{aligned}$$

Its Fourier coefficients k_{mn} are given by Eq. (3.35), and can be evaluated as:

$$\begin{aligned} k_{00} \quad &= \frac{2}{\int_0^{\omega_m} \frac{C_\omega}{\tau_\omega} d\omega} \int_0^{\omega_m} \frac{C_\omega \mathrm{Kn}_\omega}{\tau_\omega} \left\{ \frac{2}{\mathrm{Kn}_\omega} - 1 + 2E_3\left(\frac{1}{\mathrm{Kn}_\omega}\right) \right. \\ &\left. + (2D_\omega + B_{1\omega} + B_{2\omega}) \left[\frac{1}{2} - E_3\left(\frac{1}{\mathrm{Kn}_\omega}\right) - \frac{1}{2}E_2\left(\frac{1}{\mathrm{Kn}_\omega}\right) + E_3\left(\frac{1}{\mathrm{Kn}_\omega}\right) E_2\left(\frac{1}{\mathrm{Kn}_\omega}\right) \right] \right\} d\omega, \end{aligned} \tag{B.6}$$

and

$$\begin{aligned} k_{m0} \quad &= \frac{2}{\int_0^{\omega_m} \frac{C_\omega}{\tau_\omega} d\omega} \int_0^{\omega_m} \frac{C_\omega}{\tau_\omega} \int_0^1 \frac{\mathrm{Kn}_\omega \mu [(-1)^m + 1] \left[e^{-\frac{1}{\mathrm{Kn}_\omega \mu}} - 1 \right]}{1 + (\mathrm{Kn}_\omega \mu)^2 (m\pi)^2} d\mu d\omega \\ &+ \frac{2}{\int_0^{\omega_m} \frac{C_\omega}{\tau_\omega} d\omega} \int_0^{\omega_m} \frac{C_\omega}{\tau_\omega} (D_\omega + B_{1\omega}) \left[1 - E_2\left(\frac{1}{\mathrm{Kn}_\omega}\right) \right] \int_0^1 \frac{\mathrm{Kn}_\omega \mu \left[1 - (-1)^m e^{-\frac{1}{\mathrm{Kn}_\omega \mu}} \right]}{1 + (\mathrm{Kn}_\omega \mu)^2 (m\pi)^2} d\mu d\omega \\ &+ \frac{2}{\int_0^{\omega_m} \frac{C_\omega}{\tau_\omega} d\omega} \int_0^{\omega_m} \frac{C_\omega}{\tau_\omega} (D_\omega + B_{2\omega}) \left[1 - E_2\left(\frac{1}{\mathrm{Kn}_\omega}\right) \right] \int_0^1 \frac{\mathrm{Kn}_\omega \mu \left[(-1)^m - e^{-\frac{1}{\mathrm{Kn}_\omega \mu}} \right]}{1 + (\mathrm{Kn}_\omega \mu)^2 (m\pi)^2} d\mu d\omega, \end{aligned} \tag{B.7}$$

and

$$\begin{aligned} k_{0n} \quad &= \frac{2}{\int_0^{\omega_m} \frac{C_\omega}{\tau_\omega} d\omega} \int_0^{\omega_m} \frac{C_\omega}{\tau_\omega} \int_0^1 \frac{\mathrm{Kn}_\omega \mu [(-1)^n + 1] \left[e^{-\frac{1}{\mathrm{Kn}_\omega \mu}} - 1 \right]}{1 + (\mathrm{Kn}_\omega \mu)^2 (n\pi)^2} d\mu d\omega \\ &+ \frac{2}{\int_0^{\omega_m} \frac{C_\omega}{\tau_\omega} d\omega} \int_0^{\omega_m} \frac{C_\omega \mathrm{Kn}_\omega}{\tau_\omega} (D_\omega + B_{1\omega}) \left[\frac{1}{2} - E_3\left(\frac{1}{\mathrm{Kn}_\omega}\right) \right] \int_0^1 \frac{\left[1 - (-1)^n e^{-\frac{1}{\mathrm{Kn}_\omega \mu}} \right]}{1 + (\mathrm{Kn}_\omega \mu)^2 (n\pi)^2} d\mu d\omega \\ &+ \frac{2}{\int_0^{\omega_m} \frac{C_\omega}{\tau_\omega} d\omega} \int_0^{\omega_m} \frac{C_\omega \mathrm{Kn}_\omega}{\tau_\omega} (D_\omega + B_{2\omega}) \left[\frac{1}{2} - E_3\left(\frac{1}{\mathrm{Kn}_\omega}\right) \right] \int_0^1 \frac{\left[(-1)^n - e^{-\frac{1}{\mathrm{Kn}_\omega \mu}} \right]}{1 + (\mathrm{Kn}_\omega \mu)^2 (n\pi)^2} d\mu d\omega, \end{aligned} \tag{B.8}$$

and for $m \neq n$

$$\begin{aligned} k_{mn} \quad &= \frac{2}{\int_0^{\omega_m} \frac{C_\omega}{\tau_\omega} d\omega} \int_0^{\omega_m} \frac{C_\omega}{\tau_\omega} \int_0^1 \frac{\mathrm{Kn}_\omega \mu \left\{ e^{-\frac{1}{\mathrm{Kn}_\omega \mu}} [(-1)^m + (-1)^n] - [1 + (-1)^{m+n} \right\}}{[1 + (\mathrm{Kn}_\omega \mu)^2 (m\pi)^2][1 + (\mathrm{Kn}_\omega \mu)^2 (n\pi)^2]} d\mu d\omega \\ &+ \frac{2}{\int_0^{\omega_m} \frac{C_\omega}{\tau_\omega} d\omega} \int_0^{\omega_m} \frac{C_\omega D_\omega}{\tau_\omega} \int_0^1 \frac{\mathrm{Kn}_\omega \mu \left[1 - (-1)^m e^{-\frac{1}{\mathrm{Kn}_\omega \mu}} \right]}{1 + (\mathrm{Kn}_\omega \mu)^2 (m\pi)^2} d\mu \int_0^1 \frac{\left[(-1)^n - e^{-\frac{1}{\mathrm{Kn}_\omega \mu}} \right]}{1 + (\mathrm{Kn}_\omega \mu)^2 (n\pi)^2} d\mu d\omega \\ &+ \frac{2}{\int_0^{\omega_m} \frac{C_\omega}{\tau_\omega} d\omega} \int_0^{\omega_m} \frac{C_\omega D_\omega}{\tau_\omega} \int_0^1 \frac{\mathrm{Kn}_\omega \mu \left[(-1)^m - e^{-\frac{1}{\mathrm{Kn}_\omega \mu}} \right]}{1 + (\mathrm{Kn}_\omega \mu)^2 (m\pi)^2} d\mu \int_0^1 \frac{\left[1 - (-1)^n e^{-\frac{1}{\mathrm{Kn}_\omega \mu}} \right]}{1 + (\mathrm{Kn}_\omega \mu)^2 (n\pi)^2} d\mu d\omega \\ &+ \frac{2}{\int_0^{\omega_m} \frac{C_\omega}{\tau_\omega} d\omega} \int_0^{\omega_m} \frac{C_\omega B_{1\omega}}{\tau_\omega} \int_0^1 \frac{\mathrm{Kn}_\omega \mu \left[1 - (-1)^m e^{-\frac{1}{\mathrm{Kn}_\omega \mu}} \right]}{1 + (\mathrm{Kn}_\omega \mu)^2 (m\pi)^2} d\mu \int_0^1 \frac{\left[1 - (-1)^n e^{-\frac{1}{\mathrm{Kn}_\omega \mu}} \right]}{1 + (\mathrm{Kn}_\omega \mu)^2 (n\pi)^2} d\mu d\omega \\ &+ \frac{2}{\int_0^{\omega_m} \frac{C_\omega}{\tau_\omega} d\omega} \int_0^{\omega_m} \frac{C_\omega B_{2\omega}}{\tau_\omega} \int_0^1 \frac{\mathrm{Kn}_\omega \mu \left[(-1)^m - e^{-\frac{1}{\mathrm{Kn}_\omega \mu}} \right]}{1 + (\mathrm{Kn}_\omega \mu)^2 (m\pi)^2} d\mu \int_0^1 \frac{\left[(-1)^n - e^{-\frac{1}{\mathrm{Kn}_\omega \mu}} \right]}{1 + (\mathrm{Kn}_\omega \mu)^2 (n\pi)^2} d\mu d\omega, \end{aligned} \tag{B.9}$$

and for $m \neq 0$

$$
\begin{aligned}
k_{mm} = {} & \frac{2}{\int_0^{\omega_m} \frac{C_\omega}{\tau_\omega} d\omega} \left\{ \int_0^{\omega_m} \frac{C_\omega}{\tau_\omega} \frac{\tan^{-1}(m\pi \mathrm{Kn}_\omega)}{m\pi \mathrm{Kn}_\omega} d\omega + 2 \int_0^{\omega_m} \frac{C_\omega}{\tau_\omega} \int_0^1 \frac{\mathrm{Kn}_\omega \mu \left[e^{-\frac{1}{(-1)^m \mathrm{Kn}_\omega \mu}} - 1 \right]}{[1 + (\mathrm{Kn}_\omega \mu)^2 (m\pi)^2]^2} d\mu d\omega \right\} \\
& + \frac{2}{\int_0^{\omega_m} \frac{C_\omega}{\tau_\omega} d\omega} \int_0^{\omega_m} \frac{C_\omega D_\omega}{\tau_\omega} \int_0^1 \frac{\mathrm{Kn}_\omega \mu \left[1 - (-1)^m e^{-\frac{1}{\mathrm{Kn}_\omega \mu}} \right]}{1 + (\mathrm{Kn}_\omega \mu)^2 (m\pi)^2} d\mu \int_0^1 \frac{\left[(-1)^m - e^{-\frac{1}{\mathrm{Kn}_\omega \mu}} \right]}{1 + (\mathrm{Kn}_\omega \mu)^2 (m\pi)^2} d\mu d\omega \\
& + \frac{2}{\int_0^{\omega_m} \frac{C_\omega}{\tau_\omega} d\omega} \int_0^{\omega_m} \frac{C_\omega D_\omega}{\tau_\omega} \int_0^1 \frac{\mathrm{Kn}_\omega \mu \left[(-1)^m - e^{-\frac{1}{\mathrm{Kn}_\omega \mu}} \right]}{1 + (\mathrm{Kn}_\omega \mu)^2 (m\pi)^2} d\mu \int_0^1 \frac{\left[1 - (-1)^m e^{-\frac{1}{\mathrm{Kn}_\omega \mu}} \right]}{1 + (\mathrm{Kn}_\omega \mu)^2 (m\pi)^2} d\mu d\omega \\
& + \frac{2}{\int_0^{\omega_m} \frac{C_\omega}{\tau_\omega} d\omega} \int_0^{\omega_m} \frac{C_\omega B_{1\omega}}{\tau_\omega} \int_0^1 \frac{\mathrm{Kn}_\omega \mu \left[1 - (-1)^m e^{-\frac{1}{\mathrm{Kn}_\omega \mu}} \right]}{1 + (\mathrm{Kn}_\omega \mu)^2 (m\pi)^2} d\mu \int_0^1 \frac{\left[1 - (-1)^m e^{-\frac{1}{\mathrm{Kn}_\omega \mu}} \right]}{1 + (\mathrm{Kn}_\omega \mu)^2 (m\pi)^2} d\mu d\omega \\
& + \frac{2}{\int_0^{\omega_m} \frac{C_\omega}{\tau_\omega} d\omega} \int_0^{\omega_m} \frac{C_\omega B_{2\omega}}{\tau_\omega} \int_0^1 \frac{\mathrm{Kn}_\omega \mu \left[(-1)^m - e^{-\frac{1}{\mathrm{Kn}_\omega \mu}} \right]}{1 + (\mathrm{Kn}_\omega \mu)^2 (m\pi)^2} d\mu \int_0^1 \frac{\left[(-1)^m - e^{-\frac{1}{\mathrm{Kn}_\omega \mu}} \right]}{1 + (\mathrm{Kn}_\omega \mu)^2 (m\pi)^2} d\mu d\omega. \qquad \text{(B.10)}
\end{aligned}
$$

These equations specify the matrix elements of $\bar{\bar{A}}$ in Eq. (3.39). With the linear system specified, the coefficients of the temperature profile x_m can be easily obtained by solving a linear system.

Appendix C

ISOTROPIC DISPERSION

We reduce computational cost by taking advantage of the cubic symmetry of Si and computing an isotropic equivalent dispersion in phonon frequency ω-space. To obtain this dispersion, we start with the full dispersion in three-dimensional wavevector k-space calculated using density functional theory (DFT) by J. Carrete and N. Mingo using ShengBTE (*88*, *89*) and Phonopy(*173*) from interatomic force constants obtained with VASP.(*91–94*) Phonon frequencies $\omega_{\mathbf{k}}$, group velocities $\mathbf{v}_{\mathbf{k}}$ and relaxation times $\tau_{\mathbf{k}}$ for the three acoustic and three optical branches are functions of wavevector $\mathbf{k} = (k_x, k_y, k_z)$. We discretize the phonon frequency between its minimum and maximum values into 101 bins with equal weight $\Delta\omega$. For each polarization, the density of states for a given frequency bin ω_i is obtained by counting the number of modes N that fall into that bin, given by

$$D(\omega_i) = \frac{N}{V\Delta\omega}, \tag{C.1}$$

where V is the volume of the First Brillouin zone, calculated from the maximum wavevectors given by the data.

We obtain average group velocities using $v_{avg}^2(\omega_i) = \langle \mathbf{v}^2(\omega_i) \rangle$, or the average of the square of group velocity for phonons in a specific frequency bin. In addition, we can compute the average of the square of the speed in a particular direction, *i.e.* $v_x^2(\omega_i) = \langle v_{k_x}^2(\omega_i) \rangle$. We find that $v_x^2(\omega_i) = v_y^2(\omega_i) = v_z^2(\omega_i) = \frac{1}{3} v_{avg}^2(\omega_i)$, which confirms that the dispersion of Si is isotropic on average.

To obtain the average relaxation time, we compute $\langle \tau(\omega_i)\mathbf{v}^2(\omega_i) \rangle / v_{avg}^2(\omega_i)$. This particular averaging is chosen to maintain the spectral thermal conductivity distribution of the full dispersion.

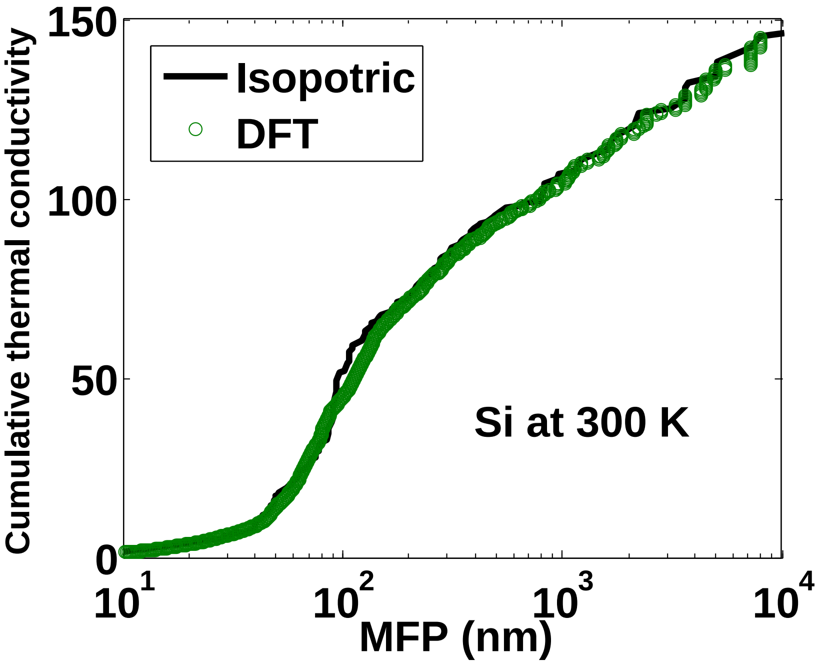

Figure C.1: Cumulative thermal conductivity as a function of phonon mean free path (MFP) for silicon at 300 K calculated by the isotropic equivalent dispersion (solid line) and the original DFT data (circles). The isotropic dispersion matches well with the ab-initio calculations as expected for a cubic crystal.

The final bulk thermal conductivity for this isotropic equivalent dispersion of silicon at 300 K is 155.0 W/m-K, very close to the original value of 155.7 W/m-K, and the cumulative thermal conductivity spectra are nearly identical, as shown in Fig. C.1.

Appendix D

SUPPLEMENTARY MATERIALS FOR PHONON TRANSMISSION COEFFICIENTS AT SOLID INTERFACES

D.1 Overview

The supplementary information contains additional information on our computational approach as well as the details about experiments and modeling. Section D.2 presents transmission coefficients for all polarizations from both sides, followed by Section D.3 showing the original raw TDTR data along with the BTE fitting results. Sections D.4 & D.5 provide details about experimental measurments and modeling, respectively.

D.2 Transmission coefficients for all polarizations

In the main text, we only show the transmission coefficient from Si to Al for longitudinal phonons for the three samples. Here, in Figs. D.1, D.2 and D.3, we plot the transmission coefficient profiles as a function of phonon frequency and wavelength from both sides of the materials for each polarization with a clean interface, with a native oxide layer and with a thermally grown oxide layer. The color intensity indicates the likelihood that a single transmission coefficient curve passing through a particular point at a given phonon frequency is able to simultaneously explain all of the experimental data. We emphasize that the only fitting parameters are the transmission coefficients from Si to Al for the three polarizations. All other transmission and reflection coefficients are determined from detailed balance and energy conservation.(*79*)

For the clean interface, the only constraint used in the fitting process is the smoothness of the profile. In particular, note that we do not enforce any type of monotonicity or shape requirement on the coefficients other than smoothness. For the native oxide interface, we additionally require that the transmission coefficients of the native oxide interface do not exceed the values for the clean interface. Similarly, the transmission coefficients of the thicker oxide interface should always be smaller than those of the native oxide interface.

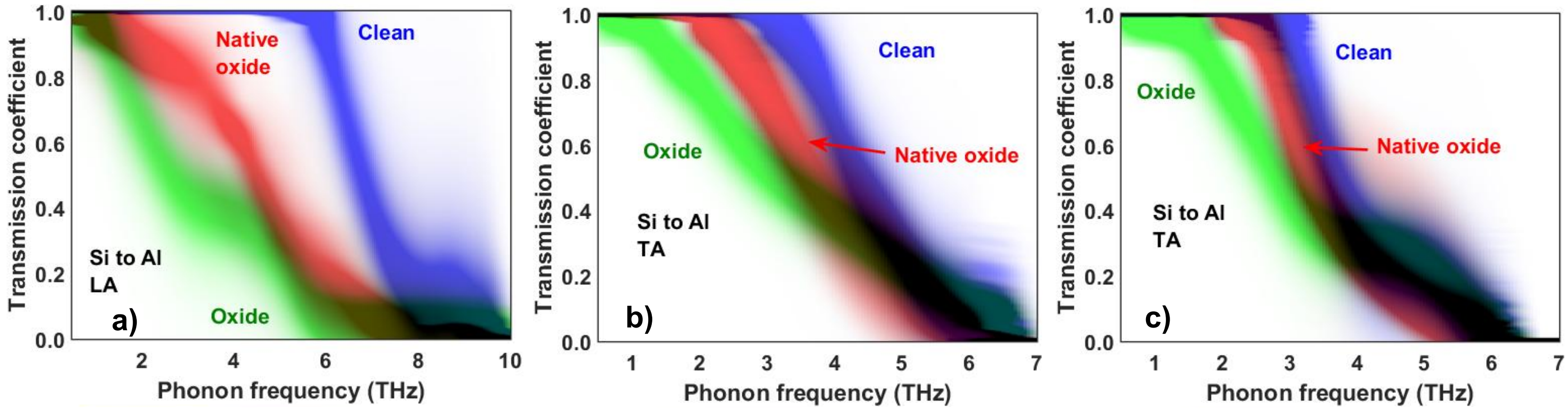

Figure D.1: Transmission coefficients from Si to Al versus phonon frequency for different polarizations measured from Al/Si sample with three different interfaces studied in this work. The intensity of the shaded region corresponds to the likelihood that the transmission coefficient possesses a given value. We emphasize that the transmission coefficients for the three polarizations are the only fitting parameters in our calculations.

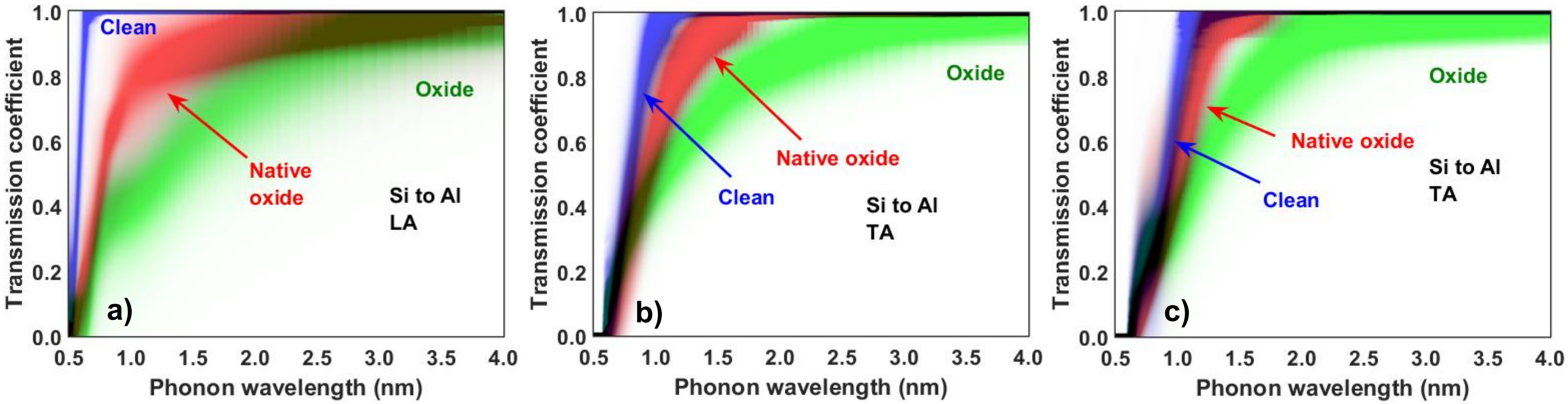

Figure D.2: Transmission coefficients from Si to Al from Fig. D.1 plotted versus phonon wavelength for different polarizations measured from Al/Si sample with three different interfaces studied in this work.

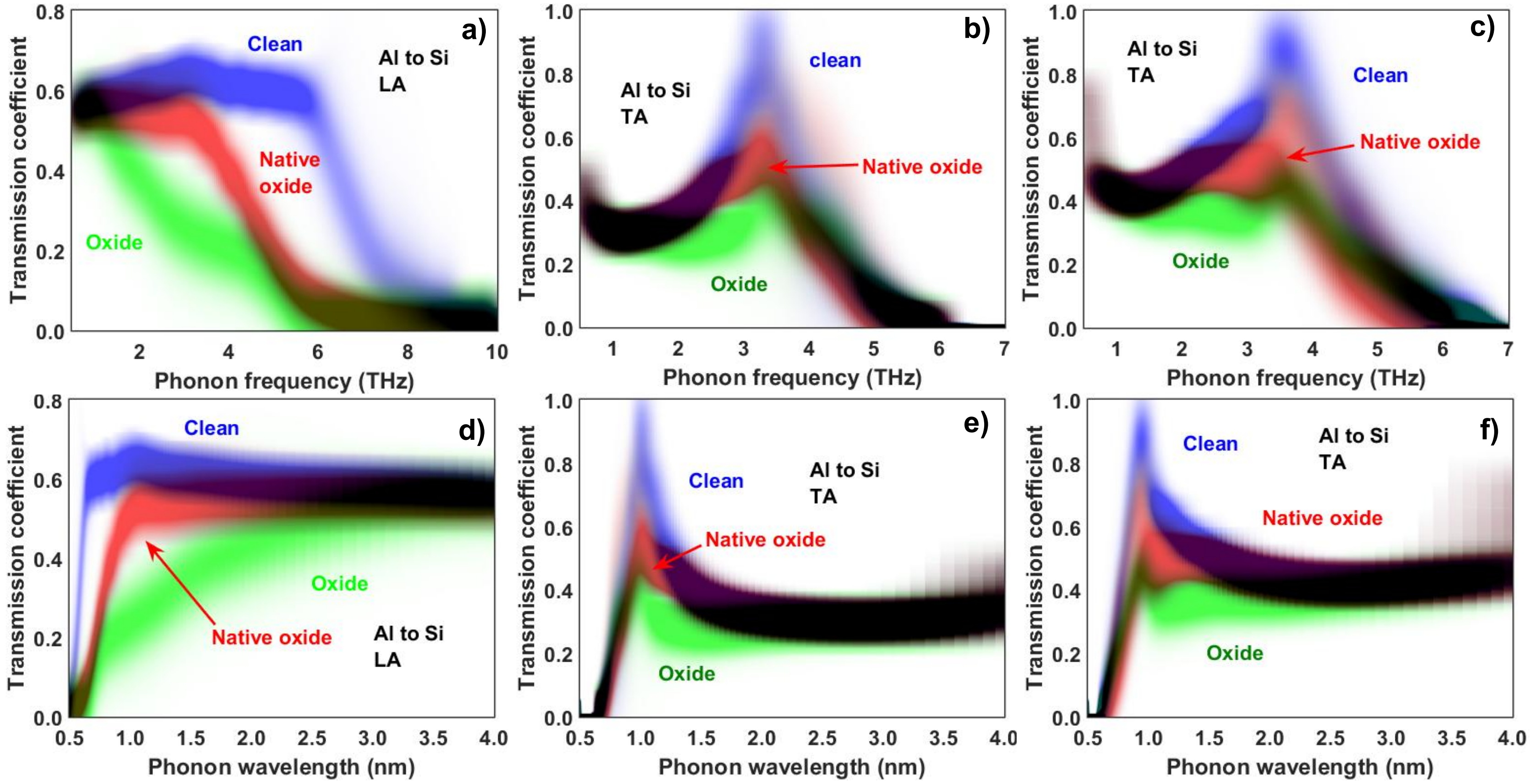

Figure D.3: Transmission coefficients from Al to Si versus (a)-(c) phonon frequency and (d)-(f) phonon wavelength for different polarizations measured from Al/Si sample with three different interfaces studied in this work, calculated using the measured values of the transmission coefficients from Si to Al shown in Fig. D.1. The increase in transmission coefficient from Al to Si at phonon frequencies less than approximately 4 THz are due to the requirements of detailed balance. Specifically, these coefficients must follow the shape of the density of states since the coefficients from Si to Al are a constant value. These coefficients are determined by the principle of detailed balance and are not free parameters.

D.3 TDTR data

In Figs. D.4 & D.5, we plot all the original raw data from the TDTR experiments used in the manuscript along with the BTE fitting results. In all the cases, we show excellent agreement between simulation and experiments.

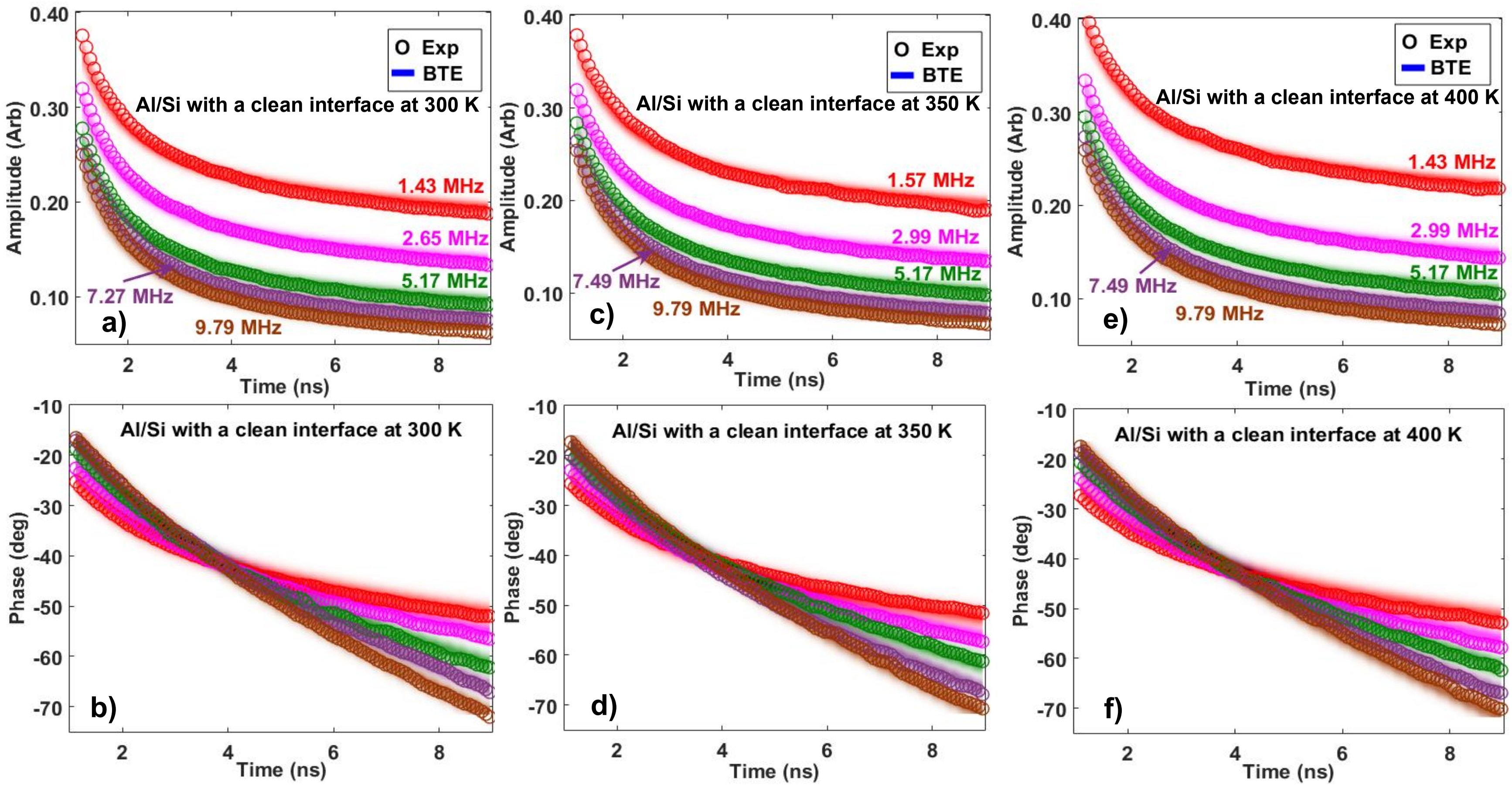

Figure D.4: Experimental TDTR data (symbols) of an Al/Si sample with a clean interface at T = 300 K, 350 K and 400 K at different modulation frequencies fit to the data from the BTE simulations (shaded regions), demonstrating excellent agreement between simulation and experiment at different temperatures.

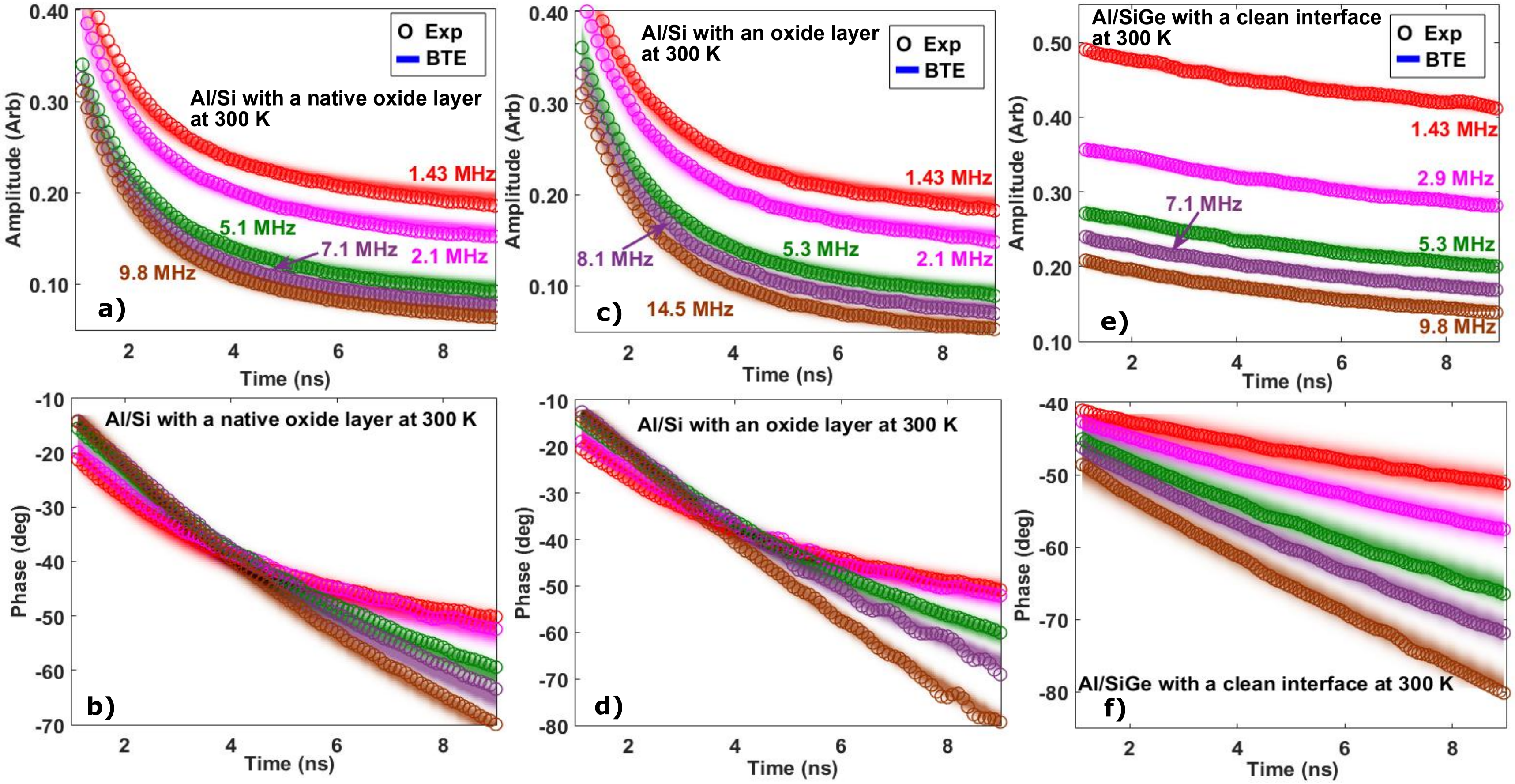

Figure D.5: Experimental TDTR data (symbols) of an Al/Si sample with a native oxidized interface, an Al/Si sample with a thermally oxidized interface, and an Al/SiGe with a clean interface at T = 300 K at different modulation frequencies fit to the data from the BTE simulations (shaded regions).

D.4 Experimental details

Sample preparation

Commercial high-purity natural Si (100) wafer and Si-Ge (1.5-2 at % Ge) wafer (100) from MTI Corp. were used in the experiments. Before coating Al on the samples, three different surface conditions of the samples were prepared. First, the native oxide was removed with buffered HF acid to obtain a clean surface of Si and SiGe. After etching, the samples were immediately put into a vacuum chamber for Al deposition. Second, the native SiO_2 layer was left in place. No further treatment was taken for this condition before Al deposition. Finally, a thermally grown SiO_2 layer as fabricated by putting the Si samples into a tube furnace for three hours. The thickness of the native SiO_2 layer and thermally grown SiO_2 layer was measured by ellipsometry and TEM to be $\sim$ 1 nm and $\sim$ 3.5 nm, respectively. A thin film of Al was deposited on all samples using electron beam evaporator. The thickness of the Al transducer layer was 70 nm, measured by atomic force microscopy.

TDTR measurements

The measurements are taken on two-tint TDTR. The details are available in Ref. 64. The probe diameter is 10 μm and the pump diameter is 60 μm. Both beam sizes are measured using a home-built two-axis knife-edge beam profiler. With 60 μm pump heating size, the heat transfer problem can be treated as one-dimensional. All the measurements at $T = 300$ K are performed under ambient conditions, and the additional measurements at $T = 350$ and 400 K are performed in an optical cryostat (JANIS ST-500) under high vacuum of 10^{-6} torr.

TEM images

The TEM samples were prepared by standard FIB lift-out technique in the dual beam FE-SEM/FIB (FEI Nova 600). To protect the top surface, a Pt layer with thickness $\sim$ 300 nm was deposited with electron beam evaporation followed by another Pt layer with thickness ~ 3-4 μm by Ga ion beam. The lamella was cut parallel to the chip edge which was aligned to the wafer flat edge during initial cutting in TDTR sample preparation. As a result, the cutting surface normal was along (110) direction and all the TEM images were taken parallel to the Si (110) crystallographic zone axis. High resolution transmission electron microscopy (HRTEM) analyses were carried out in a FEI Tecnai TF-20 TEM/STEM at 200 kV. To avoid damage from the high energy electron beam, the beam exposure on region of interest was minimized especially at high magnification during operation.

D.5 Ab-initio properties and modeling details

Point defect scattering in SiGe

For SiGe, the mass difference scattering rate is calculated using the Tamura formula,(*184*) given by

$$\tau^{-1} = \frac{\pi}{6} V_0 m_0 \omega^2 D(\omega), \tag{D.1}$$

where ω is phonon frequency, $D(\omega)$ is the phonon density of states per unit volume, and V_0 is the volume per atom. $m_0 = \sum_i f_i (1 - m_i/\bar{m})^2$ is a measure of the mass disorder, f_i and m_i are the concentration and the atomic mass of species i, respectively, and $\bar{m}$ is the average mass for the given composition. The Tamura formula has been proven to effectively calculate the impurity scattering in SiGe with different Ge concentration.(*185*) The values of all the constants in Eq. D.1 are tabulated in Table D.1

We have sent the SiGe wafer to the third party, Thermotest, for bulk thermal conductivity measurements. The measured value, using transient plane source method on a bulk sample, is 50.7 ± 0.5 W/m-K. Using the measured value, we are able to obtain the Ge concentration to be about ~ 2 at % based on calculations with the Tamura formula while the measured Ge concentration using Energy Dispersive X-ray Spectrometry is ~ 1.5 at %, which gives SiGe thermal conductivity around

$\sim$ 58 W/m-K. These differences in atomic concentration have only a minimal effect on the transport calculations and have been incorporated in the uncertainty of BTE simulations in Fig. 5.12 of the main text.

Al thermal conductivity

We assume a constant MFP for all modes in Al; the value $\Lambda_{Al} = 60$ nm is chosen to yield a lattice thermal conductivity $k \approx 123$ W/m-K so that no size effects in the thin film occur. Although the literature value of Al thermal conductivity is about 230 W/m-K, we verified that the resulting surface temperature decay curves by using these two Al thermal conductivities in the TDTR diffusion model could not be distinguished as shown in Fig. D.6. Since the transmission coefficients are extracted by fitting our model to the data, if a parameter in the model has little effect on the results of the model, then it cannot affect the measured transmission coefficients. Here, we demonstrate that the calculations are completely insensitive to Al thermal conductivity, provided that it is larger than $\sim$ 30 W/m-K. Therefore, our choice of Al thermal conductivity has no impact on our results.

The relaxation time for each mode is then obtained through $\tau_\omega = \Lambda_{Al}/v_\omega$. We also verified that the particular value of the Al MFP does not affect the results. Note that although the Al MPF is a constant, the dispersion of Al is directly from the first-principle calculations, and the transmission coefficients depend heavily on the density of states and phonon group velocity in both metal and substrate. Therefore, Al is still modeled with a spectral phonon BTE.

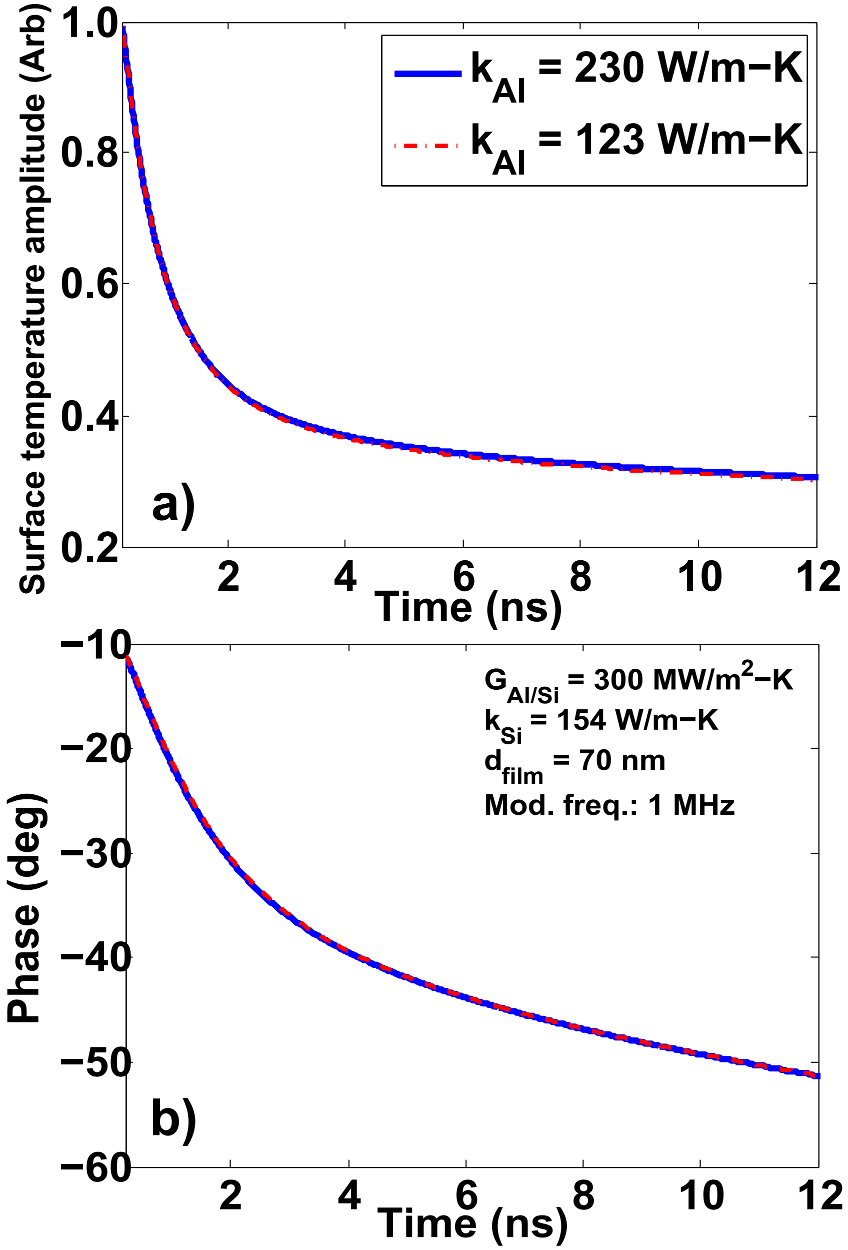

Figure D.6: Calculated transient surface temperature (a) amplitude and (b) phase for Al on Si using a two-layer diffusive model with Al thermal conductivity to be 230 W/m-K (solid blue line) and 123 W/m-K (dash-dotted red line). The surface temperature response is not sensitive to the change of Al thermal conductivity from 230 W/m-K to 123 W/m-K.

Table D.1: All the constants appearing in the BTE models and the fitting process are given in the following table.

Bulk thermal properties	
Al heat capacity (J/m^3-K):	2.41×10^6
Al lattice thermal conductivity (W/m-K):	123
Al total thermal conductivity (W/m-K):	230
Si heat capacity (J/m^3-K):	1.63×10^6
Si thermal conductivity (W/m-K):	155
SiGe heat capacity (J/m^3-K):	1.63×10^6
SiGe thermal conductivity (W/m-K):	51
Electronic thermal properties in Al	
Heat capacity (J/m^3-K):	4.11×10^4
Thermal conductivity (W/m-K):	203
Electron-phonon coupling coefficient g (W/m^3-K):	2.1×10^{17}
Constants in Tamura formula	
Volume per Si atom V_0 (nm^3):	0.02
Measure of the mass disorder m_0:	0.0568
Transducer film thickness	
Al/Si with a clean interface (nm):	69
Al/SiGe with a clean interface (nm):	72
Al/Si with a native oxidized interface (nm):	70
Al/Si with a thermally-grown oxidized interface (nm):	70
Other constants	
Optical penetration depth δ (nm):	10
Laser repetition frequency (MHz):	76